UNIVERSITY OF CALIFORNIA,
IRVINE

Development of Label-free, Non-faradaic Electronic Biosensors using Polymer Bio-composites for Rapid Detection of Proteins

DISSERTATION

submitted in partial satisfaction of the requirements
for the degree of

DOCTOR OF PHILOSOPHY

in Chemistry

by

Alana Frances Ogata

Dissertation Committee:
Professor Reginald M. Penner, Chair
Associate Professor Mathew D. Law
Associate Professor Andrej Luptak

2018

DEDICATION

To my family and friends, who are an essential part of my happiness, determination to be the best version of myself, and passion for science…

I dedicate this thesis to my mother, Willa, and my father, Reichel, who gave me the ultimate gift of love and support so I could go through life with enthusiasm and confidence in myself…

To Evan, who is way cooler than me and always lends a listening ear…

To Will, you are my person and inspire me more than you know every day…

To keep me humble and always curious…

Everyone you will ever meet knows something you don't.
-Bill Nye-

TABLE OF CONTENTS

LIST OF FIGURES

LIST OF TABLES

ACKNOWLEDGMENTS

I would like to thank my advisor Reg Penner for support and guidance throughout my PhD career. I consider you a prime example of a scientist and mentor. You enable so much growth for me as a researcher and always support my efforts. In addition to your wealth of knowledge, what I find most admiring is the humanity you bring to science. You always do what's right and best for the science and lead by example; I often try to follow. Ultimately you make science welcoming and exciting. Thank you for great graduate school experience.

Thank you to my committee members, Andrej Luptak and Matt Law. Andrej, thank you for providing the most stimulating conversations that could stem from even my simplest questions. After every meeting, I fed off of your energy, immense amount of knowledge, and new ideas for experiments. Also, if I didn't laugh in the moment, I do think your jokes are funny. Matt, thank you for providing sound advice and feedback. After feeling slightly 'burnt out' in graduate school, you suggested I reflect more and that ultimately lead me to realize my passion for research and education. I am excited to pursue a career in academia.

To my parents, Reichel and Willa, thank you for all the love and support that has made me the independent and fearless person I am today. Mom, I believe I have a passion and enthusiasm for education because I was raised by an amazing teacher. You have always inspired me as kind, independent, and intelligent woman, teacher, and mother. Thanks for always being there. Papa, you have made me a very resilient person and scientist who is not afraid to fail. You always told me failure can be a good thing and is necessary. Now I am not afraid to face challenges head on knowing that it will always be a learning and growing experience. To my brother Evan, thanks for letting me vent to you at random times and giving calm, rational advice. I don't know how you keep your cool, but I will always try to be as cool as you.

To all the people I have met at UCI, I did not have to go through graduate school alone and I thank you all for that. To the Penner lab (current and past members), thank you for being a wonderfully supportive group of scientists and creating an environment where we can all help each other. To Kellen, Adam, Millie, and Gerald, thanks for adopting me into your group, letting me hang out in your office, and all the cabo cantina adventures. To Brandon (and Brit, we miss you), the list is too long to thank you, I'm blessed to have met you first year while looking for people to do quantum homework with and now have an amazing friend to get through this crazy thing called grad school.

To my friends away from school, my other lifeline. Thanks to CRACKL for still being my second family even across the nation and taking me on awesome adventures to new cities. To Gerald, Lindsay, Andrea, Andrew, and Sam, thanks for all the rage cage, obviously, and making California a home to me and Will.

Last but not least. Thank you Will. Thank you for going through this whole experience with me and always standing by my side when things got rough. I could leave all my research troubles behind the second I came home to you and be refreshed to take on the next day. You are an amazing human and I am so blessed that we now have so many California adventures to look back on and so many more to be had. You are my person and inspire me every day.

This dissertation belongs to all of you as much as it belongs to me. I hope you find the work presented in this dissertation informative and inspiring.

CURRICULUM VITAE

Alana F. Ogata

Curriculum Vitae

November 15, 2018

A. Personal Information

Date of Birth:	September 6, 1992
Business Address:	Department of Chemistry 2313 Natural Sciences 2 University of California, Irvine Irvine, 92617
Phone:	(703) 894 8968
Email:	alanao@uci.edu

B. Academic History

1. College of William & Mary, Williamsburg, Virginia, 2010 - 2014
   B.S. Chemistry, minor Mathematics, 2014, Thesis Advisor: Kristin Wustholz

2. University of California, Irvine, 10/01/2014 – 12/07/2018
   PhD. Chemistry, Thesis Advisor: Reginald Penner

C. Fellowships/Grants

University California, Irvine

1. UCI Chemistry Department Dissertation Fellowship
   UCI Fall Quarter Stipend, Tuition, and Fees
   09/27/2018 – 12/20/2018
2. National Science Foundation Graduate Research Fellowship Program
   Three-year annual stipend with a $12,000 cost of education allowance
   06/01/2015 – 6/01/2018
3. NSF-Graduate Research Opportunities Worldwide Fellowship
   Four-month stipend with $4,000 allowance to conduct research at KAIST, South Korea
   06/06/2017 – 11/01/2017

College of William & Mary

1. Virginia Space Grant Consortium
   $8,500 of research funding from the NASA Undergraduate Research Scholarship
   08/2013 – 05/2014
2. Charles Center Summer Scholarship
   $3,000 of summer research funding from the Sayford Student Research Endowment
   06/01/2012 – 08/01/2012
3. Friends of TODAI Inc Scholarship
   $4,000 research scholarship to fund University of Tokyo Research Internship Program

06/01/2013 – 07/20/2013

D. Publications

University California, Irvine

1. Bhasin, A$^{\alpha}$; **Ogata, Alana F**$^{\alpha}$; Briggs, Jeffrey S; Tam, PY; Tam, Ming X; Weiss, Gregory A; Penner, Reginald M. The Virus bioresistor: Wiring Virus Particles for the Direct, Label-Free Detection of Target Proteins. *Nano Letters*. 2018, 18 (6), 3623-3629.
(α indicates first coauthors)

2. **Ogata, Alana F**; Song, Seok-Won; Cho, Su-Ho; Koo, Won-Tae; Jang, Ji-Soo; Jeong, Yong Jin; Kim, Min-Hyeok; Cheong, Jun Young; Penner, Reginald M*; Il-Doo Kim*. An Impedance-Transduced Chemiresistor with a Porous Carbon Channel for Rapid, Nonenzymatic, Glucose Sensing. *Analytical Chemistry*. 2018, 90 (15), 9338-9346.

3. Qiao, Shaopeng; **Ogata, Alana F**; Jha, Gaurav; Chattopadhyay, Aurnov; Penner, Reginald M*. Rapid, Wet Chemical Fabrication of Radial Junction Electroluminescent Wires. *ACS Applied Materials &Interfaces.* 2018, Article ASAP.

4. Jha, Gaurav; Tran, Thien; Qiao, Shaopeng; Ziegler, Joshua M; **Ogata, Alana F**; Dai, Sheng; Xu, Mingjie; Thai, Mya L; Chandran, Girija T; Pan, Xiaoqing*; Penner, Reginald M*. Electrophoretic Deposition of Mesoporous Niobium (V) Oxide Nanoscopic Films. *Chemistry of Materials*. 2018, 30 (18), 6549-6558.

5. Cheong, Joon Young.; Youn, Doo Young.; Kim, Chanhoon.; Jung, Ji-Won.; **Ogata, Alana F.**; Bae, Jin Gook.; Kim, Il-Doo*. Ag-coated one-dimensional orthorhombic Nb_2O_5 fibers as high-performance electrodes for lithium storage. *Electrochimica Acta* 2018, (269) 338-396.

6. **Ogata, Alana F**; Edgar, Joshua M.; Majumdar, Sudipta; Briggs, Jeffrey S.; Patterson, Shae V.; Tan, Ming X.; Kudlacek, Stephan T.; Schneider, Christine A.; Weiss, Gregory A*.; Penner, Reginald M*. Virus-enabled biosensor for human serum albumin. *Analytical Chemistry*. 2017, 89 (2), 1373-1381.

7. Chandran, Girija T$^{\alpha}$; Li, Xiaowei$^{\alpha}$; **Ogata, Alana F**$^{\alpha}$; Penner, Reginald M*. Electrically Transduced Sensors Based on Nanomaterials. *Analytical Chemistry.* 2017,89 (1), 249-275.
(α indicates first coauthors)

8. Koo, Won-Tae.; Qiao, Shaopeng.; **Ogata, Alana F**.; Jha, Gaurav.; Jang, Ji-Soo.; Chen, Vivian T.; Kim, Il-Doo.; Penner, Reginald M*. Accelerating Palladium Nanowire H_2 Sensors Using Engineered Nanofiltration. *ACS Nano*. 2017,11, 9276.

9. Jang, Ji-Soo.; Qiao, Shaopeng.; Choi, Seon-Jin.; Jha, Gaurav.; **Ogata, Alana F**.; Koo, Won-Tae.; Kim, Dong-Ha.; Kim, Il-Doo.; Penner, Reginald M*. Hollow Pd-Ag Composite Nanowires for Fast Responding and Transparent Hydrogen Sensors. *ACS Applied Materials and Interfaces*. 2017, 9, 39464.

10. Chandran, Girija T.; Jha, Gaurav.; Qiao, Shaopeng.; Thai, Mya Le.; Dutta, Rajen K.; **Ogata, Alana F**.; Jang, Ji-Soo.; Kim, Il-Doo*.; Penner, Reginald M*. Supercharging a

MnO_2 Nanowire: An Amine-Altered Morphology Retains Capacity at High Rates and Mass Loadings. *Langmuir*. 2017, (33) 9324.

11. Thai, Mya Le.; Qiao, Shaopeng.; Dutta, Rajen K.; Jha, Gaurav.; **Ogata, Alana F**.; Chandran, Grijia T.; Penner, Reginald M*. Collateral Advantages of a Gel Electrolyte for MnO_2 Nanowire Capacitors: Higher Voltage; Reduced Volume. *ACS Energy Letters*. 2017, 2 (5), 1162-1169.

College of William & Mary

1. Tan, Jenna A; Garakyaraghi, Sofia; Tagami, Kan A; Frano, Kristen Frano A; Crockett, Heidi M; **Ogata, Alana F**; Patterson, Joshua D; Wustholz Kristin L*. Contributions from excited-state proton and electron transfer to the blinking and photobleaching dynamics of alizarin and purpurin. *Journal of Physical Chemistry C.*2014,121 (1), 97-106.

2. Wustholz. K***; Ogata. Alana F**$^{\alpha}$; Wong. N$^{\alpha}$, Dispersive Electron-Transfer Kinetics from Single Molecules on TiO_2 Nanoparticle Films. *Journal of Physical Chemistry C.* 2013, 117 (41), 21075-21085.
(α indicates first coauthors)

E. Patents

1. Penner, R.M., **Ogata, A.F**., Bhasin, A., Weiss, G.A., Tam, P., Briggs, J.S., (filed March 29, 2018). U.S. Provsional Application Serial Number 62/650,059

2. **Ogata, A.F**., Edgar, J.M., Majumdar, S., Weiss, G.A., Penner, R.M., Tan, M.X. (filed December 19, 2016). Virus composite biosensor. U.S. Provisional Application Serial Number 62/436,373.

F. Research Summary

My research focuses on the development of various electronic nanomaterial-based biosensors for detection of biomarkers in body fluids. I employ electrochemistry, photolithography, and electrospinning to create nanomaterials, typically electronically conductive polymers, to drive the evolution of simple, label-free, and rapid (i.e,. < 10 s) biosensors for point-of-care diagnostics. Device fabrication is routinely paired with heavy microscopy and materials characterization (SEM, AFM, EDS, XPS, and BET) to probe what structure, morphology, and chemical composition produces optimal nanomaterial properties for detection of a desired biomarker. Electrodeposition methods, surface modification chemistries, and chemical doping are utilized to inertly functionalize viruses, boronic acid molecules, or aptamers onto a nanostructure or biosensor surface. The culmination of my PhD research is categorized into three collaborations between UCI university labs (Greg Weiss and Andrej Luptak), international institutions (KAIST), and a start-up company (PhageTech Inc). I am involved in patenting two of my biosensor designs and have successfully reported my work in three first-author publications to Analytical Chemistry and Nano Letters. One innovative contribution of these works is the introduction of the virus bioresistor, which represents a new class of electronic biosensors that directly incorporates biological entities into an electrical circuit for a device that is label free and highly sensitive to target binding.

G. Invited Presentations and Talks

University California, Irvine

09/19/2018 Beckman Coulter's Innovation Event, *Guest Speaker*
08/02/2018 Inside UCI Series: Incoming undergraduate student, *Presenter*
06/06/2018 Inside UCI series: Transfer students, *Presenter*
05/31/2018 UCI Foundation Trustee Board Meeting, *Guest Speaker*
05/22/2018 OCACS high school awards dinner at UC Fullerton, *Keynote Speaker*
05/03/2018 UC-wide GradSlam, LinkedIn Headquarters, UCI Representative *Speaker*
03/21/2018 Women in STEM symposium, St. Margaret's Episcopal School, *Speaker*
05/26/2017 NSF GFRP Symposium, *Poster Presenter*
03/05/2017 Pittcon, Society of Electroanalytical Chemistry Student Session, *Speaker*
03/17/2016 American Chemical Society Conference 2016, *Poster*

College of William & Mary

04/11/2013 Virginia Space Grant Consortium Student Research Conference, *Poster*
11/05/2012 Southern Regional Meeting, American Society Inc. Conference, *Poster*

H. Teaching Assistant Appointments

University California, Irvine

Honors General Chemistry Lab
Honors General Chemistry
General Chemistry Lab

College of William & Mary

Linear Algebra

I. Service

1. Program Co-leader- Nano Electrochemistry eXtensions to Technology Penner Group Highschool Outreach Program. 07/09/2018 – 08/06/2018
2. Lead Volunteer- UCI CaSTL Boys & Girls Club Partnership, Advancing Informal Science Education. 11/2015 – 04/2016. 11/2016 – 04/2017. 11/2017 – 04/2018.

J. Awards

University California, Irvine

05/23/2018 The Jacqueline Smitrovich Department of Chemistry Prize
03/02/2018 UCI Grad Slam 1st place winner
05/26/2017 NSF GFRP Research Symposium Poster 1st place award

College of William & Mary

2014 ACS Award in Inorganic Chemistry, 2014
2014 Summa Cum Laude, 2014
2014 William and Mary's Dean's List (2010-2014)

K. Students Supervised

Undergraduate Students

Christine May Liu, UCI 10/2015 – 06/2018, current position: NIH Postbaccalaureate IRTA Program

High School Students

Andrew Song, UCI 07/09/2018 – present

L. Honor Society Memberships

2014 Phi Beta Kappa Honor Society
2011 National Society of Collegiate Scholars
2011 Phi Eta Sigma Honor Society

ABSTRACT OF THE DISSERTATION

Development of Label-free, Non-faradaic Electronic Biosensors using Polymer Bio-composites for Rapid Detection of Proteins

By

Alana Frances Ogata

Doctor of Philosophy in Chemistry

University of California, Irvine, 2018

Professor Reginald M. Penner, Chair

In this thesis the development of label-free, non-faradaic, and rapid electronic biosensors based on conducting polymers for point-of-care applications is presented. Issues with label-free, non-faradaic electronic biosensors are addressed. First, we will address issues of poor sensitivity or low sensor signal that is typically seen when redox labels, which provide signal amplification in electrochemical biosensors, are taken out of a biosensor design. We describe two generations of virus-polymer-based biosensors that use impedance spectroscopy to transduce protein binding events. In chapter 2, a first-generation virus biosensor will show that a simple, monolithic design can be sensitive (limit-of-detection of 100 nM) and rapid (response time < 60s) for protein detection by analyzing the impedance spectrum for an optimal sensing regime. In Chapter 3, the virus-bioresistor will be introduced to establish that large amounts of sensor signal can be produced from a label-free, non-faradaic electronic system by taking advantage of impedance spectroscopy measurements on a chemiresistive channel. Equivalent circuit fitting of the impedance Nyquist plot enables independent measurement of channel resistance versus solutions resistance and provides large signals from direct protein binding to the channel surface. The virus bioresistor

improves the first-generation virus-based biosensor with a 7.5 nM limit of detection and a 3 -30 s response time. In Chapter 4, we will address the generality of the virus-bioresistor by applying impedance-transduced chemiresitive measurements to a channel composed of porous carbon nanofibers for detection of glucose. Copolymer nanofibers fabricated by electrospinning are doped with fluoride and functionalized with phenylboronic acid for direct binding to glucose. Impedance measurements are ultimately taken at a single, optimal frequency to provide real-time sensing with ultrafast response times < 8 s and a detection range of 50 μM to 5 mM for glucose. In the entirety of this dissertation, each biosensor shows excellent reproducibility with coefficient-of-variation values < 10%.

Chapter 1

Introduction

This chapter was adapted from a research article (Chandran, Girija T; Li, Xiaowei; Ogata, Alana F; Penner, Reginald M. *Analytical Chemistry.* **2017**,89 (1), 249-275)

1.1 Electrically Transduced Sensors Based on Nanomaterials

The synthetic nanomaterials that have enabled an era of transformative sensor science began to emerge in the mid-1980s with the discovery by Kroto, Smalley, and workers[1] of Buckminster fullerene, highly stable clusters of 60 carbon atoms (C60). The electrochemical, optical, and mechanical properties of fullerenes have since been characterized by showing excellent conductivity, high electroactive surface areas, and biocompatibility.[2-4] Around the same time, Brus and co-workers demonstrated the synthesis of colloidal semiconductor nanocrystals.[5] These discoveries of new, zero-dimensional nano-materials produced tremendous excitement for their size-tunable applications in electrically based sensors because the techniques for immobilizing these nanoparticles and for functionalizing their surfaces did not yet exist. Electrically conductive support materials that could serve as "wires", enabling electrical connections to nanoparticles, were still in the future. These became available in 1991 with the discovery by Sumio Iijima[6] of the first one-dimensional nanomatierla, single- and multiwalled carbon nanotubes (CNTs). Techniques for producing CNTs in quantity using chemical vapor deposition were quickly discovered and refined and relatively rapidly, CNTs were widely available.[7-9] A new era of nanomaterials-based, electrically transduced sensing was launched by this discovery. 2D materials, with tremendous potential for sensors, were discovered later: graphene (2004 [10]), 2D transition metal dichalcogenide (TMD) monolyares (2010 [11-14]), and MXenes (2011 [15]).

With few exceptions, sensors exploiting electrical transduction can be classified as chemiresistors, field-effect transistors (FETs), or electrochemical sensors. Chemiresistors are simply electrical conduits having a resistance that is altered by the direct interaction of an analyte molecule with the sensors surface. A well-known example are palladium (Pd) nanowire sensors

for hydrogen gas.[16] In this case, H_2 chemisorbs at the Pd surface forming $2H_{ads}$. Subsequent diffusion of H into the Pd sensing element causes the formation of bulk PdH_x having a higher electrical resistance than Pd metal. FETs, on the other hand, measure the charge carrier mobility through a channel that is subjected to an applied electrical field from a conductive gate electrode. The gate potential causes an accumulation or a depletion of mobile charge carriers, modifying the conductivity of the channel. Charged analyte species adsorbed or otherwise bound at the channel surface can also gate charge carriers within the channel, leading to measurable changes in the transfer characteristics for the FET. IN the first example of FET sensors derived from semiconductor nanowire, Lieber and co-workers demonstrated the detection of streptavidin by biotin-modified silicon nanowire FETs in 2001.[17] Electrochemical sensors derive signal from the electron transfer reaction of on intermediate that may be tethered to the sensor surface or current associated with the direct or indirect electrooxidation or reduction of the target species itself.

1.2 Polymer Nanostructures

Since the discovery of polyacetylene by Heeger, MacDiarmid, and Shirakawa,[18] electronically conductive organic polymers have become a mainstay in sensor technology, valued for their tunable electronic properties and mechanical behavior.[19-21] Polymers such as polyaniline (PANI), poly(3-4 ethylenedioxythiophene) (PEDOT), and polypyrrole (PPy) are attractive due to their facile syntheses and processing, low weight, and flexibility. Conductive polymers are available in various "flavors" of nanostructures for sensing applications: The established field of polymer nanowire-based sensors has been augmented by polymer nanotubes, nanoparticles, nanofibers, and polymer hybride nanostructures all of which have been discussed in the following comprehensive reviews. [22,23] Advances in polymerization methods for nanostructured polymers

have also been previously discussed.[24] Conductive polymer nanomaterials enable excellent sensitivity and specificity for gas, chemical, and biosensors.[22,25] Most recent advances in polymer-nanostructured sensors demonstrate a continuing improvement of sensitivity and analysis time. The optical, electronic, and chemical properties of PEDOT and PANI can be modified making them ideal for flexible, transparent, and wearable electronics.[25,26]

1.3 Dissertation Overview

This dissertation focuses on the fabrication, characterization, and optimization of label-free electronic biosensors for rapid protein detection. All three projects described here focus on biosensors comprised of electronically-conductive polymer composites on the sensor surface and transduce a binding signal by impedance spectroscopy. In each chapter, impedance spectroscopy is utilized to robustly characterize the electrical properties of a biosensor and establish sensitivity, specificity, and response time to a target analyte. Fundamentals of impedance spectroscopy are discussed in the following comprehensive book.[27]

In Chapter 2, the label-free detection of human serum albumin (HSA) in aqueous buffer is demonstrated using a simple, monolithic, two-electrode electrochemical biosensor. In this device, both millimeter-scale electrodes are coated with a thin layer of a composite containing M13 virus particles and the electronically conductive polymer poly(3,4 ethylenedioxy thiophene) or PEDOT. These virus particles, engineered to selectively bind HSA, serve as receptors in this biosensor. The resistance component of the electrical impedance, Z_{re}, measured between these two electrodes provides electrical transduction of HSA binding to the virus-PEDOT film. The analysis of sample volumes as small as 50 µL is made possible using a microfluidic cell. Upon exposure to HSA, virus-PEDOT films show a prompt increase in Z_{re} within 5 s and a stable Z_{re} signal within 15 min.

HSA concentrations in the range from 100 nM to 5 μM are detectable. Sensor-to-sensor reproducibility of the HSA measurement is characterized by a coefficient of variance (COV) ranging from 2-8% across this entire concentration range. In addition, virus-PEDOT sensors successfully detected HSA in synthetic urine solutions.

Chapter 3 describes on a novel virus-bioresistor model that takes advantage of directly incorporating M13-virus into an electrical circuit. The virus bioresistor (*VBR*) is a chemiresistor that directly transfers information from virus particles to an electrical circuit. Specifically, the *VBR* enables the label-free detection of a target protein that is recognized and bound by filamentous M13 virus particles, each with dimensions of 6 nm (w) x 1 μm (l), entrained in an ultra-thin (≈250 nm) composite virus-polymer resistor. Signal produced by the specific binding of virus to target molecules, is monitored using the electrical impedance of the *VBR*: The *VBR* presents a complex impedance that is modeled by an equivalent circuit containing just three circuit elements: a solution resistance (R_{soln}), a channel resistance (R_{VBR}), and an interfacial capacitance (C_{VBR}). The value of R_{VBR}, measured across five orders of magnitude in frequency, is increased by the specific recognition and binding of a target protein to the virus particles in the resistor, producing a signal ΔR_{VBR}. The *VBR* concept is demonstrated using a model system in which human serum albumin (HSA, 66 kDa) is detected in a phosphate buffer solution. The *VBR* cleanly discriminates between a change in the electrical resistance of the buffer, measured by R_{soln}, and selective binding of HSA to virus particles, measured by $R_{VBR.}$ The ΔR_{VBR} induced by HSA binding is as high as 200 Ω, contributing to low sensor-to-sensor coefficients-of-variation (<15%) across the entire calibration curve for HSA from 7.5 nM to 900 nM. The response time for the *VBR* is 3 - 30 seconds.

Chapter 4 deviates from virus-based biosensors and a new type of chemiresistor, the impedance-transduced chemiresistor (*ITCR*), is described for the rapid analysis of glucose. The

ITCR exploits a porous, high surface area, fluorine-doped carbon channel prepared by electrospinning of fluorinated polymer nanofibers followed by pyrolysis. This channel is functionalized with a boronic acid receptor for glucose from Nafion-containing solution. The recognition and binding of glucose by the *ITCR* is detected by measuring its electrical impedance at a single frequency. The analysis frequency is selected by measuring the signal-to-noise (S/N) for glucose detection across five orders of magnitude, evaluating both the imaginary and real components of the complex impedance. Based on this analysis, an optimal frequency of 13 kHz is selected for glucose detection, yielding a S/N ratio of 60-100 for [glucose] = 5 mM using the change in the total impedance, ΔZ. The resulting *ITCR* glucose sensor shows a rapid analysis time (< 8 s), low coefficient-of-variation for a series of sensors (< 10%), an analysis range of 50 µM to 5 mM, and excellent specificity versus fructose, ascorbic acid, and uric acid. These metrics for the *ITCR* are obtained using a sample size as small as 5 µL.

1.4 References

(1) Kroto, H. W.; Heath, J. R.; O'Brien, S. C.; Curl, R. F.; Smalley, R. E. Nature **1985**, 318, 162.

(2) Liu, J. Science (Washington, DC, U. S.) **1998**, 280, 1253−1256.

(3) Goyal, R. N.; Gupta, V. K.; Bachheti, N. Anal. Chim. Acta **2007**, 597, 82−89.

(4) Csiszar, M.; Szucs, A˝ ; Tölgyesi, M.; Mechler, Á ; Nagy, J. B.; Novak, M.˙ J. Electroanal. Chem. **2001**, 497, 69−74

(5) Brus, L. E. J. Chem. Phys. **1984**, 80, 4403−4409.

(6) Iijima, S. Nature **1991**, 354, 56−58.

(7) Kim, K. S.; Zhao, Y.; Jang, H.; Lee, S. Y.; Kim, J. M.; Kim, K. S.; Ahn, J.-H.; Kim, P.;

Choi, J.-Y.; Hong, B. H. Nature **2009**, 457, 706− 710.

(8) Fu, L.; Yu, A. Rev. Adv. Mater. Sci. **2014**, 36, 40−61.

(9) Lv, R.; Cruz-Silva, E.; Terrones, M. ACS Nano **2014**, 8, 4061− 4069.

(10) Novoselov, K. S.; Geim, A. K.; Morozov, S. V.; Jiang, D.; Zhang, Y.; Dubonos, S. V.; Grigorieva, I. V.; Firsov, A. A. Science (Washington, DC, U. S.) **2004**, 306, 666−669.

(11) Mak, K. F.; Lee, C.; Hone, J.; Shan, J.; Heinz, T. F. Phys. Rev. Lett. **2010**, 105, 2−5.

(12) Kannan, P. K.; Late, D. J.; Morgan, H.; Rout, C. S. Nanoscale 2015, 7, 13293−13312.

(13) Rao, C. N. R.; Ramakrishna Matte, H. S. S.; Maitra, U. Angew. Chem., Int. Ed. **2013**, 52, 13162−13185.

(14) Xu, M.; Liang, T.; Shi, M.; Chen, H. Chem. Rev. **2013**, 113, 3766−3798.

(15) Naguib, M.; Kurtoglu, M.; Presser, V.; Lu, J.; Niu, J.; Heon, M.; Hultman, L.; Gogotsi, Y.; Barsoum, M. W. Adv. Mater. **2011**, 23, 4248−4253.

(16) Favier, F.; Walter, E. C.; Zach, M. P.; Benter, T.; Penner, R. M. Science (Washington, DC, U. S.) **2001**, 293, 2227−2231.

(17) Cui, Y. Science (Washington, DC, U. S.) 2001, 293, 1289−1292

(18) Chiang, C. K.; Fincher, C. R.; Park, Y. W.; Heeger, A. J.; Shirakawa, H.; Louis, E. J.; Gau, S. C.; MacDiarmid, A. G. Phys. Rev. Lett. **1977**, 39, 1098−1101.

(19) Knopfmacher, O.; Hammock, M. L.; Appleton, A. L.; Schwartz, G.; Mei, J.; Lei, T.; Pei, J.; Bao, Z. Nat. Commun. **2014**, 5, 2954.

(20) Schwartz, G.; Tee, B. C.-K.; Mei, J.; Appleton, A. L.; Kim, D. H.; Wang, H.; Bao, Z. Nat. Commun. **2013**, 4, 1859.

(21) Janata, J.; Josowicz, M. Nat. Mater. **2003**, 2, 19−24.

(22) Hangarter, C. M.; Chartuprayoon, N.; Hernandez, S. C.; Choa,´ Y.; Myung, N. V. Nano

Today **2013**, 8, 39.

(23) Yoon, H. Nanomaterials **2013**, 3, 524−549.

(24) Dallas, P.; Georgakilas, V. Adv. Colloid Interface Sci. **2015**, 224, 46−61.

(25) Wang, T.; Guo, Y.; Wan, P.; Zhang, H.; Chen, X.; Sun, X. Small **2016**, 12, 3748−3756.

(26) Park, S. J.; Kwon, O. S.; Lee, J. E.; Jang, J.; Yoon, H. Sensors **2014**, 14, 3604−3630

(27) Barsoukov, E.; Macdonald, J. R. *Impedance Spectroscopy: Theory, Experiment, and Applications*; **2005**.

Chapter 2

A Virus-Enabled Biosensor for Human Serum Albumin

This chapter was adapted from a research article (Ogata, Alana F; Edgar, Joshua M.; Majumdar, Sudipta; Briggs, Jeffrey S.; Patterson, Shae V.; Tan, Ming X.; Kudlacek, Stephan T.; Schneider, Christine A.; Weiss, Gregory A. *Analytical Chemistry*. **2017**, 89 (2), 1373-1381)

2.1 Introduction

Biosensor technologies that enable the rapid measurement of disease biomarkers in unprocessed biological samples, including blood, urine, saliva, and cerebrospinal fluids, remain elusive and highly sought. The ultimate goal are devices that can be used with minimal training by physicians and patients to provide actionable information at the point-of-care (PoC).[1-3] In addition to simplicity, analysis speed and sensitivity are critically important metrics for PoC biosensors but the technology must also provide for sensor-to-sensor reproducibility, manufacturability, and low cost.

A new approach to PoC detection of protein disease markers involves the use of virus particles, rather than antibodies, within a bioaffinity capture layer. Relative to antibodies, virus particles have several advantages that make them attractive for emerging PoC sensor technologies: First, virus particles can be engineered to bind virtually any protein – even toxic proteins for which antibody development is difficult.[4,5] Second, virus particles are less thermally and chemically labile than antibodies, dramatically simplifying the large-scale production, storage, and transport of biosensors that rely on virus–based bioaffinity layers.[6] Finally, virus particles that are capable of antibody-like affinities can be produced in quantity at lower costs.[7]

Here we describe a PoC biosensor that exploits electrodeposited bioaffinity layers that consist of a composite of virus particles with an electrically conductive polymer, poly(3,4 ethylenedioxythiophene) or PEDOT. The receptors in these biosensors are M13 virus particles. Peptides are "displayed" as fusions to the N-terminus of a subset of this virus' major P8 coat proteins that compose the virus capsid. From libraries of $>10^{11}$ unique sequences, the displayed peptide on the phage surface is selected based upon its target binding affinity and specificity. The use of whole virus particles as a bioaffinity matrix for biosensors dates to 2003, when it was

demonstrated that engineered M13 phage could be immobilized by physisorption onto the gold transducer of an acoustic wave sensor[8] and, somewhat later,[9] to a gold quartz crystal microbalance electrode, enabling the detection in both cases of β-galactosidase.[8,9] Subsequently, in 2007 Cosnier *et al.*[10] demonstrated biosensors based upon the virus T7 capable of detecting human antibodies to the West Nile virus.

Virus-PEDOT films provide a simple and reproducible method for immobilizing virus on an electrode that involves entraining it in a film of the conductive polymer PEDOT. We have demonstrated two types of biosensors based upon this bioaffinity matrix: virus-PEDOT nanowires prepared using the lithographically patterned nanowire electrodeposition (LPNE) process,[11,12] and virus-PEDOT films on planar gold electrodes.[13,14] Biosensors based upon virus-PEDOT nanowires transduce target binding using the through-nanowire resistance[11,12] whereas films of virus-PEDOT use electrical impedance spectroscopy (EIS) without added redox species to transduce the binding of a target molecule to the virus-PEDOT composite.[13,14] We have demonstrated that virus-PEDOT biosensors can detect prostate specific membrane antigen (PSMA), a 90 kDa glycoprotein that is a promising prostate cancer marker, with a limit-of-detection in synthetic urine of 0.50 nM.[14] These experiments establish the current baseline capabilities for this technology in terms of its sensitivity and limit-of-detection. But research grade gold electrodes, three-electrode potentiostats, and stand-alone reference and counter electrodes were employed in this prior work. How can this sensing modality be translated into manufacturable and minaturizable biosensor architectures and how well do these work in terms of sensitivity, signal-to-noise, and sensor-to-sensor reproducibility? We address these issues here for a problem of broad importance.

The analyte of interest in this study is human serum albumin (HSA, MW = 66.5 kDa) in urine. HSA is a well-established urinary biomarker that can indicate a wide range of adverse health conditions such as stroke, coronary artery disease, heart disease, renal disease, and liver or kidney failure, especially for those with diabetes.[15] In healthy adults, HSA is excreted in urine at a concentration below 20 mg/mL (or 300 nM).[16 17 18] HSA levels of 20 mg/L to 200 mg/L (300 nM to 3 µM) indicate microalbuminuria, a moderate increase in albumin related to a risk of kidney disease,[19 20] and patients with HSA concentrations above 200 mg/L are diagnosed with macroalbuminuria.[16 21] Current dipstick tests are only sensitive to macroalbuminuria, a diagnosis that usually occurs when kidney disease has irreversibly progressed to kidney failure.[19] Early detection of microalbuminuria through routine screening is imperative for a successful treatment plan that can be implemented in the beginning stages of kidney disease. This need for an accessible urinalysis test for HSA that is able to detect HSA over the range from < 20 mg/L to > 200 mg/L corresponding to < 300 nM to >3 µM.

In this study, we describe the label-free detection of human serum albumin (HSA) in aqueous buffer using a simple, monolithic, two-electrode electrochemical biosensor. In this device, both millimeter-scale electrodes are coated with a thin layer of the virus-PEDOT composite. The resistance component of the electrical impedance measured between these two electrodes, Z_{re}, provides electrical transduction of HSA binding to the virus-PEDOT composite. The analysis of sample volumes as small as 50 µL is made possible using a microfluidic cell. Upon exposure to HSA, virus-PEDOT films show a prompt increase in Z_{re} within 5 s and a stable Z_{re} signal within 5 min. HSA concentrations in the range from 100 nM to 5 µM are detectable using this biosensor. Sensor-to-sensor reproducibility of the HSA measurement is characterized by a

Table 2.1. Summary of Related Biosensing Literature involving Virus-Biosensors and/or HSA.

Detection method[1]	**Analyte**	**Bioaffinity Surface**	**Range**	**LOD_{exp}**	**Inter/Intra assay**	**Total analysis time**	**Ref**
Immuno-inhibition assay	HSA	PCS-modified latex particles incorporating HSA antibody	75.19 nM - 3.76 µM	6.02 nM (calc.)	Inter <10% N=20	N/A	[26]
QCM	HSA	Quartz crystal coated with polystyrene solution for direct HSA antibody adsorption.	15.04 nM – 3.76 µM	15.04 nM (meas.)	N/A	2 hr	[27]
EIS	HSA	HSA antibody immobilized on functionalized Si_3N_4 substrate.	10 pM to 10 µM	0.1 fM (calc.)	Inter 7.6% N=3	1 hr	[28]
DPV and EIS ($Fe(CN)_6$)	HSA (blood sample)	HSA molecularly imprinted polymer.	DPV: 12 nM - 300 nM EIS: 60 nM - 1200 nM	DPV:24 9 pM (calc.) EIS : 12 nM (calc.)	N/A	1 hr	[29]
DPV	HSA	HSA antibody modified gold nanoparticles immobilized on screen printed carbon electrode surfaces.	37 nM -3 µM	376 pM (calc.)	Intra 3.5% N=8 Inter 5% N=3	N/A	[30]
EIS	HSA	Modified glass surface with 3-aminopropyltriethoxysilane and HSA antibody in between two gold electrodes	3.01 nM - 90 µM	3 nM (meas.)	N/A	1 hr	[31]
EIS ($Fe(CN)_6$)	Cancer Cells	Octapeptide fused phage immobilized by layer-by-layer assembly onto gold electrodes	200-2.0E8 cells/mL	79 cells/mL (calc.)	Inter 4.9% N=5	1 hr	[32]
EIS ($Fe(CN)_6$)	HSA	HSA antibodies immobilized onto electropolymerized polytyramine films using a glutaraldehyde cross linker.	27.6 pM – 5.54 nM	24 pM (calc.)	Inter 9.2% N=4 Intra 11.4% N=5	50 min	[33]
EIS	**HSA**	**Virus-PEDOT composite film**	**100 nM – 5 µM**	**100 nM (meas.)**	**Intra 1.71-3.9% N=5 Inter 2%-8% N=3**	**< 10 min**	**This work**

[1] Abbreviations: HSA: human serum albumin, BSA: bovine serum albumin, QSM: quartz crystal microbalance, EIS: electrochemical impedance spectroscopy, DPV: differential pulse voltammetry, PCS: poly(chloromethyl)styrene, PEDOT: poly(3,4 thiophene)

coefficient of variance (COV) ranging from 2-8% across this concentration range. A comparison the current work compared to relevant prior biosensor studies is summarized in Table 2.1.

2.2 Experimental Considerations

2.2.1 Materials

All chemicals and solvents were purchased from Sigma Aldrich and used as received, unless noted. Nichromix solutions (Godax Laboratories) were prepared in sulfuric acid (Macron Fine Chemicals) by package directions. Positive photoresist (Shipley S-1827) and developer MF-219 (Microchem Corporation), gold pellets (5 N purity, Kurt J. Lesker Co.), and chromium powder (3 N purity, American Elements) were used for the photolithography of gold films. Devices were O_2 plasma cleaned using a basic plasma cleaner (PDC-32G, Harrick Plasma). Flow cells were designed and manufactured by Wainamics Inc., Fremont CA. Milli-Q UV water (ρ >18 MΩ cm) was used as the solvent for all aqueous solutions. Phosphate-buffered saline (PBS) buffer (137 mM NaCl, 2.7 mM KCl, 10 mM Na_2HPO_4, 1.8 mM KH_2PO_4 pH 8) was filtered through a 0.22 µM pore size membrane (Corning). The wash buffer was 0.1% Tween 20 (Fisher Scientific) in PBS. 2 mg/mL of Casein in PBS was used as blocking solution. Human serum albumin (HSA) of purity >97% based on SDS-PAGE was used as received. Bovine serum albumin (BSA, Calbiochem Omnipur) was used as received. The buffer for all blank and analyte solutions used for EIS measurement contained 2 mg/mL casein and 0.1% Tween 20 (henceforth “tween”) in PBS buffer. Synthetic urine (Ricca Chemical Co.) solutions composed of 18.01 g/mol water, 60.05 g/mol urea, 58.44 g/mol sodium chloride, magnesium sulfate heptahydrate, and 147.02 g/mol calcium chloride dihydrate.

2.2.2 Phage Library Design and the Selection of HSA Binders

The procedures associated with design of the phage library and the selection of HSA binders from this library are both described in the Appendix A section A.6.

2.2.3 Device Fabrication

Gold-film electrodes on glass substrate were fabricated by photolithography (Figure A.1). 1 in. by 1 in. glass slides were soaked in nichromix solution overnight, rinsed with Millie Q-UV water, and dried with pure air. Each slide was spincoated with positive photoresist and baked in a 90 °C oven for 30 min. The slides were then patterned using a contact photomask, 365 nm UV light source, and alignment stage (Newport, 83210i-line, 4 s), developed (MF-319), and rinsed with Millie Q-UV water. A 2 nm thick layer of chromium followed by a 60 nm thick layer of gold were thermally evaporated onto the slides. The slides were then soaked in acetone and sonicated for 10 min to lift off the photoresist layer and subsequently rinsed with Millie Q-UV water. Each 1 in by 1 in slide contained three pairs of gold electrodes, and were cut into three separate devices.

2.2.4 Synthesis of Phage-PEDOT Films

Gold-film electrodes and flow cells were cleaned by O_2 plasma for 10 min prior to electroplating. The flow cell was then mounted on the gold-film electrodes. A flame-cleaned platinum foil counter electrode – wrapped around a mercurous sulfate electrode (MSE) – was used during electropolymerization. Film growth occurred by cycling between 0.2 V and 0.8 using a PalmSens3 controlled by a PS-Trace software (PalmSens BV, Houten, Netherlands) at a scan rate of 20 mV/s in plating solution. Gold-film electrodes were first exposed to EDOT plating solution (12.5 mM $LiClO_4$, 2.5 mM EDOT) for 2 cycles of electropolymerization. Electrodes were then

exposed to phage-EDOT plating solution (8 nM M13 bacteriophage, 12.5 mM $LiClO_4$, 2.5 mM EDOT) and electropolymerized for 2 cycles. Electropolymerization of phage-EDOT was repeated with new phage-EDOT plating solution three times for a total of 8 cycles.

2.2.5 Electrochemical Impedance Spectroscopy

Various concentrations of HSA in run buffer (casein, tween, PBS) were prepared immediately prior to exposure of phage electrodes. Newly plated phage-PEDOT films were exposed to blocking solution (casein, PBS) for 15 min followed by rinsing with wash buffer (PBS, tween). The electrode was then rinsed three times with run buffer and allowed to equilibrate while monitoring the impedance signal over time. Equilibration was determined by having less than 1 Ω of change over a 2 min period. Once equilibration was reached, five consecutive EIS measurements were taken using a PalmSens3 controlled by a PS-Trace software (PalmSens BV, Houten, Netherlands). The amplitude of the applied voltage was 10 mV, and 50 data points were acquired spanning a frequency range of 5 Hz to 40 kHz. Phage electrodes were then exposed to HSA solutions in run buffer, monitored for equilibration, and five consecutive EIS measurements were collected. Independent electrodes were used for EIS measurements of HSA solutions and BSA solutions for a positive and negative response, respectively.

2.2.6 AFM and SEM Analysis

Scanning electron microscopy (SEM) was performed on uncoated films using a FEI Magellan 400L XHR SEM operating at 2 keV. Atomic force microscopy (AFM) images of PEDOT-only and phage-PEDOT films were acquired using an Asylum MFP-3D-SA atomic force microscopy (Asylum Research, Santa Barbara, CA) equipped with Olympus AC160TSAFM tips

(Olympus) in laboratory ambient air. AC Mode AFM images were obtained over a 20 μm range at 512 x 512 pixels. Images and amplitude traces were analyzed using the Asylum image processing software.

2.3 Results and Discussion

2.3.1 Electrodeposition and Characterization of virus-PEDOT Films

We describe a biosensor that consists of a pair of gold electrodes lithographically patterned onto a microscope slide, mated to a flow cell (Figure 2.1a). The flow cell, in three parts, is assembled on the sensor electrode before electrodeposition of the virus-PEDOT bioaffinity layer (Figure 2.1b). Each of the two gold electrodes is 1 mm x 3 mm, and the two electrodes are separated by 50 μm (Figure 2.1c). These electrodes span the 3 mm width of the flow channel from edge to edge, and are centered along its 2.3 mm length (Figure 2.1d). Plating and sample solutions are introduced into the 75 μL reservoir at top (Figure 2.1e), and the 6 μL volume of the flow channel quickly fills by capillary action. Both gold electrodes are modified with identical virus-PEDOT films that serve as bioaffinity layers. The virus incorporated into the PEDOT film is engineered[22] to selectively bind HSA with an affinity in the 10-100 nM range, as estimated using enzyme-linked immunosorbent assay (ELISA, Figure 2S).

The sensor operates without counter and reference electrodes, but these additional electrodes were used for the electrodeposition of virus-PEDOT films. Both virus-PEDOT films were electrodeposited simultaneously using an aqueous plating solution containing 8 nM virus, 2.5 mM EDOT, and 12.5 mM $NaClO_4$. Ten voltammetric scans from +0.80 V to +0.20 V vs. MSE (Figure 2.2a) were used for the preparation of each pair of films and the plating solution within the

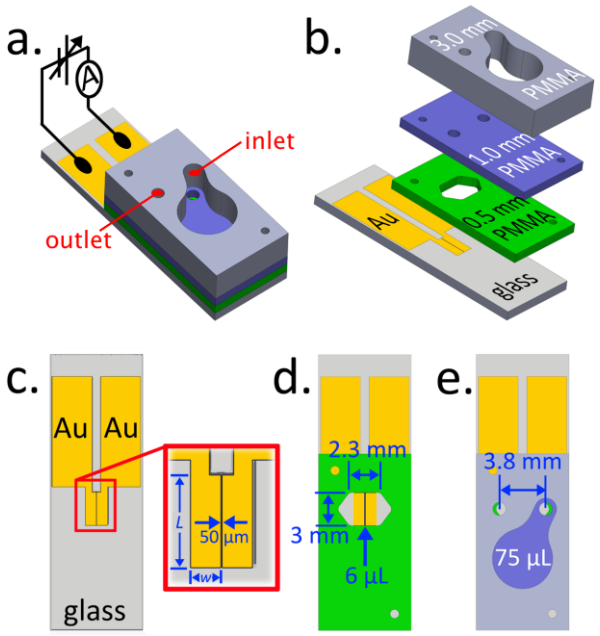

Figure 2.1. Schematic diagrams of the biosensor and the flow cell described in this study. (a) An assembled flow cell attached to a gold-electrode device consists of two gold contacts connected to a potentiostat for EIS measurements. (b) A gold-electrode device and detailed structure of a single PMMA flow cell; (c) a single device with a red box showing the two planar gold electrodes used for sensing. The two gold electrodes have a length (*L*) of 2 mm, width (*w*) of 0.85 mm, and are separated by a 50 µm gap. (d) Dimensions of the first PMMA flow cell layer which creates a cell holding 6 µL of solution over the gold electrodes; (e) Top view representation of assembled flow cell. Solution flows from the inlet port (right), through the cell, and exits through the outlet port (left) into a reservoir with a 75 µL capacity.

flow cell, which was quiescent during the deposition process, was replaced every two cycles. Electrodeposited virus-PEDOT films were a uniform dark blue in color (Figure 2.2c).

Scanning electron micrographs of pure PEDOT films prepared from the same plating solution without the addition of virus (Figure 2.2d) show a textured surface, dotted with 50-500 nm diameter protrusions. The apparent film thickness measured in the SEM is in the 200-300 nm range (Figure 2.2e). Virus-PEDOT films prepared from plating solution containing added 8 nM virus showed a surface with much greater roughness; the filamentous texture observed is characteristic of the virus-PEDOT composite (Figure 2.2f). At the film edge, SEM images acquired

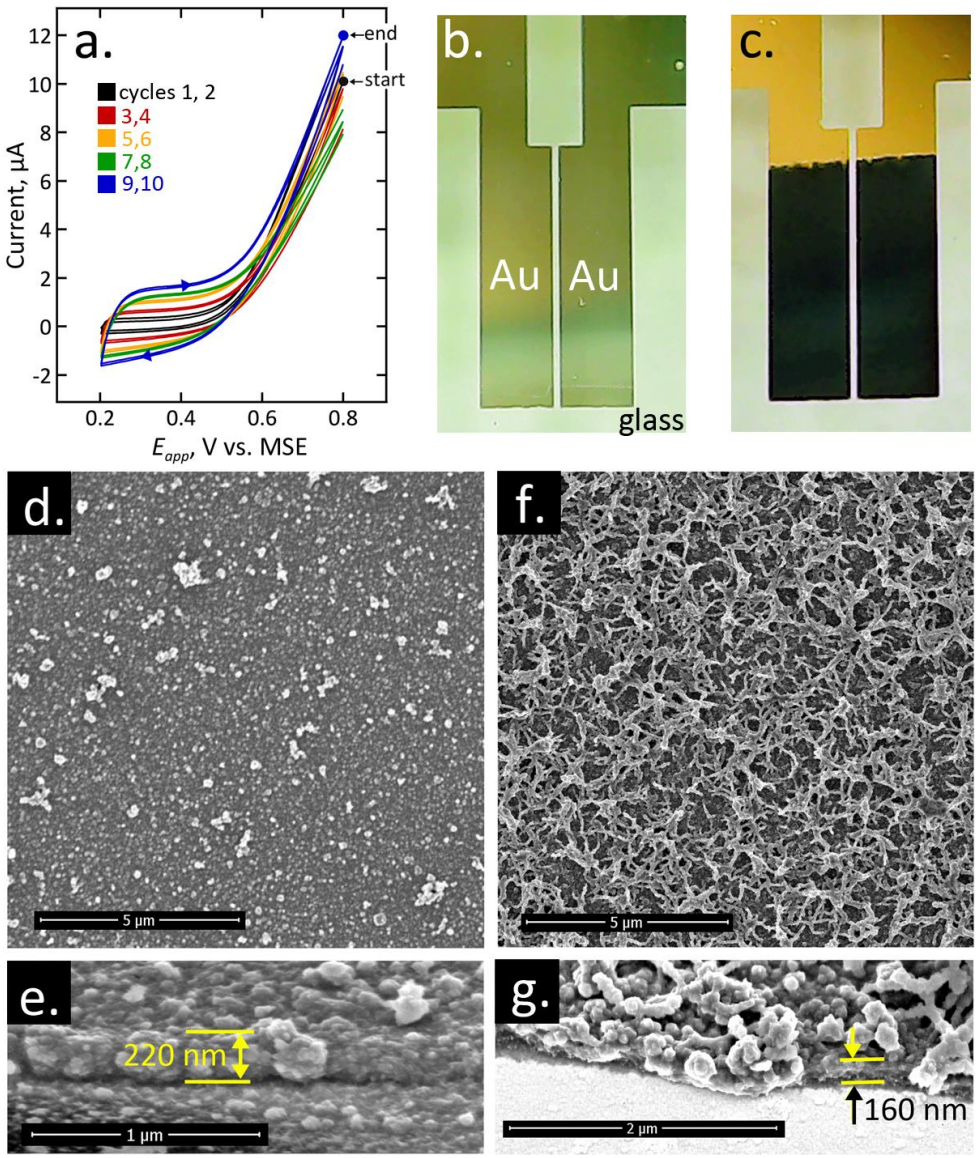

Figure 2.2. Electrodeposition and SEM characterization of virus-PEDOT bioaffinity coatings. (a) Electrodeposition of a virus-PEDOT film by cyclic voltammetry. Film prepared by two cycles in aqueous EDOT solution (2.5 mM EDOT, 12.5 mM $LiClO_4$) followed by eight cycles in a virus-EDOT solution (2.5 mM EDOT, 12.5 mM $LiClO_4$, 8 nM HSA phage). Virus-EDOT solution was replenished every two cycles. All scan rates were 20 mV/s. Optical image of: (b) bare gold electrodes and (c) gold electrodes after electrodeposition of virus-PEDOT film. (d,f,e,g) Scanning electron microscopy images of uncoated films. (d) PEDOT film prepared by ten consecutive cycles of deposition in aqueous EDOT solution (2.5 mM EDOT, 12.5 mM $LiClO_4$). (e) PEDOT edge showing film height of approximately 220 nm. (f) Virus-PEDOT film prepared as described in (a) showing dense incorporation of phage bundles on the surface. (g) Virus-PEDOT edge showing primer layer of PEDOT with thickness of approximately 160 nm and PEDOT-coated phage on top.

at high angular incidence of the electron beam show that a thin PEDOT layer of ≈150-180 nm is present on the gold surface and virus particles protrude from this PEDOT base layer like a shag carpet (Figure 2.2g). Several SEM images were obtained at random spots on the PEDOT-phage films and were visually identical, showing complete and uniform coverage over the gold electrodes.

Refreshing the plating solution every two scans dramatically increased the amount of virus present in the resulting virus-PEDOT films, as qualitatively assessed from these SEM images (Figure 2.2d,f and Figure A.2). Such difference in phage loading suggests that phage particles diffuse

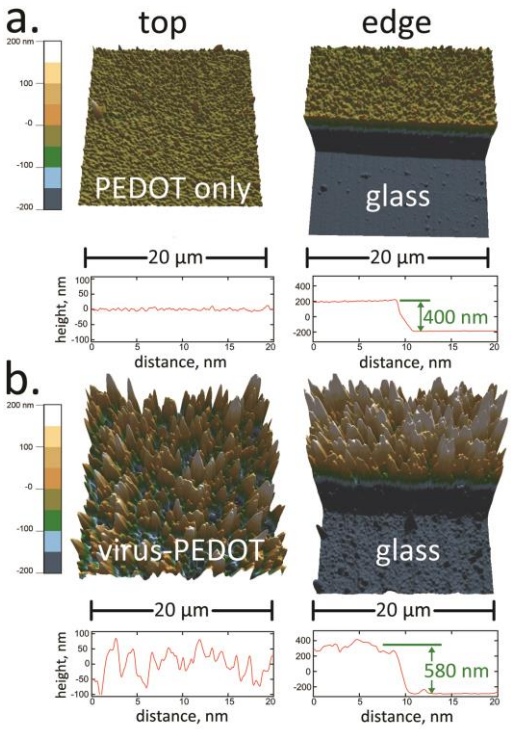

Figure 2.3. Atomic force microscopy of virus-PEDOT bioaffinity films and AFM line scans shown at the bottom. (a) PEDOT-only film prepared by ten cycles of deposition in EDOT solution (2.5 mM EDOT, 12.5 mM $LiClO_4$). Topography of the middle (left) and the edge (right) of films imaged by atomic force microscopy. The film-edge height shown in line scans includes the gold electrode layer (60 nm). (b) Virus-PEDOT film prepared by two cycles of deposition in EDOT solution followed by eight cycles in virus-EDOT solution (2.5 mM EDOT, 12.5 mM $LiClO_4$, 8 nM HSA phage); virus-EDOT solution replenished every two cycles. The rms roughness for PEDOT and virus-PEDOT films is ≈10 nm and ≈150 nm, respectively.

slowly to the surface of the electrode and are depleted within two cycles of deposition. An increase in phage loading enables high density of receptors on the phage-PEDOT sensors.

Atomic force microscopy (AFM) images of PEDOT only films prepared using this procedure (Figure 2.3a) allow for determination of the RMS surface roughness which is 15.596 nm. At the edges of the gold electrode (Figure 2,3a, right), the film thickness could be determined, and was in the range from 350 – 450 nm – significantly thicker than measured in the high vacuum environment of the SEM. We attribute the difference to the removal of water associated with film swelling in the SEM whereas films imaged by AFM were not subjected to high vacuum and likely retain a greater water content as a result. AFM images of virus-PEDOT films (Figure 2.3b) show a much more pronounced topography and a greater RMS roughness of 101.150 nm. The apparent film thickness for these films (Figure 2.3b, right) is in the range from 550 to 650 nm, but this value includes the PEDOT film and the protruding phage layer, that can not be distinguished in these images.

2.3.2 Detection of HSA in Buffer

We begin by comparing the impedance response of virus-PEDOT biosensors in BSA and HSA in order to ascertain the degree to which HSA can be selectively detected. BSA and HSA are identical in size (66.5 kDa) and have 76% sequence homology so this comparison provides a challenging test for HSA selectivity.[23] Nyquist plots (Z_{im} vs. Z_{re}) for virus-PEDOT films immersed in run buffer (Figure 2.4a) shows behavior characteristic of a series RC circuit, as expected. An equivalent circuit for the virus-PEDOT film quantitatively accounting for these observations is presented in the Supporting Information. The addition of 500 nM of BSA to the buffer causes a slight, 1-4 Ω, shift in this curve to higher Z_{re}, but almost no change in Z_{im}. For a different virus-

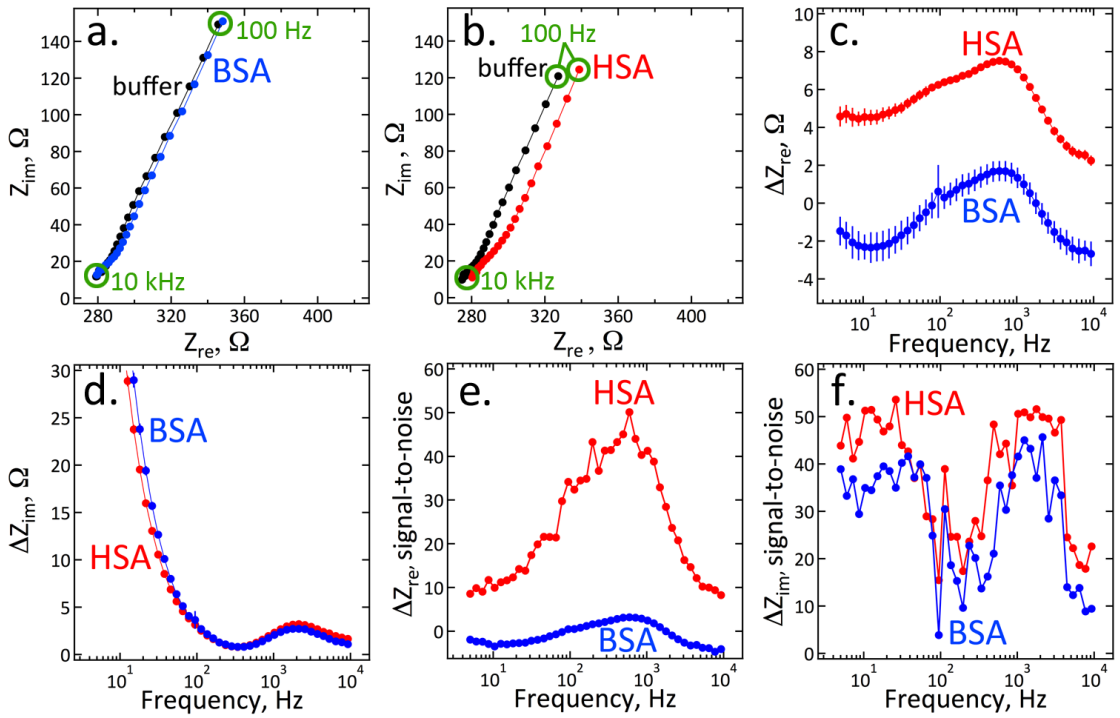

Figure 2.4. Detection of HSA binding using electrochemical impedance spectroscopy (EIS). The EIS response of virus-PEDOT biosensors upon exposure to 500 nM BSA (blue) and 500 nM HSA (red) is compared. No redox species are added to the solution in these measurements. Error bars represent the standard deviation, ±1σ, of five consecutive EIS measurements on a single electrode. (a,b) Nyquist plots for virus-PEDOT films in solutions of run buffer (black) and 500 nM BSA or HSA. Plots of (c) ΔZ_{re} and (d) ΔZ_{im} *versus* frequency, where ΔZ is defined as $Z_{analyte} - Z_{buffer}$. Corresponding (e) ΔZ_{re} and (f) ΔZ_{im} signal-to-noise ratio, defined as $\Delta Z/\sigma$, as a function of frequency.

PEDOT film (Figure 2.4b) a larger shift in Z_{re} of 8-10Ω, is observed upon exposure to 500 nM HSA in buffer and a much smaller shift is seen in Z_{im}. In all subsequent discussion, we refer to the shifts

in Z_{re} and Z_{im} relative to buffer as ΔZ_{re} and ΔZ_{im}. Plots of ΔZ_{re} and ΔZ_{im} versus frequency (Figures 2.4c and 2.4d) show that ΔZ_{re} is superior to ΔZ_{im} for detecting HSA at 500 nM across the entire frequency spectrum from 5 Hz to 10 kHz. The error bars shown in these two plots represent the standard deviation of the mean for multiple impedance measurements (n = 5) on a single biosensor. The measurement-to-measurement dispersion in impedance seen both for ΔZ_{re} and ΔZ_{im} is simply

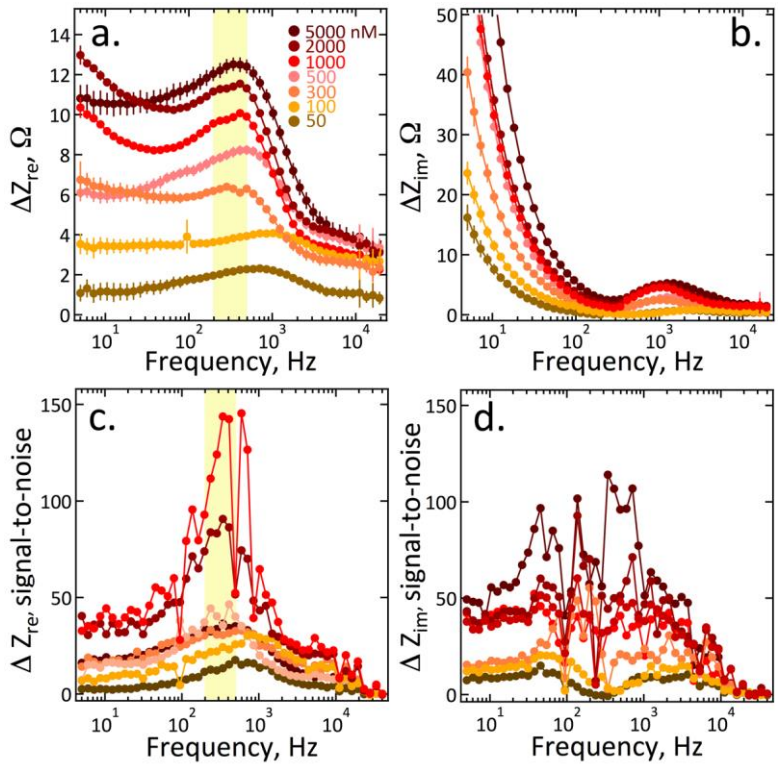

Figure 2.5. Measurement of ΔZ_{re} affords superior signal-to-noise (S/N) compared with measurement of ΔZ_{im}. Calibration plots of (a) ΔZ_{re} and (b) ΔZ_{im} versus frequency for virus-PEDOT films in varying concentrations of HSA in run buffer. Each HSA concentration was measured using a different biosensor. Errors bars are defined as the standard deviation, $\pm 1\sigma$, of five consecutive impedance measurements on a single electrode. (c) the relative S/N, defined as $\Delta Z_{re}/\sigma$, *versus* frequency for ΔZ_{re}, and, d) the relative S/N, defined as $\Delta Z_{im}/\sigma$, *versus* frequency for ΔZ_{im}.

noise, and a signal-to-noise ratio (*S/N*) can therefore be calculated at each frequency point as: $\Delta Z_{re}/\sigma_{re}$ and $\Delta Z_{im}/\sigma_{im}$ (Figure 2.4e and2. 4f) where σ_{re} is the standard deviation of ΔZ_{re} across these five EIS measurements at each frequency. These plots show that for ΔZ_{re} (Figure 2.4e) a *S/N* of 50 is obtained at 500-600 Hz for HSA whereas BSA at the same 500 nM concentration and frequency is detected with a *S/N* of 1-3. For ΔZ_{im}, on the other hand (Figure 2.4e), both HSA and BSA produce a comparable *S/N* ranging from 10-50 across the frequency spectrum. The tentative conclusion is that measurement of ΔZ_{re} is superior to ΔZ_{im} for the detection of HSA under these conditions. Since ΔZ_{re} represents the change in resistance of the virus-PEDOT layer, and ΔZ_{im}, is

the change in the quantity $(\omega C)^{-1}$ where ω is the angular frequency and C is the capacitance the resistance of the virus-PEDOT bioaffinity layer, we conclude that the resistance of the virus-PEDOT layer is preferentially perturbed by HSA binding, relative to the capacitance.

The extension of these EIS measurements to a range of HSA concentrations from 50 nM to 2 μM (Figure 2.5) confirms that ΔZ_{re} increases monotonically with HSA concentration from 50 nM to 5 μM. The peak *S/N* of 20-140 for this response occurs in the range from 200-500 Hz. Below 100 Hz, ΔZ_{im} shows an even larger increase with increasing HSA concentration – as high as 50 Ω - but noise is also more prominent and the resulting *S/N* is lower than seen for ΔZ_{re}. A more serious problem is that no single frequency provides reliable HSA quantitation across this HSA concentration range using ΔZ_{im}. In addition to sensitivity and signal-to-noise, the speed of biosensor response is also critically important. Real time measurements of ΔZ_{re} at f = 340 Hz (Figure 2.6) show that increasing the HSA concentration in the flow cell causes a prompt increase in ΔZ_{re} on the 5 s time scale followed by a slower increase in ΔZ_{re} over the next 200 s or so. Using the slower of these two time-scales, a single measurement comprising exposure to buffer and then to sample can be accomplished in ≈8-10 min.

The sensor-to-sensor reproducibility for HSA detection can be assessed by making repetitive measurements of HSA at a particular concentration using different sensors. The impedance versus frequency data shown in Figure 2.7a (for ΔZ_{re}) and b (for ΔZ_{im}) show error bars representing coefficient-of-variation (COV) for measurements at three different biosensors at each concentration. For ΔZ_{re} in the frequency range from 200-500 Hz, no overlap of these error bars occurs between the seven concentration plots, suggesting that the biosensor cleanly resolves these seven concentrations. COV values are minimized for all concentrations in the 200-500 Hz window

(F

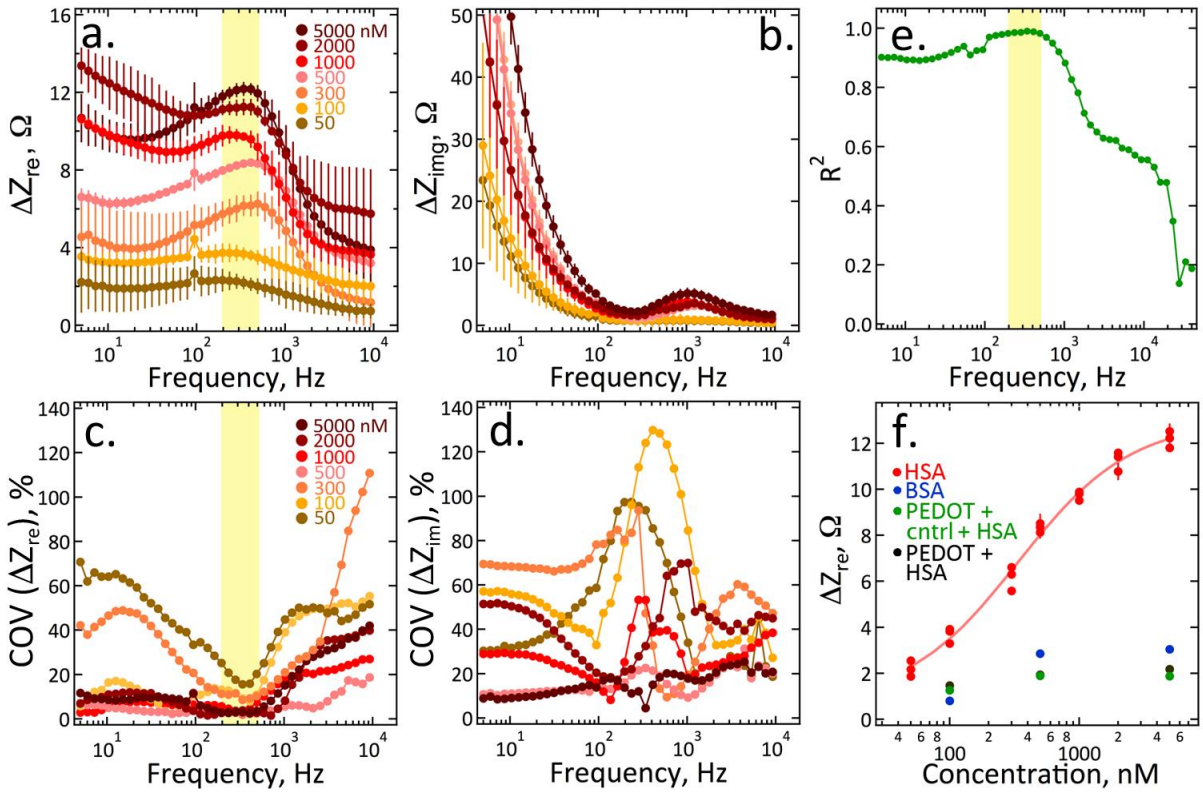

Figure 2.6. Sensor-to-sensor reproducibility of HSA detection. Calibration plot of (a) ΔZ_{re}, and (b) ΔZ_{im} *versus* frequency for multiple virus-PEDOT films exposed to varying concentrations of HSA. ΔZ values for n = 3 independent virus-PEDOT electrodes were averaged to obtain each curve, errors bars indicate, ±1σ. Corresponding coefficient of variation, defined as the relative standard deviation for n=3 virus-PEDOT electrodes of (c) ΔZ_{re} and (d) ΔZ_{im} versus frequency plots for each HSA concentration. ΔZ_{re} shows regions of COV values < 20 % while, ΔZ_{im} COV values are too high for reliable measurements. At each frequency, ΔZ_{re} versus [HSA] was fitted to the Hill equation and the square of the regression coefficient, R^2, versus frequency plot (e). R^2 = 1 represents the best fit of the Hill equation to the data. The highlighted interval in (a,c,e) indicates the frequency range where ΔZ_{re} signal is largest, COV is at a minimum, and the peak for goodness of fit occur, respectively. (f) Calibration plot of ΔZ_{re}, measured at 340 Hz, versus concentration. Each data point represents a different virus-PEDOT electrode with error bars defined as the standard deviation, ±1σ, of five consecutive impedance measurements. Impedance data for HSA exposures to virus-PEDOT films containing HSA (red) phage are fitted to the hill equation (red line). Three controls to confirm specific binding to HAS are shown: BSA exposure to virus-PEDOT films containing HSA binding phage (blue), HSA exposure to virus-PEDOT films containing a control phage having no affinity for HSA (green), and HSA exposure to pure PEDOT films containing no phage (black).

nM to 2 µM. For ΔZ_{im} on the other hand, error bars overlap across the frequency spectrum (Figure 6b) and larger COV values apply (Figure 6e) demonstrating again that ΔZ_{im} is a less effective discriminator of HSA than ΔZ_{re}.

While Figure 6a shows that ΔZ_{re} progresses to higher values as the HSA concentration increases, one can ask whether this progression conforms to the Hill Equation, which is expected to model the sensor response:[24]

$$\Delta Z_{re} = \Delta Z_{re,lim} + \frac{\Delta Z_{re,0} - \Delta Z_{re,lim}}{1 + \left(\frac{C_{HSA}}{K_D}\right)^{h}} \qquad \text{Eq (1)}$$

where $\Delta Z_{re,lim}$ is the limiting ΔZ_{re} seen at high HSA concentrations, $\Delta Z_{re,0}$ is the minimum value of ΔZ_{re} seen at low C_{HSA}, and K_D is the dissociation constant, which corresponds to the value of C_{HSA} at which $\Delta Z_{re} = (\Delta Z_{re,0} - \Delta Z_{re,lim})/2$. The Hill coefficient, h, equals 1.0 when no cooperativity is present, it has a positive value when positive cooperativity is operating (that is, $K_{D,app}$ increases with HSA loading) and it has a negative value when negative cooperativity is indicated.[24] The R^2 value computed for the best 4-parameter fit of Eq. (1) to the data of Figure 2.6a is plotted in Figure 2.6c. R^2 when > 0.9 is seen for all frequencies below 800 Hz, and $R^2 > 0.95$ is observed in the frequency range 200-500 Hz (yellow). The calibration of phage-PEDOT biosensors will ultimately be determined at a single frequency. Based on the maximum signal-to-noise ratio, minimum COV, and maximum R^2 fits to the Hill equation, the frequency of choice is 340 Hz. Using f = 340 Hz, for example, the ΔZ_{re} versus C_{HSA} calibration curve shown in Figure 2.6f is obtained. A summary of the Hill equation fit parameters for ΔZ_{re} is summarized in Table A.4. The Hill coefficient of h

= 1.0 ± 0.2 indicates that there is no cooperativity in phage-HSA binding, consistent with previous studies.[14]

Nonspecific adsorption is well-controlled by casein blocking of these virus-PEDOT films. Blue data points in Figure 2.6f are BSA while green and black data points represent measurements of HSA conducted using a Stop 4 phage which has no measurable affinity to HSA (green), and a pure PEDOT film containing no phage (black). Phage-PEDOT films do show slight non-specific binding to BSA. Therefore, a conservative limit of detection for phage-PEDOT films is 100 nM HSA. Corresponding COV values for 100 nM - 5 µM HSA are within 2% - 8%. Nonspecific binding is attributed to electrostatic interactions between proteins and the positively charged PEDOT backbone. The isoelectric point of HSA and BSA is ~5, rendering the proteins negatively

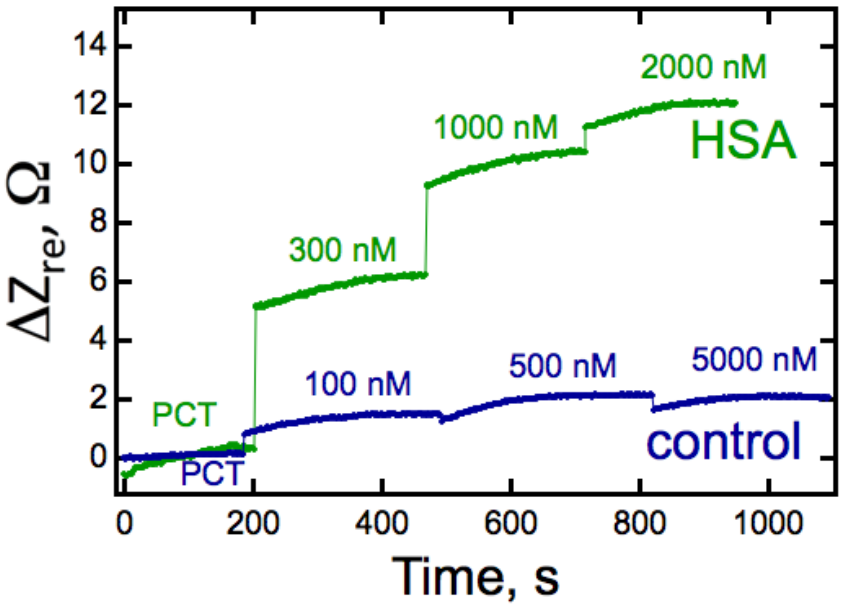

Figure 2.7. Real-time HSA biosensing. Plot of ΔZ_{re} *verus* time, of a single virus-PEDOT, using a control virus that did not bind HSA (blue) and HSA virus (green), electrode when exposed to three concentrations of HSA. A freshly electrodeposited virus-PEDOT film was first immersed in run buffer (PBS-casein-tween) until reaching an equilibration signal. The time scan was then paused and five EIS spectra were acquired in rapid succession. Immediately following this, the virus-PEDOT film was exposed to 100 nM HSA in run buffer and the time scan was restarted within 5 seconds of exposure. This procedure was repeated for exposures to 500 nM and 5000 nM HSA.

charged in solutions with pH values above 5 such as buffer solutions (pH=8) used in phage-HSA sensing. Figure A.3 demonstrates that lowering the pH of buffer solution suppresses the negative charge on BSA and results in a decrease of non-specific binding with the inherently positive PEDOT-only film. The addition of casein blocking solution similarly inhibits non-specific adsorption compared to sensing in pH 5 buffer. While casein is an effective blocking agent for phage-PEDOT films, it can also block binding sights and suppress sensor response. Such effects are apparent in the observed K_D of phage-PEDOT biosensors, which is slightly higher than K_D = 10 nM - 100 nM obtained by ELISA immunosorbent assays.

2.3.3 Detection of HSA in Synthetic Urine

To validate phage-PEDOT sensor capabilities for urine analysis, EIS measurements for HSA detection were repeated in synthetic, buffered urine. Casein blocking was not implemented in synthetic urine sensing experiments. Negative controls in synthetic urine show little non-specific binding in agreement with previous studies that show synthetic urine improves specificity.[14] Urea disrupts protein interactions and mimics the blocking activity of casein which mitigates the non-specific binding of HSA and BSA. Phage-PEDOT sensors in synthetic urine demonstrated a concentration dependent response to HSA similar to buffer (Figure 2.8a). Sensor-to-sensor reproducibility in synthetic urine is maintained at <10 % COV centered around 100 Hz (Figure 2.8b). Optimal frequency point for calibrating virus-PEDOT films in synthetic urine was 136 Hz (Figure 2.8c) based on the maximum signal-to-noise ratio, minimum COV, and maximum R^2 fits to the Hill equation (Figure A.5). Although the impedance response in synthetic urine and buffer follow a similar trend, assessment of the Hill equation reveals significant differences in the fit parameters (Table 2.2). In synthetic urine sensitivity decreases by an order of magnitude and

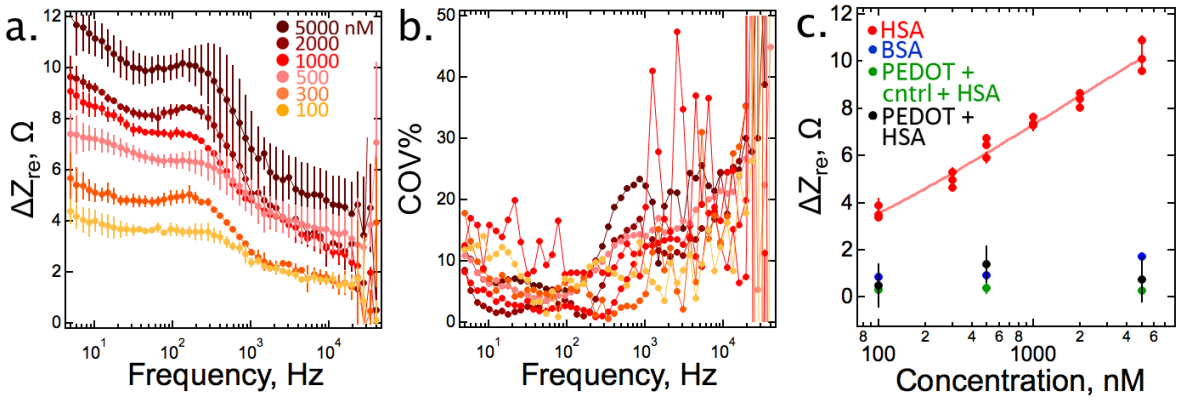

Figure 2.8. Virus-PEDOT sensors in synthetic urine. Calibration plot of (a) ΔZ_{re} versus frequency for multiple virus-PEDOT films exposed to varying concentrations of HSA. ΔZ values for n = 3 independent virus-PEDOT electrodes were averaged to obtain each curve, errors bars indicate, ±1σ. (b) Corresponding coefficient of variation (COV), defined as the relative standard deviation for n=3 virus-PEDOT electrodes of ΔZ_{re} *versus* frequency plots for each HSA concentration. (c) Calibration plot of ΔZ_{re}, measured at 136 Hz, versus concentration. Each data point represents an independent virus-PEDOT electrode with error bars defined as the standard deviation, ±1σ, of five consecutive impedance measurements. Impedance data for HSA exposures to virus-PEDOT films containing HSA (red) phage are fitted to the hill equation (red line). Three controls to confirm specific binding to HSA are shown: BSA exposure to virus-PEDOT films containing HAS phage (blue), HSA exposure to virus-PEDOT films containing a control phage that did not bind HSA (green), and HSA exposure to pure PEDOT films containing no phage (black).

Table 2.2 Parameters for the Best Fit of the Hill Equation (Eq. 1) to HSA Calibration Curves Acquired in PBS Buffer and Synthetic Urine

	Frequency (Hz)	$\Delta Z_{re,0}$ (Ω)	$\Delta Z_{re,lim}$ (Ω)	K_D (nM)	h
PBS	340	0.4 ± 1	12.2 ± 0.5	300 ± 50	1.0 ± 0.2
Synthetic urine	136	1 x 10^{-16} ± 5	15 ± 8	1036 ± 1000	0.5 ± 0.5

the Hill coefficient indicates negative cooperativity binding of virus-PEDOT films to HSA. We attribute this to interactions between urea and the PEDOT backbone that induce a reduction-like reaction. Amines participate in a nucleophilic attack on the delocalized positive charge on PEDOT, displacing charge carriers, and decreasing the conductivity of the PEDOT film. The two amine

groups on urea enable such interactions with PEDOT to increase the film resistance and ultimately reduce efficiency in impedance sensing towards analytes.[25]

2.4 Summary

We describe a simple, monolithic, two-electrode electrochemical biosensor for the label-free detection of HSA in PBS buffer and synthetic urine. This biosensor relies upon phage-PEDOT bioaffinity layer that are electrodeposited on both electrodes. An EIS measurement of the shift in Z_{re} at an optimum frequency of ≈300 Hz is then used to transduce the binding of HSA. HSA concentrations in a physiologically relevant range of 100 nM to 5 μM were detected using this biosensor. The resulting calibration curves are well-described by the Hill equation for receptor-ligand binding. These single-use biosensors exhibit a sensor-to-sensor reproducibility characterized by a coefficient-of-variation of 2-8% across the entire concentration range. It is also demonstrated that phage-PEDOT biosensors are capable of HSA quantitation in synthetic urine. This simple biosensor architecture is readily manufacturable, is compatible with small sample volumes (≈ 50 μL), and affords rapid analysis times (< 15 min). All of these attributes provide motivation for the further development of this and related biosensing technologies.

2.5 Acknowledgments

R.M.P gratefully acknowledges the financial support of this work by the National Science Foundation, Chemistry Division through contract CHE-1306928. G.A.W. acknowledges support from the National Cancer Institute of the NIH (1R33CA206955-01), PhageTech Inc (PHAGE-203015), and Chao Family Comprehensive Cancer Center, UC Irvine. FE-SEM data were acquired using instrumentation of the LEXI facility (lexi.eng. uci.edu/) at UCI.

2.6 References

(1) Gubala, V.; Harris, L. F.; Ricco, A. J.; Tan, M. X.; Williams, D. E. *Anal. Chem.* **2012**, *84*, 487-515.

(2) Soper, S. A.; Brown, K.; Ellington, A.; Frazier, B.; Garcia-Manero, G.; Gau, V.; Gutman, S. I.; Hayes, D. F.; Korte, B.; Landers, J. L.; Larson, D.; Ligler, F.; Majumdar, A.; Mascini, M.; Nolte, D.; Rosenzweig, Z.; Wang, J.; Wilson, D. *Biosens. Bioelectron.* **2006**, *21*, 1932-1942.

(3) Luo, X. L.; Davis, J. J. *Chem. Soc. Rev.* **2013**, *42*, 5944-5962.

(4) Beekwilder, J.; Rakonjac, J.; Jongsma, M.; Bosch, D. *Gene* **1999**, *228*, 23-31.

(5) Pacheco, S.; Canton, E.; Zuniga-Navarrete, F.; Pecorari, F.; Bravo, A.; Soberon, M. *Amb Express* **2015**, *5*.

(6) Hayhurst, A.; Georgiou, G. *Curr. Opin. Chem. Biol.* **2001**, *5*, 683-689.

(7) Weiss, G. A.; Penner, R. M. *Anal. Chem.* **2008**, *80*, 3082-3089.

(8) Petrenko, V. A.; Vodyanoy, V. J. *J Microbiol. Meth.* **2003**, *53*, 253-262.

(9) Nanduri, V.; Sorokulova, I. B.; Samoylov, A. M.; Simonian, A. L.; Petrenko, V. A.; Vodyanoy, V. *Biosens. Bioelectron.* **2007**, *22*, 986-992.

(10) Ionescu, R. E.; Cosnier, S.; Herrmann, S.; Marks, R. S. *Anal Chem* **2007**, *79*, 8662-8668.

(11) Arter, J. A.; Diaz, J. E.; Donavan, K. C.; Yuan, T.; Penner, R. M.; Weiss, G. A. *Anal. Chem.* **2012**, *84*, 2776-2783.

(12) Arter, J. A.; Taggart, D. K.; McIntire, T. M.; Penner, R. M.; Weiss, G. A. *Nano. Lett.* **2010**, *10*, 4858-4862.

(13) Donavan, K. C.; Arter, J. A.; Pilolli, R.; Cioffi, N.; Weiss, G. A.; Penner, R. M. *Anal. Chem.* **2011**, *83*, 2420-2424.

(14) Mohan, K.; Donavan, K. C.; Arter, J. A.; Penner, R. M.; Weiss, G. A. *J. Am. Chem. Soc.* **2013**, *135*, 7761-7767.

(15) Meigs, J. B.; D'Agostino, R. B.; Nathan, D. M.; Rifai, N.; Wilson, P. W. F. *Diabetes Care* **2002**, *25*, 977-983.

(16) Wu, H. Y.; Peng, Y. S.; Chiang, C. K.; Huang, J. W.; Hung, K. Y.; Wu, K. D.; Tu, Y. K.; Chien, K. L. *JAMA. Intern. Med.* **2014**, *174*, 1108-1115.

(17) Chavers, B. M.; Mauer, S. M.; Ramsay, R. C.; Steffes, M. W. *Diabetes* **1994**, *43*, 441-446.

(18) Gross, J. L.; de Azevedo, M. J.; Silveiro, S. P.; Canani, L. H.; Caramori, M. L.; Zelmanovitz, T. *Diabetes Care* **2005**, *28*, 164-176.

(19) Viberti, G. C.; Hill, R. D.; Jarrett, R. J.; Argyropoulos, A.; Mahmud, U.; Keen, H. *Lancet* **1982**, *1*, 1430-1432.

(20) Watta, G. F. B. J. E. R., D. J.; Morris, R. W.; Gatting, W.; Polak, A. *Clin. Chem.* **1986**, *32*, 1544-1548.

(21) Jones, C. A.; Francis, M. E.; Eberhardt, M. S.; Chavers, B.; Coresh, J.; Engelgau, M.; Kusek, J. W.; Byrd-Holt, D.; Narayan, V.; Herman, W. H.; Jones, C. P.; Salive, M.; Agodoa, L. Y. *Am. J. Kidney. Dis.* **2002**, *39*, 445-459.

(22) Sidhu, S. S.; Lowman, H. B.; Cunningham, B. C.; Wells, J. A. *Methods Enzymol.* **2000**, *328*, 333-363.

(23) Huang, B. X.; Kim, H. Y.; Dass, C. *J. Am. Soc. Mass Spectrom.* **2004**, *15*, 1237-1247.

(24) Kurganov, B. I.; Lobanov, A. V.; Borisov, I. A.; Reshetilov, A. N. *Anal. Chim. Acta.* **2001**, *427*, 11-19.

(25) Hojati-Talemi, P.; Evans, D.; Fabretto, M. *Chem. Mater.* **2013**, *25*, 1837-1841.

(26) Thakkar, H.; Newman, D. J.; Holownia, F.; Davey, C. L.; Wang, C. C.; Lloyd, J. *Clin. Chem.* **1997**, *43*, 1471-1471.

(27) Sakti, S. P.; Hauptmann, P.; Zimmermann, B.; Buhling, F.; Ansorge, S. *Sens Actuators,B* **2001**, *78*, 257-262.

(28) Caballero, D.; Martinez, E.; Bausells, J.; Errachid, A.; Samitier, J. *Anal. Chim. Acta.* **2012**, *720*, 43-48.

(29) Cieplak, M.; Szwabinska, K.; Sosnowska, M.; Bikram, K. C. C.; Borowicz, P.; Noworyta, K.; D'Souza, F.; Kutner, W. *Biosens. Bioelectron.* **2015**, *74*, 960-966.

(30) Omidfar, K.; Dehdast, A.; Zarei, H.; Sourkohi, B. K.; Larijani, B. *Biosens. Bioelectron.* **2011**, *26*, 4177-4183.

(31) Chuang, Y. H.; Chang, Y. T.; Liu, K. L.; Chang, H. Y.; Yew, T. R. *Biosens. Bioelectron.* **2011**, *28*, 368-372.

(32) Han, L.; Liu, P.; Petrenko, V. A.; Liu, A. H. *Sci. Rep.* **2016**, *6*.

(33) Wu, Z. S.; Li, J. S.; Deng, T.; Luo, M. H.; Shen, G. L.; Yu, R. Q. *Anal. Biochem.* **2005**, *337*, 308-315.

Appendix A

Supplementary Information for Chapter 2

A.1. Process flow for lithographic preparation of gold electrodes

Figure A.1 shows a process flow of lithographically patterned gold films. A detailed description is described in the text.

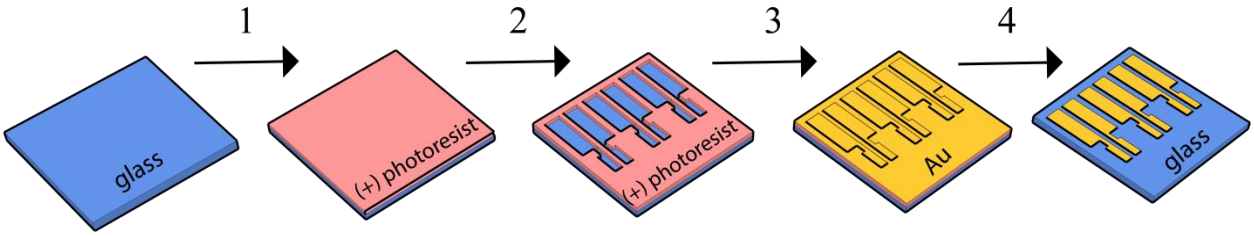

Figure A.1. Schematic diagram of gold film electrodes prepared by photolithography. (1) Positive photoresist is spin coated onto a glass substrate, (2) the photoresist is patterned by a photomask and developed, (3) slides are coated with thermally-evaporated gold, (4) and lift off is performed.

A.2. Enzyme linked immunosorbent assay

Figure A.2 shows an enzyme-linked immunosorbent assay for HSA phage binding. Ligand binding is compared to the negative control Stop-4 phage, which shows significantly less binding activity.

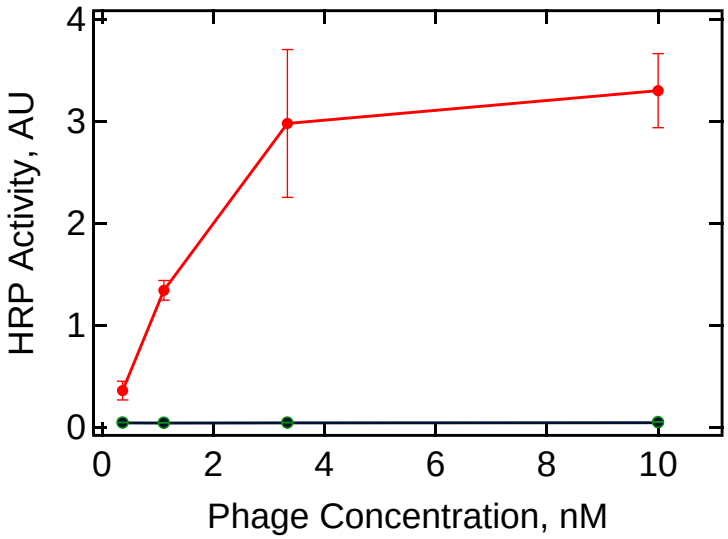

Figure A.2. A phage-based ELISA for HSA phage binding. (red) HSA-phage binding to HSA compared to two negative controls, (black) HSA-phage binding to BSA and (dotted green) Stop-4 phage binding to HSA.

A.3. Effect of pH and blocking agents on non-specific binding

Figure A.3 shows a plot of the change in Z_{re} at 340 Hz when exposed to 500 nM BSA under various conditions. Preventing non-specific binding is a critical challenge for non-faradaic impedance based biosensors; in this study pH and blocking agents were explored. Non-specific binding was characterized by exposing a PEDOT film to BSA protein in various buffers. Initial studies of PEDOT films in PBS buffer at pH 8 shows significant non-specific binding to BSA. This response from non-specific binding is reduced as the pH of the buffer is decreased, suggesting that non-specific binding is caused by electrostatic interactions between the positively-charged PEDOT and BSA protein. Non-specific was also reduced by addition of a blocking agent, casein. At pH 8, PEDOT films that were blocked with casein in PBS show less response from BSA than PEDOT films that were not blocked.

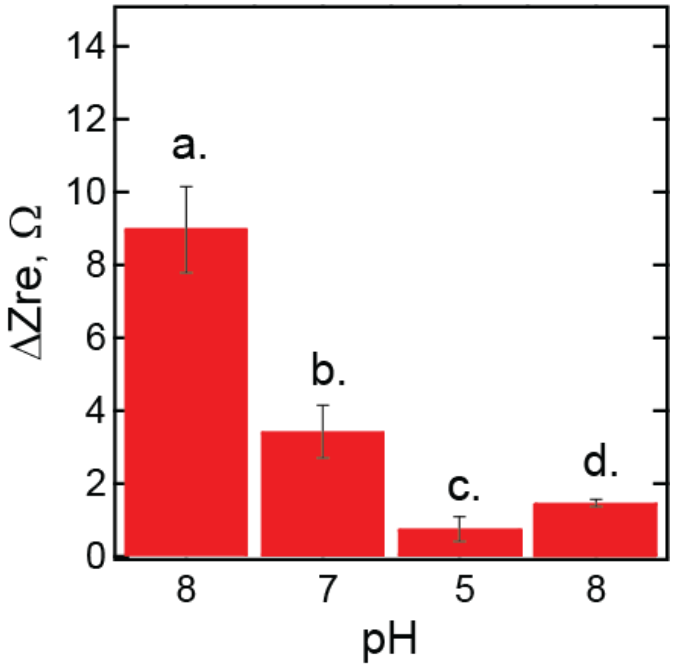

Figure A.3**.** Bar plot of ΔZ_{re} for PEDOT films to determine optimal buffer conditions for reduced non-specific binding. (a-c) PEDOT films, at varying pH's, were equilibrated in PBS and then exposed to 500 nM BSA in PBS. (d) A PEDOT film was blocked with casein in PBS for 15 minutes, equilibrated in PCT, and exposed to 500 nM BSA in PCT at pH 8. Lowering the buffer pH or implementing a casein blocking agent significantly reduced non-specific binding.

A.4. An equivalent circuit for virus-PEDOT films

Figure A.4 shows an equivalent circuit corresponding to virus-PEDOT films on two gold electrodes. R_1, C_2 , R_2, and C_3 represent the two virus-PEDOT films where most of the change induced by HSA binding is in the two resistors.

Table A.1. Values for elements in the equivalent circuit

Solution	**C_1 ($x10^{-9}$ F)**	**R_1 (Ω)**	**C_2 ($x10^{-6}$ F)**	**R_2 (Ω)**	**C_3 ($x10^{-5}$ F)**	**Q_1 ($x10^{-4}$ F)**	**n_1**	**R_3 (Ω)**	**Q_2 ($x10^{-5}$ F)**	**n_2**
PCT	2.0 ± 0.4	90 ± 12	7.4 ± 0.4	276 ± 3	3.1 ± 0.5	9 ± 15	0.8 ± .2	92 ± 13	1.41 ± .04	0.710 ± .006
500 nM HSA	2.4 ± 0.6	95 ± 9	6.2 ± 0.5	278 ± 3	3.2 ± 0.8	9 ± 9	0.8 ± 0.4	100 ± 11	1.37 ± 0.05	0.993 ± .008
Change	+ 0.5	+ 5	- 1.2	+ 2	+ 0.1	- 2	0.0	+ 8	- 0.04	+ 1.53

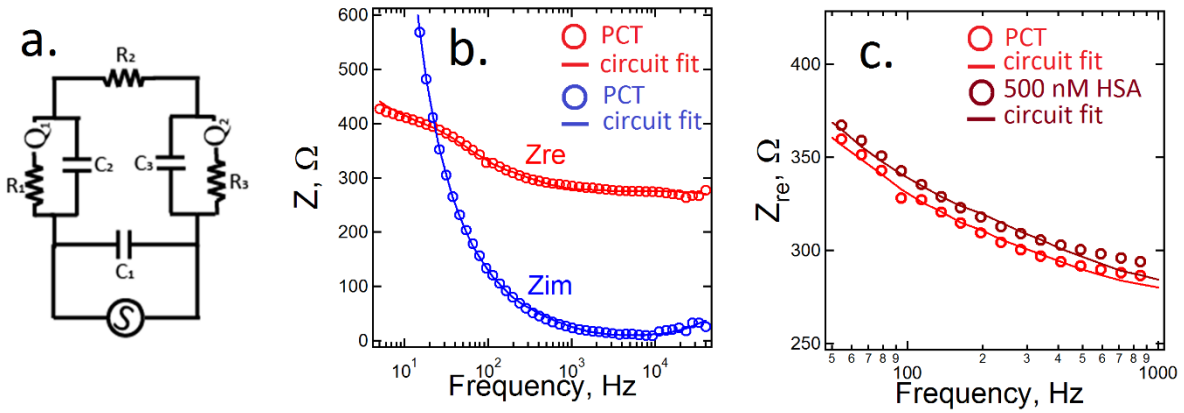

Figure A.4. (a) Diagram of an equivalent circuit used to model virus-PEDOT films on two planar-gold electrodes. Circuit elements represent: capacitance between the two electrodes (C_1), the solution resistance of PBS buffer (R_2), the impedance imposed by one virus-PEDOT film (R_1,C_2, Q_1), and the impedance imposed by the second virus-PEDOT film (R_3, C_3, Q_2). (b) Plot of impedance versus frequency for Z_{re} (red) and Z_{im} (blue). The simulated impedance (solid line) data produced by the parameters in Table S1 is plotted on top of the raw impedance data (open circle) of a virus-PEDOT film in PCT buffer. (c) Plot of Z_{re} versus frequency for the range of frequencies,50 Hz to 10 kHz, where a response to HSA binding is observed. Both the raw and simulated data show an increase in impedance from virus-PEDOT films in PCT buffer (red) to 500 nM HSA in PCT buffer (dark red).

A.5. HSA sensing in synthetic urine

Figure A.5 includes analysis of signal-to-noise and R^2 values for the Hill equation for virus-PEDOT films in synthetic urine. ΔZ_{re} increases monotonically with HSA concentration from 100 nM to 5 µM in synthetic urine. Peak ΔZ_{re} response, signal-to-nose, and $R^2 > 0.95$ are observed at 136 Hz.

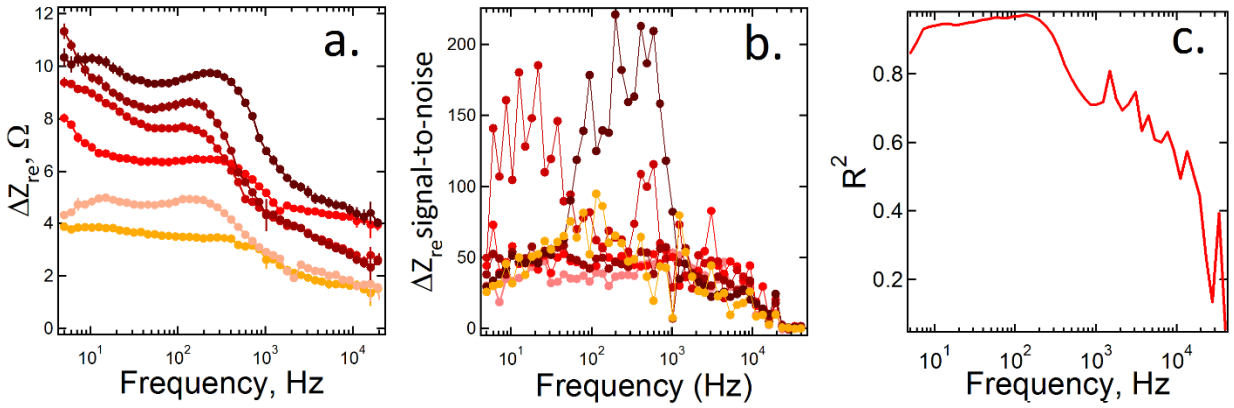

Figure A.5.. (a) Calibration plot of ΔZ_{re} versus frequency for virus-PEDOT films in varying concentrations of HSA in synthetic urine. Each HSA concentration was measured using a different biosensor. Errors bars are defined as the standard deviation, ±1σ, of five consecutive impedance measurements on a single electrode. (b) S/N, defined as $\Delta Z_{re}/\sigma$, versus frequency for ΔZ_{re}. (c) At each frequency, ΔZ_{re} versus [HSA] was fitted to the Hill equation and the square of the regression coefficient, R^2, versus frequency plot. $R^2 = 1$ represents the best fit of the Hill equation to the data.

A.6. Phage Library Design and Selection of HSA Binders.

A.6.1 Phage Library Design

The HSA binding phage was selected from a mega random peptide library (MRPL) created by pooling 24, individually constructed, peptide libraries (Table A.2). Individual peptide libraries contain five to 18 amino acids codons encoding the 20 naturally occurring amino acids or none or two cysteines. Each library has a theoretical peptide diversity of 10^6 to 10^{23}, respectively. Among the library members, X_8 is the only designed linear library, and the other libraries are structurally constrained by disulfide bonds. The library of peptides is fused to the N-terminus of P8, which is localized in the oxidizing environment of the periplasm prior to assembly in the phage[1, 2].

Table A.2. The MRPL components representing theoretical and actual peptide diversity.

Library Design	Number of Residues	Theoretical Peptide Diversity	Actual Peptide Diversity
CX_5C	7	3.2×10^6	1.7×10^8
CX_5CX	8	6.4×10^7	1.2×10^8
$X_2CX_2CX_2$	8	6.4×10^7	2.0×10^8
X_8	8	2.6×10^{10}	2.3×10^8
XCX_5C	8	6.4×10^7	1.8×10^8
CX_5CX_2	9	1.3×10^9	1.0×10^8
$X_2CX_2CX_3$	9	1.3×10^9	2.0×10^8
$X_2CX_3CX_2$	9	1.3×10^9	3.2×10^8
X_2CX_5C	9	1.3×10^9	4.7×10^8
$X_2CX_4CX_2$	10	2.6×10^{10}	2.5×10^8
$X_2CX_5CX_2$	11	5.1×10^{11}	3.2×10^8
$X_2CX_6CX_2$	12	1.0×10^{13}	2.7×10^8
$X_2CX_7CX_2$	13	2.0×10^{14}	3.3×10^8
$X_2CX_8CX_2$	14	4.1×10^{15}	2.5×10^8
$X_2CX_9CX_2$	15	8.2×10^{16}	3.3×10^8
$X_2CX_{10}CX_2$	16	1.6×10^{18}	3.8×10^8
$X_4CX_2GPX_4CX_4$	18	1.6×10^{18}	1.2×10^8
$X_4CX_{10}CX_4$	20	2.6×10^{23}	6.0×10^7

$X_5CX_8CX_5$	20	2.6 X 10^{23}	1.2 X 10^8
$X_5CX_9CX_4$	20	2.6 X 10^{23}	1.0 X 10^8
$X_6CX_6CX_6$	20	2.6 X 10^{23}	1.2 X 10^8
$X_6CX_7CX_5$	20	2.6 X 10^{23}	2.5 X 10^8
$X_7CX_4CX_7$	20	2.6 X 10^{23}	1.2 X 10^8
$X_7CX_5CX_6$	20	2.6 X 10^{23}	1.1 X 10^8

A highly efficient site-directed mutagenesis method, Kunkel mutagenesis was used to clone libraries in the phagemid.[3] The pooled libraries were electroporated, into SS320 cells, a strain of *E. coli* optimized for efficient electroporation.[4] The P8 phagemid, carries an antibiotic resistance marker, bacterial and phage origins of replication, and a phage packaging signal. Virions extruded from co-infected cells contain single-stranded recombinant phagemid DNA, and display a mixture of recombinant and wild-type P8 proteins.[5] Phage-displayed peptides have a physical linkage between phenotype (the expressed peptide) and its encoding phagemid DNA. This linkage provides easy access to the DNA sequence of any MRPL phage-displayed peptide that binds a target of interest.

The cells were grown in 2YT media supplemented with carbenicilin (50 μg/ml) and tetracyclin (5 μg/ml), and infected with KO7 helper phage (10^{10} phage/mL) before growth in 2YT/carbenicilin media supplemented with kanamycin (20 μg/ml). The culture was shaken at 250 rpm for 16-18 h at 37 °C. To isolate the phage from the cells, the culture was centrifuged for 10 min at 10 krpm at 4 °C. The supernatant was decanted into separate tubes, and the phage was precipitated by addition of 1/5th volume of PEG-NaCl (2.5 M NaCl, 20% PEG-8000). The solution was placed on ice for 1 h. Next, the phage was recovered by centrifugation for 10 min at 10 krpm. The phage pellet was resuspended in phosphate-buffered saline (PBS, 140 mM NaCl, 2.7 mM KCl, 10 mM Na_2HPO4, 2 mM KH_2PO_4, pH 7.2) with addition of 0.05% Tween-20. After additional centrifugation for 10 min at 15 krpm, the phage precipitation step was repeated as

described above. Phage were isolated by PEG-NaCl precipitation, and their concentration was determined by UV absorbance at 268 nm.

A.6.2 Selection of HSA Binders

In each of five rounds of selection, 15 wells of a 96-well microtiter plate (Nunc) were coated with 10 μg/mL HSA in 100 μL of PBS (pH 8.0), and incubated overnight at 4 °C on a shaker. After removal of the coating solution, 400 μL of a solution of 0.2% w/v casein in PBS was used to block the wells for 30 min on a shaker at room temperature. In successive rounds, the blocking reagent was switched to BSA, ovalbumin, or nonfat milk (NFM). The plate was then washed three times with 300 μL per well 0.05% Tween-20 in PBS. Phage were added to the wells in a buffer containing 0.2% w/v BSA, 0.05% Tween-20 in PBS. After 90 min incubation on a shaker at room temperature, the wells were washed with 0.05% Tween-20 in PBS. The numbers of washes increased with each round from 3, 5, 5, 7, and 9 times respectively for the five rounds. The bound phage was eluted by adding 100 μL of 0.1 M HCl and shaking vigorously at room temperature for 5 min. The phage were neutralized with 33 μL of 1 M Tris-HCl, pH 8.0. Before incubation for 45 min at 37 °C, 2 mL of the eluted phage was used to infect 20 mL of log phase *E. coli* XL-1 Blue cells. Helper phage KO7 was added at $\approx 6X10^{12}$ phage/mL, and after 45 min of incubation, the culture was transferred to 200 mL of 2YT supplemented with 50 μg/mL carbenicillin and 20 μg/mL kanamycin and shaken overnight at 37 °C for 16-18 h.

After 5 rounds of selection, spot assays were performed on around 200 selectants targeting HSA (10 μg/mL). The assay was performed based on a sandwich ELISA format in 96-well microtiter plates. Four potential HSA binders were obtained from the selections and spot assay. The four peptides were further examined for specificity to HSA. In the specificity assay, the

selectants were screened against seven different proteins including kinases, membrane proteins, and high pI proteins. Furthermore, to increase accuracy, the binders were also screened against *E. coli* and mammalian cancer (fibroblasts, kidney, and prostate) cell lysates. From the selected variants, only two binders demonstrated high affinity and specificity to the HSA protein.

The apparent K_d of both binders was calculated by dose–dependent ELISA. The phagemid containing the genes encoding P8 fused to either peptide 1 or 2 were transformed in $CaCl_2$ competent *E. coli* XL-1 Blue cells. Similar steps were followed for the phage growth and precipitation as mentioned in the previous section. The phage concentration was determined by UV absorbance at 268 nm. For the ELISA, 96-well microtiter plates (Nunc) were coated with 10 μg/mL of HSA in PBS (pH 8.0), and incubated on a shaker at 4 °C overnight. The wells were blocked with 0.2% w/v solution of BSA in PBS at room temperature on a shaker for 30 min and washed three times with wash buffer (0.05% v/v Tween-20 in PBS). The phage were then serially diluted along with a negative control (Stop4 phage) in phage dilution buffer (0.2% w/v BSA, 0.05% v/v Tween-20 in PBS). The plates were incubated with the samples at room temperature on a shaker for 1 h and then washed five times with wash buffer. Anti-M13/HRP conjugate (GE Healthcare) was diluted 1:5000 in the phage dilution buffer, added to the wells, and incubated for 30 min on a shaker at room temperature. The wells were washed four times with wash buffer and once with PBS. 100 μL of a solution of 2 mg/mL o-phenylenediamine dihydrochloride, 0.02% w/v H_2O_2, in citric acid buffer (50 mM citric acid, 50 mM Na_2HPO_4, pH 5.0) was added to each well. After 10 min incubation, the absorbance at 450 nm was measured using a microtiter plate reader (Bio-Tek). The data was further analyzed by Prism (GraphPad) software, which estimated the apparent K_D for the binders. Since, the apparent K_D of binder 2 (0.08 nM) was higher than binder 1 (45 nM), future experiments were conducted with binder 2. For incorporation of phage

in the virus-PEDOT films, the phage pellet obtained after the above protocol was re-suspended in aqueous $LiClO_4$ (12 mM) solution.

The mega random peptide library (MRPL) from which HAS binders were selected was constructed from 24 individual peptide libraries. Each library was designed to be structured, yet as unbiased as possible, and thus provide potential binders for a wide range different targets. The individual libraries were designed to be structurally different using degenerate codons and varied placement of cysteine-based disulfide bonds. Each amino acid residue in the peptide was randomly assigned using NNS as the codon designation; where N is any nucleotide, and S is C or G. Thus, each degenerate position is designed to encode all 20 natural amino acids, termed "hard randomization." The codon choice prevents the occurrence of the non-suppressible stop codons TGA and TAA that could result in non-displayed peptides. Due to the degeneracy of the genetic code, some amino acids will be represented twice (A, G, P, T and V; in one-letter amino acid code) or three times (R, L and S). In addition, a TAG stop codon in each position could be encoded. In an amber suppressor strain of *E. coli* such as XL1 Blue used here, the TAG will be read as mixture of glutamine and a stop codon minimizing the impact of terminating translation to <50%.

The constrained libraries have random residues flanked by cysteines, which spontaneously form disulfide bonds creating constrained loops of two to ten amino acids. In addition, the libraries are constructed to limit the number of possible loop conformations to improve the overall free energy of binding compared with the unconstrained library. The design can increase binding affinity by limiting the entropic cost upon peptide binding to the target. Also, the X_8 linear library is included to provide conformations missing from the constrained libraries. Therefore, engineering and using multiple primary libraries with unconstrained and constrained peptides forming large or small loops, MRPL has the diversity to yield productive results when applied to

selections against a variety of targets. The theoretical diversity of the MRPL far exceeds the capability of any known system to accommodate full expression and maintenance of 10^{24} individual library members.

The twenty-four libraries were mixed and subjected to thermodynamic or equilibrium-based selections for binding to HSA. The target protein, human serum albumin (HSA) was purchased from Sigma Aldrich as lyophilized powder, and was dissolved in PBS (pH 8.0) for rounds of selection. After bio panning targeted to HSA, a total of 200 selectants were screened from the different rounds of selections. Furthermore, the binders were tested for specificity to HSA against various proteins aurora kinase A (AKA), bovine serum albumin (BSA), non-fat milk, ovalbumin, hen egg white lysozyme (HEWL), and cav(1-104)[6] by phage-based ELISA. To increase stringency for specificity, cell lysates of *E. coli* and human cancerous cell lines (LnCAP, 3T3, 293T, and PC3) were also included in the specificity assay.

Table A.3. Sequence of the binders selected after affinity maturation and specificity assay.

Binder	1	2	3	4	5	6	7	8	9	10	11	12	13	14	15	16	17	18	19	20
1	Q	Y	G	E	A	C	W	D	G	Y	S	W	K	N	C	L	A	L	T	L
2	D	C	P	I	Y	C	E	D	G	Y	C	L	R	K	C	V	D	L	Y	R

Two binders of 20 residues each were selected with high affinity and specificity to HSA (Table S3). Binder 1 and 2 emerged from round 5, with binder 2 being cysteine rich. Binder 2 had four cysteines, compared to binder 1, which had two cysteines (Table S3). This probably suggest that intramolecular disulfide bond formation within the peptide might have advantage in binding HSA to acquire binding energy. The apparent K_D of both the binders through phage-based ELISA was calculated in sub-nanomolar range. Binder 2, which exhibited the strongest relative affinity and specificity to HSA in the ELISA, was chosen for further bio-sensing studies.

A.6.3 References

1. Dottavio D: CHAPTER 7 - Phagemid-Displayed Peptide Libraries. In: *Phage Display of Peptides and Proteins.* Burlington: Academic Press; 1996: 113-125.
2. du Plessis DH, Jordaan F: CHAPTER 9 - Phage Libraries Displaying Random Peptides Derived from a Target Sequence. In: *Phage Display of Peptides and Proteins.* Burlington: Academic Press; 1996: 141-150.
3. Kunkel TA, Roberts JD, Zakour RA: Rapid and Efficient Site-Specific Mutagenesis without Phenotypic Selection. *Methods in Enzymology* 1987; 154: 367-382.
4. Sidhu SS, Lowman HB, Cunningham BC, Wells JA: Phage display for selection of novel binding peptides. *Method Enzymol* 2000; 328: 333-363.
5. Smith GP: Filamentous Fusion Phage - Novel Expression Vectors That Display Cloned Antigens on the Virion Surface. *Science* 1985; 228: 1315-1317.
6. Majumdar S, Hajduczki A, Vithayathil R, Olsen TJ, Spitler RM, Mendez AS, Thompson TD, Weiss GA: In vitro evolution of ligands to the membrane protein caveolin. *Journal of the American Chemical Society* 2011; 133: 9855-9862.

Chapter 3

The Virus BioResistor: Wiring Virus Particles for the Direct, Label-Free Detection of Target Proteins

This chapter was adapted from a research article (Bhasin, A; Ogata, Alana F; Briggs, Jeffrey S; Tam, PY; Tam, Ming X; Weiss, Gregory A; Penner, Reginald M. *Nano Letters*. **2018**, 18 (6), 3623-3629)

3.1 Introduction

Investigating the electrical properties of microscopic biological entities such as organelles, bacteria, eukaryotic cells, and viruses is both interesting from a fundamental science perspective, as well as challenging because they are electrically insulating. How does one "wire" such structures to an external circuit?[1,2,3] Elegant solutions to this problem have been demonstrated involving interfaces to single cells, bacteria etc. involving single nanostructures or ensembles of nanostructures (nanowires, nanotubes, nanosheets, etc.). For example, electrical signals from single cells have been measured using graphene field-effect transistors, and nanowire-embedded n-p junctions.[4,5] The "wiring" of bacteria to electrode surfaces has been accomplished using outer sphere redox mediators.[6,7,8]

A new approach, the *virus bioresistor* (or *VBR*), provides the means for incorporating virus particles into an electrical circuit (Figure 3.1). The key to the *VBR* is an electronically conductive channel composed of poly(3,4-ethylenedioxythiophene) or PEDOT into which M13 virus particles are embedded (Figure 3.1a). Individual M13 virus particles are filamentous with dimensions of 6 nm (w) x 1.0 μm (l). The recognition and binding of target molecules to thousands of M13 virus particles embedded in this polymeric channel is signaled by an electrical impedance signature, which can be measured by an external circuit (Figure 3.1b,c). The impedance response of the *VBR* is modeled by a simple equivalent circuit containing just three circuit elements: A solution resistance (R_{soln}), a channel resistance (R_{VBR}), and an interfacial capacitance (C_{VBR}) (Table 3.1). Information on target binding is contained in the R_{VBR}, which can be measured either at a single frequency or from the best fit of the Nyquist plot across 40 or 50 discrete frequencies using this equivalent circuit.

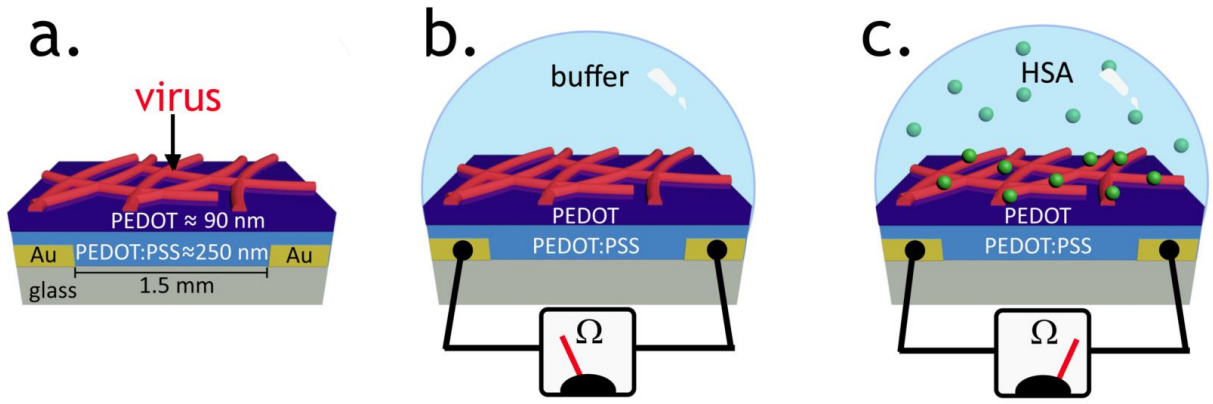

Figure 3.1. The *Virus BioResistor* (*VBR*). a) Schematic diagram of a *VBR* showing critical components and dimensions. b) A buffered salt solution alters the solution resistance, R_{soln}, but not the resistance of the *VBR* channel, R_{VBR}. C) In the presence of a target protein (HSA in this case), R_{VBR} is increased, enabling determination of its concentration.

We demonstrate the *VBR* concept using a model system in which human serum albumin (HSA, 66 kDa), is detected in a phosphate buffer solution. The *VBR*s described here have a baseline dc resistance of 200-250 Ω which is the same in air or in an aqueous buffer solution, and are capable of producing large signals ($\Delta R_{VBR} \approx 250$ Ω, or $\Delta R_{VBR}/R_o \approx 100\%$) for the detection of HSA in phosphate buffer solutions across the entire HSA binding curve ranging from [HSA] = 7.5 to 900 nM. In spite of the fact that the electrical signal generated by *VBR*s derives purely from ensembles of biological entities, extremely high sensor-to-sensor reproducibility of this signal is attainable for the response of *VBR* biosensors culminating in a coefficient-of-variation of the measured [HSA] for 20 sensors less than 15% across the entire HSA binding curve. The *VBR* achieves these metrics using a two-terminal, monolithic device architecture that is simple, robust, manufacturable, and inexpensive. No reagents and no sandwich amplification of the impedance signal are required, and no redox species are added to the test solution. Collectively, these data demonstrate the feasibility of adapting the *VBR* concept to rapid, inexpensive urine and blood-based assays at the point-of-care.

3.2 Experimental Considerations

3.2.1 Materials

Devices were designed and manufactured by the Penner lab. Devices and cells (Wainamics Inc., Fremont CA) were cleaned by O_2 plasma using a plasma cleaner (PDC-32G, Harrick Plasma) All chemicals were purchased from Sigma Aldrich and used as received, unless noted. Buffer solutions contained phosphate-buffered saline (PBS, 137 mM NaCl, 2.7 mM KCl, 10 mM Na_2HPO_4, 1.8 mM KH_2PO_4 pH 8) filtered through a 0.22 µM pore size membrane (Corning) and 2 mg/mL of Casein. Human serum albumin (Human Albumin fraction V; low folate, B12; MP Biomedicals; purity > 97%) were analyzed by SDS-PAGE and used as received. Bovine serum albumin (BSA, Calbiochem Omnipur) was used as received. EDOT was purified by silica flash chromatography.

3.2.2 Phage Library Design and the Selection of HSA Binders

The procedures associated with design of the phage library, selection of HSA binders from this library, and screens to isolate the HSA-binding virus were described previously.[17]

3.2.3 VBR Fabrication

The fabrication process for one pair (2) of *VBR*s involved the following four steps (Figure 3.2). First, two pairs of gold-electrodes are prepared by photolithography. These gold electrodes have width of 2 mm and their separation of 1.5 mm defines the *VBR* channel length. Gold electrode pairs are separated laterally by 0.5 mm. Second, a layer of PEDOT:PSS is spin-coated onto the gold-electrode device and baked for 1 hr at 90˚C. Third, a 2 mm x 2 mm PMMA cell is attached defining the area of the *VBR* bioaffinity layer. Fourth and finally, a virus-PEDOT top layer is

electropolymerized on top of the PEDOT-PSS bottom layer by using ≈100 μL of plating solution and applying two oxidizing voltammetric scans. The virus-PEDOT plating solution is removed and the cell is rinsed. Electrodes are used to enable impedance measurements at each of the two VBR sensors. One background impedance measurement is acquired in buffer, and a second in a solution containing added HSA. The difference between these two measurements, calculated at each frequency, is ΔR_{VBR}.

Further details relating to this process are the following: Gold-film electrodes were cleaned by O_2 plasma for 10 min immediately before use. Scotch tape was placed on the ends of the electrodes to protect the contacts. A poly(3,4-ethylenedioxythiophene)-poly(styrenesulfonate) (PEDOT:PSS,1.0 wt.% in H_2O, high conductivity grade) layer was deposited on the electrodes by spin-coating (2500 rpm, 80s) and baked for 1 hr at 90˚ C. Electrodes were then allowed to come to room temperature and the cell was then mounted on the gold-film electrodes followed by the incubation of the electrodes in PBS for 90 min. Next, virus-PEDOT films were electropolymerized onto the PEDOT:PSS/gold-film electrodes using a platinum foil counter and a mercurous sulfate electrode (MSE). Virus-PEDOT films were prepared by cycling between 0.2 V and 0.8 V at a scan rate of 20 mV/s in plating solution using a PARSTAT 2263 controlled by Electrochemistry PowerSuit 2.6 software. Plating solutions contained 8 nM M13 bacteriophage, 12.5 mM $LiClO_4$, 2.5 mM EDOT and electropolymerized for 2 cycles.

*VBR*s were evaluated at every step of the fabrication process to ensure the reproducibility of signal for a particular HSA concentration. Starting with the fabrication by photolithography of gold electrodes, the *VBR* is prepared in four steps (Figure S1). The parameters measured at each of these steps is indicated in the diagram for Fig. S1. In this diagram, the following definitions apply: $\boldsymbol{R_{au}}$ is the dc resistance of the gold electrons prepared in step 1, measured along their longest

dimension, R_{trans} is the dc resistance of the PEDOT-PSS film produced in step 2, i_p is the peak current for the electropolymerization, by cyclic voltammetry, of the virus-PEDOT composite in step 3, $Z_{im,m}$ and $Z_{re,m}$ are the baseline impedances measured for the complete *VBR* measured in 160 mM PBS buffer solution. *VBR* device yield using these process windows was ≈30%.

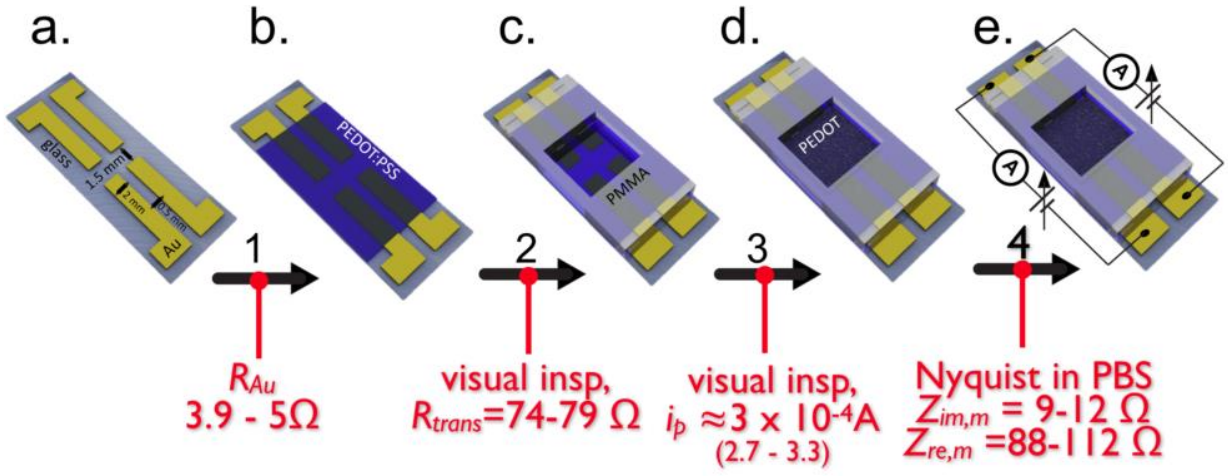

Figure 3.2 – Process flow for the four-step *VBR* fabrication process, including the process windows that were enforced for this process, indicated in red.

3.2.4 Impedance Spectroscopy (IS)

All buffer solutions were prepared and brought to room temperature (74°F) prior to EIS measurements. Newly plated phage-PEDOT chemiresistor films were washed three times with PBS and subsequently incubated in PBS for 10 minutes. All EIS measurements were taken with the PBS solution as the run buffer. Three consecutive IS measurements were taken using a PARSTAT 2263 controlled by Electrochemistry PowerSuit 2.6 software. 50 data points were acquired across a frequency range of 5 Hz to 40 kHz. The amplitude of the applied voltage was 10 mV for all EIS measurements. Chemiresistor films were then incubated in HSA solutions in run buffer for 10 min followed by three consecutive IS measurements. Independent electrodes were

used for measurements of a single concentration of HSA solutions and BSA solutions. Equivalent circuit fitting was acquired using the EIS Analyzer software (ABC Chemistry).

3.2.5 AFM and SEM Analysis

Scanning electron microscopy (SEM) were acquired on uncoated films at 2 keV using a FEI Magellan 400L XHR system. Atomic force microscopy (AFM) was performed on chemiresistor films using an Asylum MFP-3D-SA atomic force microscopy (Asylum Research, Santa Barbara, CA) equipped with Olympus AC160TSAFM tips (Olympus) in laboratory ambient air. AC Mode AFM images were acquired at 512 x 512 pixels spanning a 20 μm range. The Asylum image processing software was used to analyze AFM images and amplitude traces.

3.3 Results and Discussion

The fabrication of a *VBR* involves the preparation of two gold electrical contacts on a glass substrate by photolithography (Figure 3.3). On top of these contacts, a two-layer *VBR* channel (15 mm (l) x 20 mm (w)) is prepared consisting of a spin-cast PEDOT-PSS semiconductor bottom layer (200-300 nm in thickness) and an electrodeposited virus-PEDOT composite top layer containing thousands of engineered M13 virus particles[9,10,11] (90 – 100 nm in thickness). This virus-PEDOT electrodeposition process involves the application of two oxidizing voltammetric scans to an aqueous solution containing 8 nM M13 virus particles in 12.5 mM $LiClO_4$, 2.5 mM EDOT (Figure 3.4a).

If the PEDOT-PSS/PEDOT-virus layer that electrically connects the two metal electrodes is severed, forcing current traveling between these two electrodes into the solution phase, we recently demonstrated that the resulting device still functions as a biosensor.[20] But the *VBR* has

three attributes not found in this device: 1). An impedance signal that is amplified by a factor of 20 (200 Ω here *versus* 12 Ω in our prior work.[20] The result is a limit-of-detection of 7.5 nM in the VBR versus 100 nM in the earlier device,[20] 2) The ability to decouple this signal from the salt concentration of the solution (*vide infra*), and, 3) A dramatically faster response time of ≈5 s here *versus* 8-10 min.[20]

A cross-sectional SEM image of a *VBR* biosensor film shows a virus-PEDOT top layer with a thickness of ~92 nm on top of a ~245 nm PEDOT:PSS bottom layer (Figure 3.4b). Plain-view SEMs of pure PEDOT films prepared in an aqueous plating solution of 2.5 mM EDOT and 12.5 mM $LiClO_4$ show a smooth, homogenous surface (Figure 3.4c). Virus-PEDOT films prepared from the same plating solution with the addition of 8 nM virus show dark, filamentous structures within the virus-PEDOT top layer (Figure 3.4d). These filaments are M13 bacteriophage, which have typical dimensions of 6 nm (diameter) x 1.0 μm (length). Atomic force microscopy (AFM)

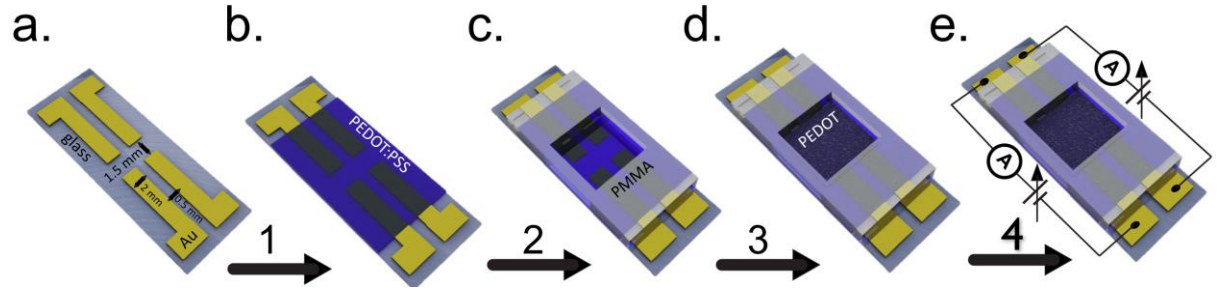

Figure 3.3. *VBR* biosensor fabrication. a) Two pairs of gold-electrodes from which two VBRs are prepared. The gold electrodes have width of 2 mm and their separation of 1.5 mm defines the channel length of these devices. The two pairs of gold electrodes are separated by 0.5 mm. b) A layer of PEDOT:PSS is spin-coated onto the gold-electrode device and baked for 1 h at 90 °C. c) A 2 mm x 2 mm PMMA cell is attached defining the area of the bioaffinity layer. d) A virus-PEDOT top layer is electropolymerized on top of the PEDOT-PSS bottom layer by using ≈100 μL of plating solution and applying two oxidizing voltammetric scans. e) The virus-PEDOT plating solution is removed, and the cell is rinsed. Electrodes are used to enable impedance measurements at each of the two *VBR* sensors. One background impedance measurement is acquired in buffer, and a second in a solution containing added HSA. The calculated ΔR_{VBR} is used to determine the HSA concentration in this sample with reference to a calibration curve.

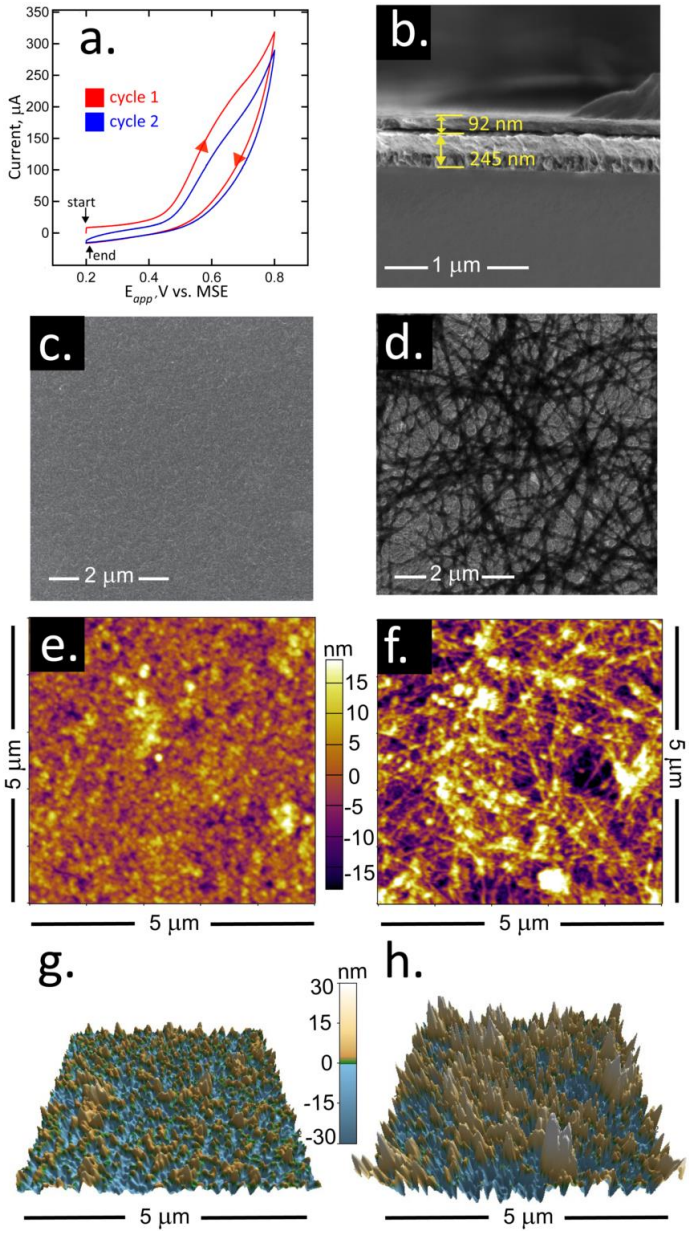

Figure 3.4. Electrodeposition and SEM/AFM characterization of virus-PEDOT bioaffinity layers. (a) Electrodeposition of a virus-PEDOT film on a PEDOT-PSS film using cyclic voltammetry (50 mV/s). The virus-PEDOT top layer is prepared by two cycles from an aqueous virus-EDOT solution containing 2.5 mM EDOT, 12.5 mM $LiClO_4$, and 8 nM HSA phage. (b) cross sectional scanning electron microscopy (SEM) image of a PEDOT-PSS/virus-PEDOT film. The PEDOT-PSS bottom layer and virus-PEDOT top layer can be distinguished. (c) Plan view SEM image of a PEDOT only film (no virus) prepared by two consecutive cycles of deposition in aqueous EDOT solution containing 2.5 mM EDOT, 12.5 mM $LiClO_4$. (d) Plan view SEM image of a virus-PEDOT film prepared as described in (a). (e,f,g,h) Atomic force microscopy (AFM) images of PEDOT films (e,g) and virus-PEDOT films (f,h). The same AFM image data are represented in two ways: (e,f) shows height versus position data while (g,h) show a three-dimensional rendering of these the same data shown in (e,f). The rms roughness for PEDOT and virus-PEDOT films are ≈5 nm and ≈10 nm, respectively.

RMS surface roughness of 5 nm (Figure 3.4e,g). If this layer is produced to contain virus particles, a slightly rougher surface is seen with an RMS roughness of 10 nm; however, a distinct topography reveals the presence of fiber like structures that can be attributed to PEDOT-covered virus strands protruding from the PEDOT surface (Figure 3.4f,h). After the virus-PEDOT top layer is electrodeposited, the bioaffinity layer is complete, and the *VBR* is ready to use.

We elected to monitor VBRs using an *ac* impedance measurement, rather than applying a simpler *dc* resistance measurement, because prior work on conductive polymer based chemiresistors have shown conclusively that dramatically lower noise can be accessed using *ac* detection, even at frequencies as low as 5 Hz.[12,13,14] Analytical equations for the real and imaginary components of the complex impedance, Z_{re} and Z_{im} (Table 3.1), are used to fit experimental impedance data to extract the values of the three circuit elements: R_{soln}, R_{VBR}, and C_{VBR}. A version of the equivalent circuit in which a constant phase element (CPE) is substituted for each capacitor is used for this purpose. This elaboration provides better agreement between the calculated and the experimental impedance data, resulting in improved precision for the measurement of R_{VBR} (Table 3.1). The impedance of a CPE, Z_{CPE}, and the capacitive impedance, Z_C, are defined by these equations:

$$Z_C = \frac{1}{i\,\omega\,C} \qquad Z_{CPE} = \frac{1}{i\,\omega\,Q^n}$$

where ω is the angular frequency (s^{-1}), $i = \sqrt{(-1)}$. Q^n is the CPE capacitance (F) where n has a value of 1.0 if the CPE is purely capacitive. n is used as a fitting parameter in this study and has a value of $1.0 < n < 1.2$.

Table 3.1. Equivalent circuits and equations representing the electrical response of a *VBR* biosensor.

Eq. Circuit[a]	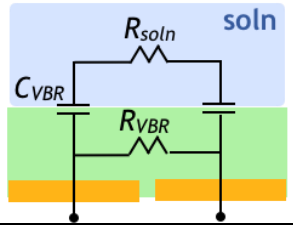
Z_{re} =	$\dfrac{R_{VBR}R_{soln}\,(R_{VBR}+R_{soln}\,)+\dfrac{R_{VBR}}{\omega^2 {C_{VBR}}^2}}{(R_{VBR}+R_{soln}\,)^2+\dfrac{1}{\omega C_{VBR}}^2}$
Z_{im}=	$\dfrac{\dfrac{{R_{VBR}}^2}{\omega C_{VBR}}}{(R_{VBR}+R_{soln}\,)^2+\dfrac{1}{\omega C_{VBR}}^2}$
Eq. Circuit[b]	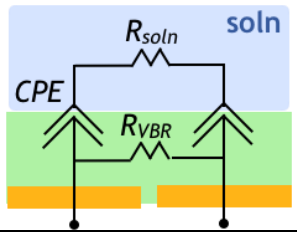
Z_{re}=	$\dfrac{R_{VBR}[\,1+Q_{VBR}\omega^n(2R_{VBR}+R_{soln})\cos\frac{\pi n}{2}+\,R_{soln}{Q_{VBR}}^2\omega^{2n}(R_{soln}+R_{VBR})]}{Q_{VBR}\omega^n(R_{soln}+R_{VBR})\left[(R_{soln}+R_{VBR})Q_{VBR}\omega^n+2\cos\frac{\pi n}{2}\right]+1}$
Z_{im}=	$\dfrac{-\,R_{VBR}^2\,\omega^n\,Q_{VBR}\,\sin\frac{\pi n}{2}}{Q_{VBR}\omega^n(R_{soln}+R_{VBR})\left[(R_{soln}+R_{VBR})Q_{VBR}\omega^n+2\cos\frac{\pi n}{2}\right]+1}$

[a]Capacitive equivalent circuit, [b]Equivalent circuit with constant phase elements (CPEs).

The *VBR* produces a distinctive impedance response consisting of a semicircular Nyquist plot (Z_{im} *versus* Z_{re} as a function of frequency) (Figure 3.5a-c). This response resembles the Randles equivalent circuit that is commonly seen for electrochemical biosensors operating in the presence of an added redox species, such as $Fe(CN)_6^{3-/4-}$.[15,16] The semicircular Nyquist plot for electro-chemical biosensors derives from electron transfer to and from the redox species present in the solution. When a redox species is not added, no semicircle is observed. The *VBR* produces a semicircular Nyquist plot *without added redox species*. Instead, the *VBR* channel presents a

parallel resistance – dominated by electron conduction through the polymer composite *VBR* - and capacitance – produced by the non-Faradaic charging and discharging of the electrical double layer at the surface of the *VBR*. The semicircular Nyquist plots aids in the precision with which R_{VBR} can be measured – just as it does in electrochemical biosensors that use the diameter of this semicircle – the so-called charge transfer resistance – to transduce target binding.[17,18,19]

VBR biosensors are able to distinguish between changes in the electrical resistance of the test solution, caused by variations in the salt concentration for example, and the concentration of target molecules present in this solution. Information on the electrical conductivity of the solution is contained in R_{soln} whereas the concentration of target protein is encoded by R_{VBR}. Virtually no cross-talk occurs between these two circuit elements. For example, Nyquist plots (Z_{im} *versus* Z_{re} as a function of frequency) for a *VBR* in three concentrations of PBS buffer (1x PBS, 2.5x PBS and 5x PBS) show the same $\Delta R_{VBR} = R_{VBR,HSA} - R_{VBR,buffer}$ signal for 75 nM HSA (Figure 4e) independent of the salt concentration ([NaCl]) over the range of 134 to 670 mM. Notably, R_{soln} decreases dramatically with increasing salt concentration (Figure 3.5d).

The complementary experiment is to vary [HSA] in a 1x PBS buffer solution (Figure 3.5f). Here, Nyquist plots are shown for five buffer solutions containing [HSA] = 0 nM, 70 nM, 220 nM, 370 nM, and 750 nM. In this case, a quasi-linear increase in ΔR_{VBR} with [HSA] is measured (Figure 4h), and R_{soln} remains constant (Figure 3.5g). This property of *VBR*s – the ability to parse changes in impedance due to the solution resistance and target binding – provides an enormous advantage in terms of the application of this biosensor technology to body fluids where salt concentrations are unknown and uncontrolled.

VBR performance was evaluated for the detection of HSA using 20 *VBR*s in order to assess sensor-to-sensor reproducibility and coefficient-of-variance (CoV) to determine their practicality

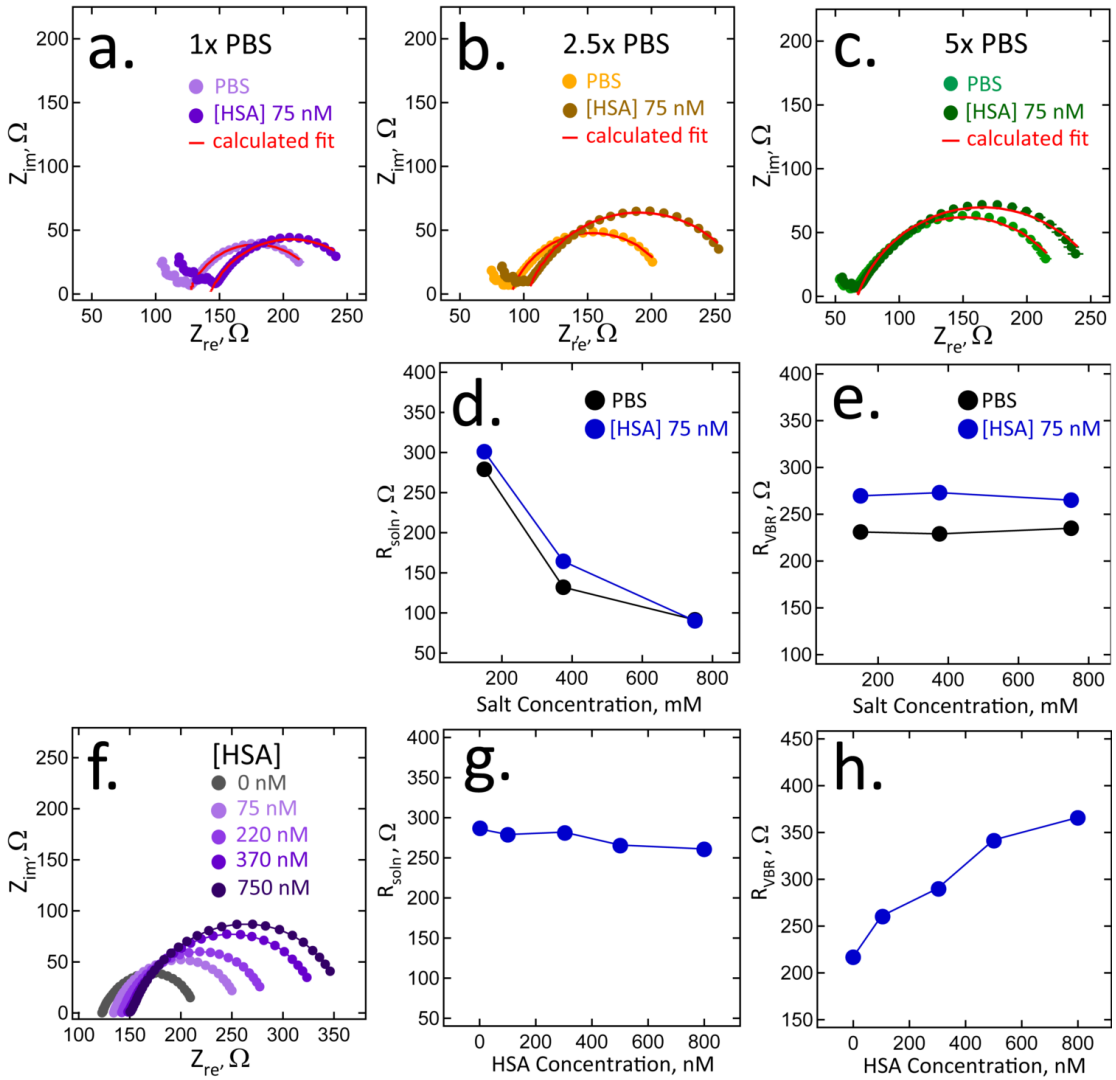

Figure 3.5. Orthogonal measurement of R_{soln} and R_{VBR} using a *VBR* biosensor. Nyquist plots summarizing the impedance response of *VBR*s from 1 Hz to 10 kHz with equivalent circuit fits (red traces). (a,b,c) *VBR*s in solutions of run buffer of: a). 1x PBS (purple), b). 2.5x PBS (yellow), c). 5x PBS (green), before and after exposure to 75 nM HSA in the same buffer. (d,e). Plots of R_{soln} and R_{VBR} as a function of buffer concentration extracted from the data of a,b, and c. Shown are the values of these two circuit elements in pure buffer, and in buffer with added 75 nM HSA, as indicated. (f,g,h) Experiment in which the HSA concentration is increased from 0 nM (1x PBS) to 750 nM (in 1x PBS) showing the invariance of R_{soln} and the linear increase in R_{VBR}.

for single use biosensors. Two methods for analyzing *VBR* impedance data are also assessed here. The first method was previously used for non-faradaic impedance biosensors where the signal-to-noise guided the selection of a single frequency at which either ΔZ_{im} or ΔZ_{re} was calculated by, for example, $Z_{re,HSA} - Z^{o}_{re}$.[20] Using this approach, the sensing signal at 5 Hz was selected. The second method exploits a range of impedance data across 40-50 discrete frequencies and employs a fit to the equations of Table 3.1 to determine ΔR_{VBR}. Method 1 will afford more rapid analysis because impedance data at a single frequency is required. Method 2 requires longer analysis times; however, the approach has the potential to provide for higher precision and reduced noise for an assay, but can this advantage be demonstrated? To answer this question, the two methods were compared for three independent *VBR* biosensors (N = 3) at each HSA concentration from 7.5 nM to 750 nM to evaluate sensor-to-sensor reproducibility. In addition, two sensors (N=2) were tested at 900 nM [HSA].

The performance of Methods 1 and 2 are summarized in the plots of Figure 3.6a and b, respectively. The main conclusion is that there is little difference in the performance of these two methods in terms of sensitivity, precision, and noise. Both $\Delta Z_{re,\,5Hz}$ (Method 1) and ΔR_{VBR} (Method 2) track increases in the HSA concentration from 7.5 nM to 900 nM HSA, saturating at close to 900 nM. These two calibration plots are both fitted with the Hill equation, which is frequently used to model biosensor response:[21]

$$\Delta \mathrm{Z}_{re} = \Delta \mathrm{Z}_{re,lim} + \frac{\Delta \mathrm{Z}_{re,0} - \Delta \mathrm{Z}_{re,lim}}{1 + \left(\frac{C_{HSA}}{K_D}\right)^{h}}$$

The best fit to the Hill equation for the ΔZ_{re} calibration plot results in $\Delta Z_{re,lim}$ = 250 ± 40 Ω, $\Delta Z_{re,0}$ = 16 ± 5 Ω, K_D = 480 ± 120 nM, h = 1.6 ± 0.3, and R^2 = 0.97. Fit to the Hill equation for the $\Delta R_{channel}$ calibration plot results in $\Delta R_{VBR,lim}$ = 250 ± 30 Ω, ΔR^o_{VBR} = 20 ± 5 Ω, K_D = 410 ± 60 nM, h = 1.9 ± 0.3, and R^2 = 0.98. These data provide no justification for the use of multiple analysis frequencies (Method 2) as compared with a single, S/N-selected, analysis frequency (Method 1). Apparent K_D values are identical within experimental error. Values of h, which indexes the degree

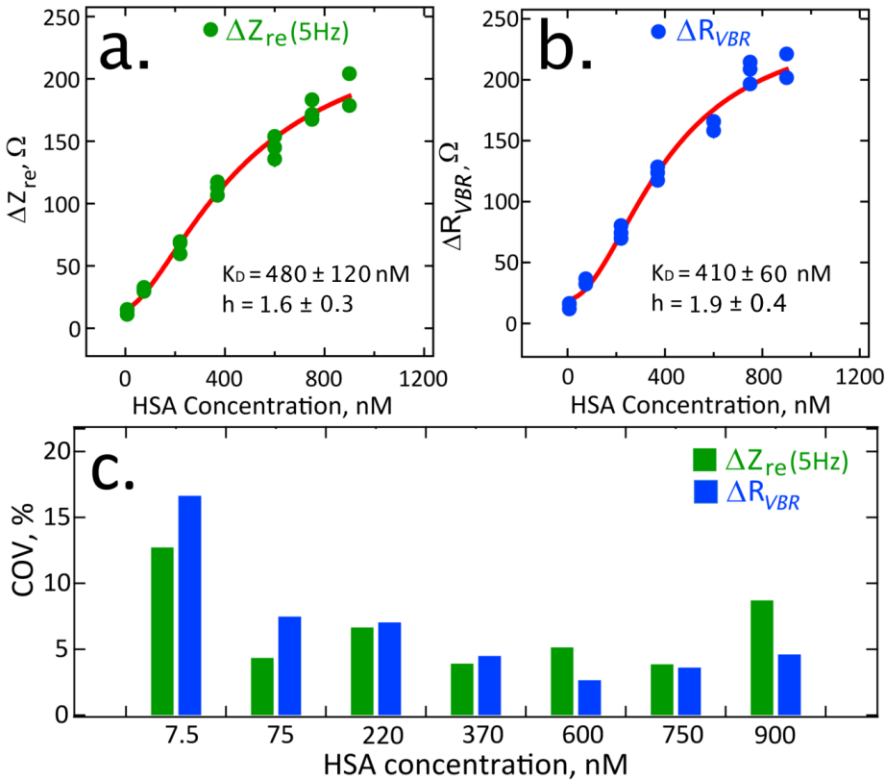

Figure 3.6. Calibration plots for 20 *VBR*s exposed to HSA concentrations 7.5 nM – 900 nM generated by two methods (5a) sensing signal ΔZ_{re}, measured at 5 Hz, versus concentration (5b) sensing signal defined as ΔR_{VBR}, versus concentration. At each of seven concentration points, three data point for three different VBR sensors are plotted here with error bars defined as the standard deviation, ±1σ. The exception is the 900 nM concentration point where just two sensors were used, and two data points are shown. It should be noted that these three data points are not all seen at all concentrations, since some are superimposed on others. Impedance data for HSA exposed to virus-PEDOT films containing HSA phage is fitted to the hill equation (red line). c) compares the CoV% for the signals from two methods obtained by the variation in signal generated by three devices exposed to concentrations [HSA] = 7.5 nM - 900 nM.

of cooperativity in target binding to virus particles, are also identical and equal to 1.6, which indicates significant cooperativity for phage binding to HSA in this system.

The origin of the *VBR* impedance signal is of interest, and remains the subject of investigation. Either of two signal transduction mechanisms could reasonably account for our observations: First, the PEDOT-PSS can function as a p-type organic semiconductor field effect transistor (FET).[22,23] In this case, an increase in ΔR_{VBR} with [HSA] is accounted for by the binding of a positively charged target molecule to the *VBR*, leading to depletion of majority carriers and an increase in impedance. But HSA has an isoelectric point, pI = 5.3,[24] and our PBS buffer has pH = 8.0., so the HSA in these experiments is expected to have an overall negative charge, not a positive charge, at this pH. The binding of HSA to the PEDOT *VBR* should therefore cause the accumulation of majority carriers, reducing its electrical impedance, which is contrary to our experimental observations. As demonstrated in Figure 4e, the signal amplitude observed for HSA is unaffected by increases in the salt concentration of the test solution from 1x PBS to 5x PBS. This observation suggests that an electric field effect is not involved in the signal transduction process, since the Debye length in these buffer solutions is both very small (2-8 Å) and variable.

A second, previously observed mechanism involves the disruption of long range ordering in the PEDOT-PSS polymer chains. For example, bulky intercalators such as tosylate anions can cause an increase in electrical resistance,[25] or "secondary dopants" – or by "secondary dopants" – including diethylene glycol,[17] olyethylene glycol,[16] and dimethyl sulfoxide[16] – that lubricate the motion of polymer chains thereby promoting a higher degree of long range ordering and a lower electrical resistance. HSA is readily classified as falling into the first category of bulky, structure disrupter. This description qualitatively explains the increases in resistance seen for *VBR*s upon exposure to HSA reported here. Furthermore, this model is consistent with the

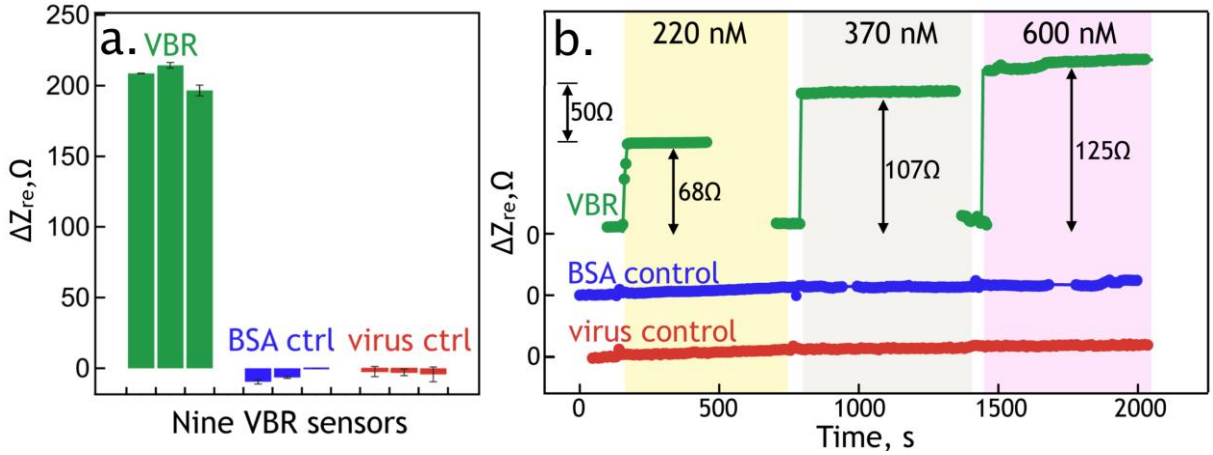

Figure 3.7. *VBR* specificity and speed. a). A specificity assay. Blue bars represent three *VBR*s with PEDOT films containing HSA binding phage exposed to 750 nM HSA; Red bars show the response to a 750 nM BSA solution of three *VBR*s containing HSA binding phage; Green bars show the response to a 750 nM HSA solution for three *VBR*s containing STOP4 phage that have no affinity for HSA. b). Real time *VBR* sensing data. Responses for three VBR sensors are shown for [HSA] exposures of 220, 370, and 600 nM that show response times of 30 s, 3 s, and 3 s, respectively. The specificity assay summarized in (a) are also repeated here, in real-time sensing format, again showing no measurable responses.

observed impedance signal for HSA measured at *VBR*s remaining unrelated to the salt concentration of the test solution. More work needs to be done with other analytes and solutions to cement our understanding of the *VBR* signal transduction mechanism.

In addition to sensitivity and reproducibility, selectivity and speed are the two other attributes important for biosensors. The selectivity of *VBR* biosensors was examined with two control conditions: 1) a *VBR* virus-PEDOT film containing HSA-binding virus measured for binding to 750 nM BSA protein, which is closely matched to HSA in terms of both size (both 66.5 kDa) and amino acid sequence (76% homologous)[26], and, 2) a *VBR* virus-PEDOT film containing the negative control STOP4 virus, which has no displayed peptide ligands, in the presence of 750 nM HSA protein. The sensing signal is described as $\Delta R_{VBR} = R_{VBR,HSA} - R_{VBR,PBS}$, determined by fitting the impedance data with the equivalent circuit of Table 3.1. Both control *VBR* biosensors

show less than ~1 Ω in of change (in either ΔR_{VBR} or ΔZ_{re}) in comparison to ~ 200 Ω resistance increase for HSA-virus-PEDOT films against 750 nM HSA. The impedance response for *VBR*s gives excellent binding signal specific to HSA at 200x over background (Figure 3.7a). Real-time *VBR* measurements (Figure 6b) allow the response time of these devices to be directly measured. We observe a rapid (3 – 30s) step-wise increase in ΔZ_{re} followed by near instantaneous settling of Z_{Re} at the concentration-appropriate value (Figure 3.7b). This constitutes a near ideal response function for a biosensor and demonstrates the potential utility of *VBR*s for point-of-care applications.

3.4 Summary

The *VBR* simplifies the problem of electrically communicating with virus particles, and importantly, extracting valuable information in this process. Communication takes the form of an increase in the electrical impedance of the virus-PEDOT *VBR* in the presence of a target protein disease marker, relative to the impedance measured in a pure buffer solution. This impedance increase of up to 200 Ω signals the degree to which virus-displayed peptides have recognized and bound a particular target protein, leading to precise and highly reproducible measurement of the concentration of this target molecule. The *VBR* is able to by-pass a ubiquitous noise source in electrical or electrochemical biosensing: the variable electrical impedance of the solution itself.

3.5 Acknowledgments

R.M.P. and A.F.O acknowledge support through the NSF Graduate Research Fellowships Program (GRFP) (Award DGE-1321846). In addition, the authors acknowledge support from the National Cancer Institute of the NIH (1R33CA206955-01), PhageTech Inc (PHAGE-

203015), and the Chao Family Comprehensive Cancer Center, UC Irvine. FE-SEM and TEM data were acquired using the instrumentation of the LEXI (lexi.eng.uci.edu/) and IMRI (ps.uci.edu/imri/) facilities at UCI. In addition, the assistance of Dr. Mark Richardson with EDOT purification is gratefully acknowledged.

3.6 References

(1) Simon, D.T.; Gabrielsson, E.O.; Tybrandt, K.; Berggren, M. *Chem. Rev.* **2016** *116*, 13009-13041.

(2) Lanzani, G. Nat. Mat. **2014** *13*, 775-776.

(3) Liao, C.; Zhang, M.; Yao, M.Y.; Hua, T.; Li, L.; Yan, F. *Adv. Mat.* **2015**, *27*, 7493-7527.

(4) Cohen-Karni, T.; Quan, Q.; Li, Q.; Fang, Y.; Lieber, C.M., *Nano Lett* **2010** 10, 1098-1102.

(5) Tzahi Cohen-Karni, T; Casanova, D.; Cahoon, J.F.; Qing, Q.; Bell, D.C.; Lieber, C.M., *NanoLett.* **2012** *12* 2639-2644.

(6) Pankratova, G.; Hasan, K.; Leech, D.; Hederstedt, L.; Gorton, L.; *Electrochem. Commun.***2017,** *75*, 56-59.

(7) Yuan, Y.; Shin, H.; Kang, C.; Kim, S. *Bioelectrochem* **2016**, 108, 8-12.

(8) Kaneko, M.; Ishikawa, M.; Hashimoto, K.; Nakanishi, S. *Bioelectrochem* **2017**, 114, 8-12.

(9) Donavan, K.C.; Arter, J.A.; Weiss, G.A., Penner, R.M., *Langmuir* **2012**, *28*, 12581-12587.

(10) Arter, J.A., Diaz, J.E.; Donavan, K.C., Penner, R.M.; Weiss, G.A., *Anal. Chem.* **2012**, *84*, 2776-2783.

(11) Donavan, K.C.; Arter, J.A.; Pilolli, R.; Cioffi, N.; Weiss, G.A., Penner, R.M., *Anal. Chem.* **2011**, *83*, 2420-2424.

(12) Xue, W.; Jiang, X.; Harima, Y., *Synth. Met.* **2010** 160, 803-807.

(13) Harris, P.D.; Arnold, W.M.; Andrews, M.K.; Partridge, A.C. *Sens. Actuat. B-Chem.* **1997**, 42, 177-184.

(14) Bruschi, P.; Cacialli, F.; Nannini, A.; Neri, B., *J. Appl. Phys.* **1994**, 76, 3640-3644.

(15) Yu, L.; Zhang, Y.; Hu, C.; Wu, H.; Yang, Y.; Huang, C.; Jia, N. *Food Chem.* **2015**, 176, 22-26.

(16) Eissa, S.; Siaj, M.; Zourob, M. *Biosen. Bioelectron.* **2015**, 69, 148-154.

(17) Zhang, J.; Wu, D. Z.; Cai, S. X.; Chen, M.; Xia, Y. K.; Wu, F.; Chen, J. H.; *Biosens.Bioelectron.* **2016**, 75, 452-457.

(18) Li, N.; Brahmendra, A.; Veloso, A.J.; Prashar, A.; Cheng, X.R. Hung, V.W.S.; Guyard, C.; Terebiznik, M.; Kerman, K. *Anal. Chem.* **2012**, 84(8), 3485-3488.

(19) Gao, Z.; Deng, H.; Shen, W.; Ren, Y. *Anal. Chem.* **2013**, 85(3), 1624-1630.

(20) Ogata, A.F.; Edgar, J.M.; Majumdar, S.; Briggs, J.S.; Patterson, S.V.; Tan, M.X.; Kudlacek, S.T.; Schneider, C.A.; Weiss, G.A.; Penner, R.M, *Anal. Chem.* **2017**, *89*, 1373-1381.

(21) Xiao, Y.; Jiang, W.; Zhang, F. *ACS Synth. Biol.* **2017**, 6(10), 1807-1815.

(22) Gao, Z.; Deng, H.; Shen, W.; Ren, Y. *Anal. Chem.* **2013**, 85(3), 1624-1630.

(23) Chu, C. H.; Sarangadharan, I.; Regmi, A.; Chen, Y. W.; Hsu, C. P.; Chang, W. H.; Lee, G. Y.; Chyi, J. I.; Chen, C. C.; Shiesh, S. C.; Lee, G. Bin; Wang, Y. L. *Sci. Rep.* **2017**, *7* (1).

(24) Dockal, M.; Carter, D. C.; Ru, F. *October* **1999**, *274* (41), 29303–29310.

(25) Meier, A.R.; Bahureksa, W.A.; Heien, M.L., *J. Phys. Chem. C* **2016**, *120*, 21114−21122.

(26) Majorek, K.A.; Porebski, P.J.; Dayal, A.; Zimmerman, M.D.; Jablonska, K.; Stewart, A.J.; Chruszcz, M.; and Minor, W., *Mol Immunol.* **2012,** *52*, 174–182.

Chapter 4

An Impedance-Transduced Chemiresistor with a Porous Carbon Channel for Rapid, Nonenzymatic, Glucose Sensing

This chapter was adapted from a research article (Ogata, Alana F; Song, Seok-Won; Cho, Su-Ho; Koo, Won-Tae; Jang, Ji-Soo; Jeong, Yong Jin; Kim, Min-Hyeok; Cheong, Jun Young; Penner, Reginald M; Il-Doo Kim. *Analytical Chemistry.* **2018**, 90 (15), 9338-9346)

4.1 Introduction

We describe a new chemical sensor architecture called an impedance transduced chemiresistor (*ITCR*). The *ITCR* combines the simplicity of a nonenzymatic chemiresistor design with unique advantages conferred by an impedance spectroscopy (IS) read-out of the resistor. Like a chemiresistor, an *ITCR* is comprised of a conductive channel material located between two electrodes. But chemiresistors produce a change in the dc resistance of the channel and perturbations of this dc resistance are caused by target binding at the channel. This scheme is very effective for gas sensors (i.e., H_2 gas sensors) but is often not sensitive enough for liquid-based biosensing. For this reason, in typical electrochemical biosensor systems a redox probe (i.e., $(Fe(CN)_6)^{-3/-4}$) is added to the sample solution, and the impedance of this electrode is measured as a function of frequency, providing an opportunity to sample the biosensor signal at frequencies that offer the highest sensitivity.[1–3] Just as in electrochemical sensor designs that rely on a redox species, IS analysis of a chemiresistor enables a systematic analysis and optimization of sensor response across a broad frequency range (i.e., 5 Hz – 40 kHz) providing for the opportunity to optimize signal-to-noise (S/N). The *ITCR* design is also simple, monolithic, readily scalable, and manufacturable.

As a proof-of-concept, we have designed an *ITCR* for the nonenzymatic detection of glucose in aqueous physiological salt solutions. The development of glucose sensors for blood glucose monitoring as required for diabetes mellitus is a mature sub-area defined by many hundreds of scientific contributions (recent reviews are [4–7]). A still unrealized goal, however, is the development of sensors that enable the continuous, noninvasive monitoring of blood glucose. Recent discovery of the correlation between glucose found in lacrimal fluid and blood[8] has inspired the development of contact-lens-embedded sensors for the continuous and noninvasive monitoring

of glucose in tears.[9] However, the correlation of tear glucose with blood glucose is made more difficult by the fact that the concentration range for glucose in lacrimal fluid (0.1 - 0.6 mM)[10] is lower than its concentration range in blood (2 - 30 mM)[11]. A second challenge is that tears produce just 0.5 - 2.2 µL/min of fluid for sampling.[12] Non-enzymatic sensors with sufficient sensitivity for the detection of glucose in tears have been demonstrated (Table B.1), but the majority of these rely on potentiometry, amperometry, or cyclic voltammetry to acquire a response that is based upon the electrochemical glucose oxidation. The complexity imposed by these electrochemical methods compromises the scalability of the sensor and the implementation of the sensor, for example, in contact lenses.[9,12,13] The physiological saline used in this study is intended to mimic "artificial tears" providing an opportunity to evaluate the performance of the *ITCR* sensor for measuring glucose in lacrimal fluid.

The *ITCR* described in this study employs an innovative porous carbon nanofiber (CNF) channel. Electrospun CNFs can be tailored to provide high surface-to-volume ratios and porosity, and controllable electrical conductivity, all of which are important in determining chemiresistor performance.[14] Porous CNFs with large surface areas were obtained by electrospinning copolymer nanofibers where a sacrificial polymer is incorporated and later removed by differential solubility. Specifically, electrospun copolymer nanofibers, containing polyacrylonitrile (PAN) and polyvinylidene fluoride (PVdF), were PVdF serves as the sacrificial polymer, were used to synthesize a fluoride-doped porous nanofiber (F-CNF) channel for the immobilization of 3-aminophenyl boronic acid (ABA) on the nanofiber surface through a boronic acid-flouride complex. We describe the *ITCR* fabrication process, and the properties of this biosensor for measuring glucose in artificial tears.

4.2 Experimental Considerations

4.2.1 Preparation of PVdF-CNFs

Electrospinning solution was prepared by dissolving a mixture of 1 g PAN and 0.5 g PVdF in 16 g of DMF with continuous stirring at 70 ˚C for a minimum of 4 hrs. Electrospinning was carried out using a single-spinneret (21 gauge) under the following conditions; a distance of 20 cm between the needles and the collector, a voltage of 16 kV, and a feeding rate of 20 µL min^{-1}. The as-spun nanofibers were annealed in a tube furnace under reducing gas atmosphere at 600 ˚C for 2 hr at a heating rate of 5 ˚C min^{-1}. The annealed polyvinylidene fluoride - carbon nanofibers were described as F-CNFs. Pristine CNFs were synthesized using an electrospinning solution of 1 g PAN dissolved in 8 g DMF and underwent the same thermal treatment as F-CNFs.

4.2.2 Characterization

Scanning electron microscopy (SEM) were acquired on Pt coated films (XL-30 SFEG, Philips, operating at an accelerating voltage of 10 kV. Transmission electron microscopy (TEM) was performed on nanofibers using a Tecnai G2 F30 S-Twin, FEI. X-ray photoelectron spectroscopy (XPS, Sigma Probe, Thermo VG Scientific) was acquired with Al $K_\alpha$radiation (1486.6 eV). Binding energies were calibrated against the C (1s) peak of carbon found at 284.8 eV as reference. Surface area was measured using the Brunauer-Emmett-Teller theory (BET, ASAP2020, Micromeritics).

4.2.3 Fabrication of ITCR glucose sensors

Electrospun F-CNFs with randomly entangled morphologies were ground by hand in a porcelain mortar into a powder (short nanorods) and dispersed at 10 wt% in ethanol. 50 µL of 3

wt % ABA in methanol was mixed with 100 µL of F-CNF solution and sonicated for 30 mins. 5 wt% Nafion 117 was diluted in PBS to obtain 300 µL of 0.5 wt% Nafion solution which was subsequently added to the ABA/F-CNF solution and vortexed. The final Nafion/ABA/F-CNF solution was used for fabrication of glucose sensors. 3 µL of Nafion/ABA/F-CNF solution was drop-cast onto Al_2O_3 substrates (w: 2.5 mm, l: 2.5 mm, h: 0.2 mm) containing two parallel screen printed Au electrodes (w: 25 µm) with a gap of 70 µm and dried at room temperature for 30 mins. An additional 3 µL of solution was drop-cast and dried at room temperature for 2 hrs. Completed *ITCR* glucose sensors (ABA/F-CNF sensors) were stored in a sealed plastic container for up to a day before used for sensing.

4.2.4 Impedance spectroscopy

All buffer solutions were prepared and brought to room temperature prior to IS measurements. Stock solutions of glucose, fructose, uric acid, and ascorbic acid were stored at 4 ˚C and aliquots were brought to room temperature immediately before IS measurements. A 5 µL droplet of PBS was placed on ABA/F-CNF sensor and sensors were allowed to equilibrate. ElS was first carried out across a frequency range of 5 Hz to 40 kHz over 50 data points. Three consecutive IS measurements were taken in PBS and sensors were then exposed to glucose buffer solutions for 1 min followed by three consecutive IS measurements. Time scan impedance measurements were taken at a frequency of 13 kHz. Immediately after a 5 µL of PBS was dropped onto the ABA/F-CNF sensor, the time scan began. The sensor was allowed to come to equilibration (typically 2 mins). Next, the droplet was carefully taken off the sensor and replaced with a new droplet of glucose buffer solution. All time scan measurements were taken in a homemade chamber to circumvent evaporation and temperature changes in the atmosphere. All IS measurements were

taken using a PalmSens3 controlled by a PS-Trace software. The amplitude of the applied voltage was 10 mV for all IS measurements. Independent electrodes were used for measurements of a single concentration of glucose, fructose, uric acid, and ascorbic acid solutions.

4.3 Results and Discussion

4.3.1 Characterization of PVdF-CNFs

ABA/F-CNF *ITCR*s were fabricated in three simple steps: electrospinning, carbonization, and film drop-casting (Figure 4.1). To synthesize porous carbon nanofibers doped with fluoride (F-CNFs), a copolymer solution of PAN/PVdF was electrospun and carbonized as illustrated in Figure 1a. The PVdF serves two purposes: (1) It provides a source of fluorine required to effect F-doping, and, (2) it serves as a sacrificial polymer that decomposes during carbonization to form pores in the carbon nanofiber. A carbonization temperature of 600 ˚C was chosen for optimal pore synthesis in carbon nanofibers according to BET and XPS analyses shown in Table B.3. After the carbonized F-CNFs were ground to a powder (chopped fibers) and resuspended in ethanol, a solution of 3-aminophenylboronic acid (ABA) was mixed in to form a complex between the boronic acid moiety and fluoride along the nanofiber surface. Next, Nafion was added to the ABA/F-CNF slurry for its common benefits in biosensor films including mechanical stability, biocompatibility, and antifouling properties.[15] The glucose sensors were finished by simple drop-casting of Nafion/ABA/F-CNF solution onto a device small enough to be incorporated into a contact lens (Figure 1b). The device is comprised of an alumina substrate containing two gold electrodes (Figure 4.1c) separated by a 70 μm gap. These glucose sensors require no additional counter or reference electrode and depend only on the conductive channel created by the air-dried Nafion/ABA/F-CNF composite between the gold electrodes (Figure 4.1d). The completed

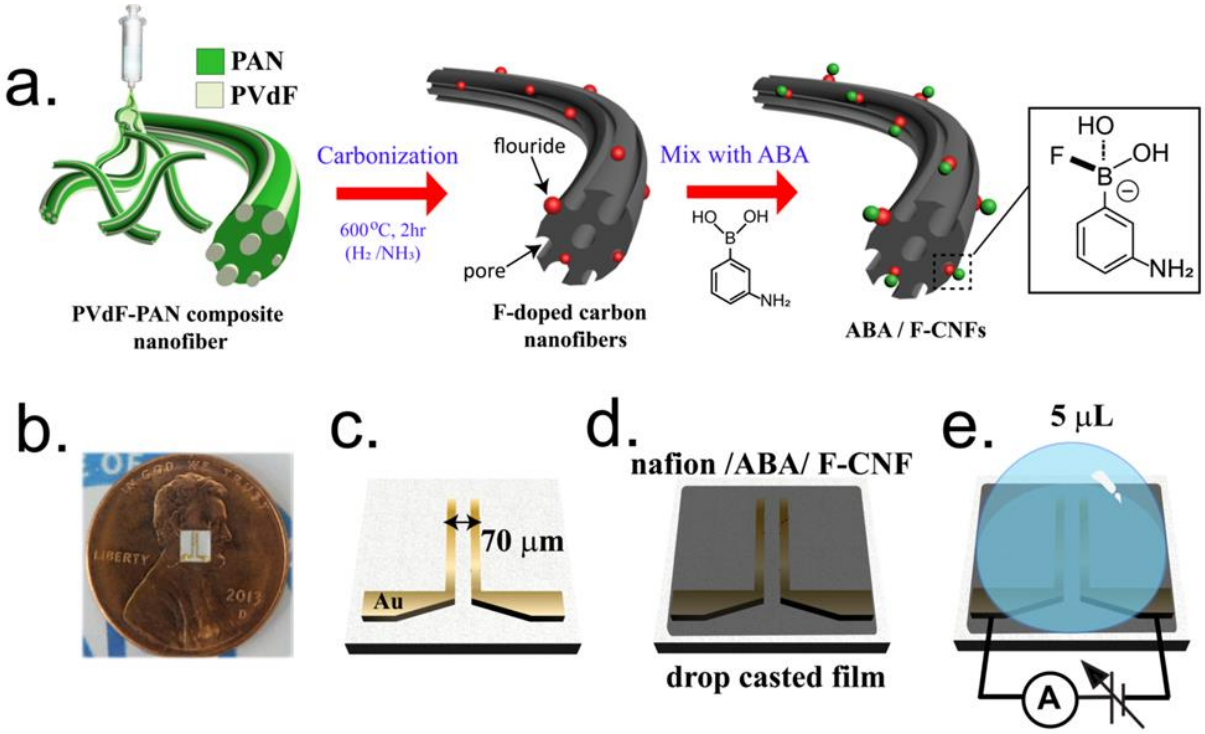

Figure 4.1. Fabrication of an ITCR. Schematic illustration of the synthetic process for preparation of a porous, high surface area channel composed of fluorinated carbon. (a) Electrospun nanofibers composed of PVdF and PAN were carbonized at 600 ˚C under NH_3 for 2 hrs. During carbonization a majority of the PVdF degraded, resulting in the formation of pores distributed along a fluoride-doped carbon nanofiber (F-CNF). ABA is mixed with F-CNFs and immobilized on the nanofiber through complex formed between boronic acid and fluoride. The ABA/F-CNF is then mixed with Nafion. (b) Optical image of a sensor. (c) schematic of sensor comprised of two gold electrodes spaced by a 70 μm gap. (d) A solution of Nafion/ABA/F-CNFs is dropcasted onto the sensor and air dried. (e) The Nafion/ABA-F-CNF film serves as the channel for an *ITCR* device, where the impedance is measured between two gold electrodes. These *ITCR*s require only 5 μL of solution to perform a measurement.

ABA/F-CNF sensors (Figure 4.1e) require a ≈5 μL droplet of sample fluid to run impedance measurements. This sample volume can be reduced further with the addition of a microfluidic flow cell in future designs.

Porous CNFs are simply made by incorporating PVdF into CNF synthesis that additionally provides fluoride doping to immobilize ABA. To probe the effects of PVdF in CNFs, direct comparisons were made against pristine CNFs for characterization studies and electrochemical

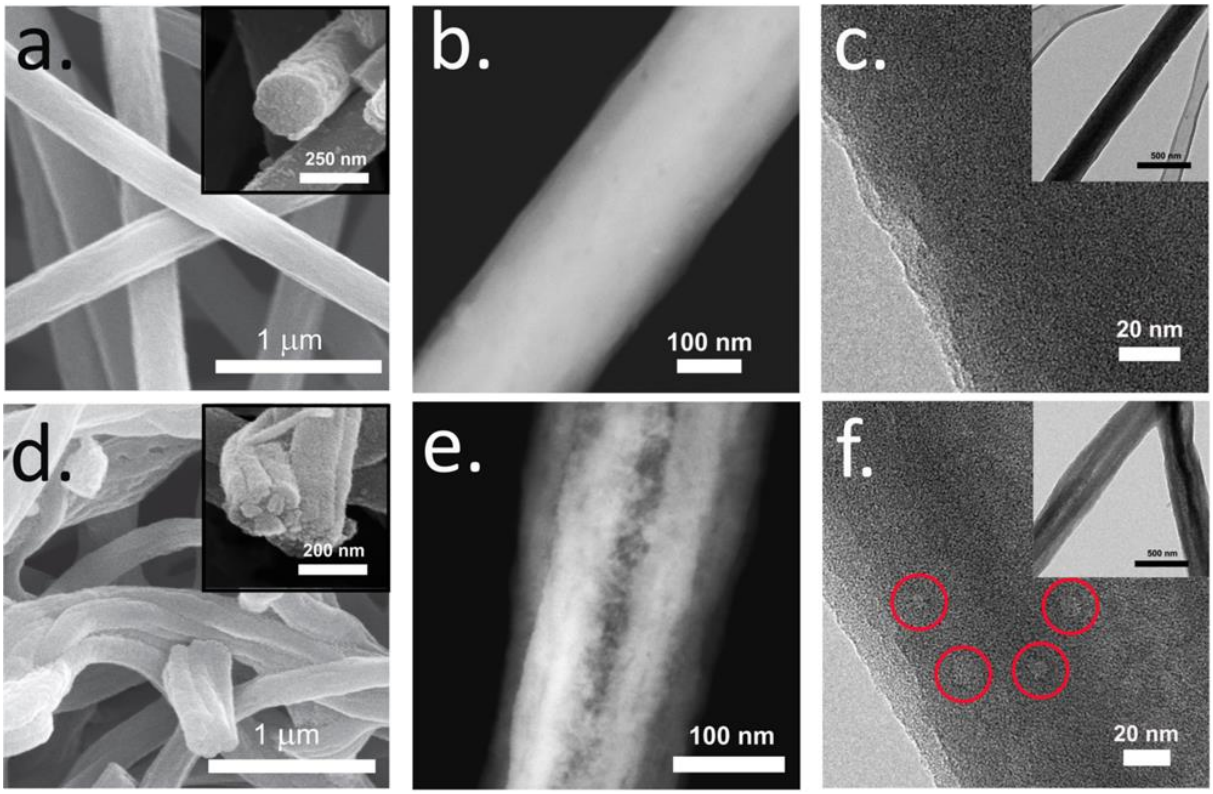

Figure 4.2. Scanning electron microscopy, scanning transmission electron microscopy, and high-resolution transmission electron microscopy images of electrospun carbonized nanofibers. Electrospun CNFs prepared by a spinning solution of PAN without PVdF characterized by (a) SEM, (b) STEM, and (c) HRTEM show a dense and smooth morphology. (d) SEM images of F-CNFs electrospun from a copolymer solution of PAN and PVdF show a porous morphology. (e) STEM of F-CNFs reveal hollow 1D pores throughout the nanofiber. (f) Additional pores along the F-CNF surface are circled in red in HRTEM images.

measurements. Scanning electron micrographs of CNFs synthesized without the addition of PVdF (Figure 4.2a) show dense nanofibers with smooth surfaces and a diameter of ~ 250 nm (inset Figure 4.2a). STEM (Figure 4.2b) and HRTEM (Figure 4.2c) images of CNFs confirm a homogenous, dense morphology that is typical of electrospun CNFs.[16] In contrast, SEM images of F-CNFs show a mesoporous network of single nanofibers and nanofiber bundles that results from PVdF decomposition during the calcination step (Figure 4.2d). A cross sectional image of a single F-CNFs (inset Figure 4.2d) shows a diameter of ~ 200 nm with potentially hollow structures throughout the nanofiber. STEM images (Figure 4.2e) confirm 1D nanostructures along a F-CNF

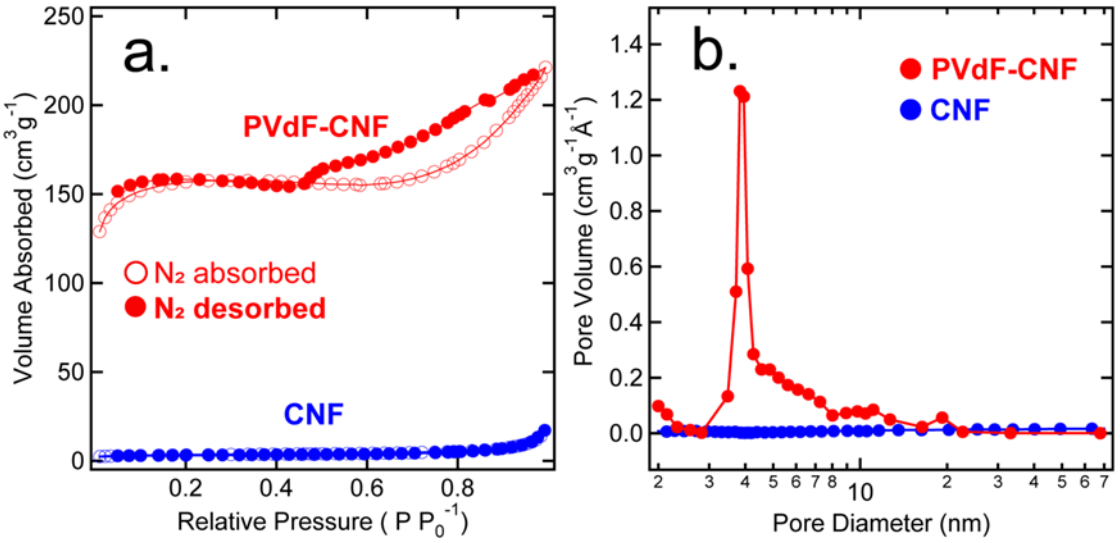

Figure 4.3. BET analysis of CNF and F-CNFs. (a) Nitrogen adsorption/desorption isotherms for CNFs(blue) and F-CNFs (red) give a surface area of 515 m^2/g and 4.51 m^2/g, respectively. (b) Pore distribution for CNFs (blue) and F-CNFs (red). BET pore distribution analysis indicates pores of ~ 4 nm in diameter along the F-CNF surface.

revealing porous nanofiber feature. Additional nanopores (diameter ~ 10 nm) on the F-CNF surface are shown in HRTEM images (Figure 4.2f) circled in red.

BET analysis confirms that PVdF incorporation into CNFs successfully creates a porous morphology with enhanced high surface area. Previously, porous nanofibers in a tangled network produced large surface areas due to the decomposition of a sacrificial polymer.[17] Here, nitrogen adsorption/desorption isotherms clearly reveal a significantly larger surface area for F-CNFs (515 m^2/g) compared to pristine CNFs (4.51 m^2/g) (Figure 4.3a). Significantly large surface areas have been reported for electrospun PVdF nanofibers when carbonized at high temperatures due to the decomposition of fluoride in PVdF which creates nano-sized pores,[18] as seen in this report's STEM images. Such nanopores in F-CNFs are characterized by a small average pore diameter of 4 nm in comparison to CNFs prepared without PVdF that show no pore distribution (Figure 4.3b). The large surface area of F-CNFs is related to the tangled nanostructure network and to the highly

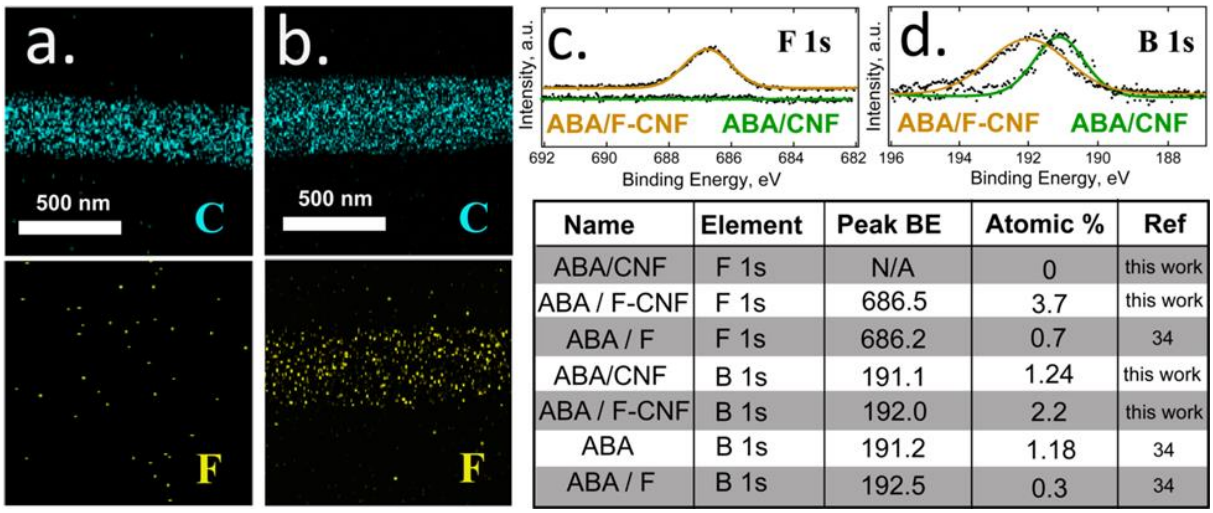

Name	Element	Peak BE	Atomic %	Ref
ABA/CNF	F 1s	N/A	0	this work
ABA / F-CNF	F 1s	686.5	3.7	this work
ABA / F	F 1s	686.2	0.7	34
ABA/CNF	B 1s	191.1	1.24	this work
ABA / F-CNF	B 1s	192.0	2.2	this work
ABA	B 1s	191.2	1.18	34
ABA / F	B 1s	192.5	0.3	34

Figure 4.4. EDS elemental mapping and XPS analysis of CNFs and F-CNFs mixed with ABA as described. EDS elemental mapping of (a) carbon-rich CNFs shows no detectable fluorine. (b) EDS elemental mapping of F-CNFs shows fluorine homogenously distributed on the nanofiber surface. (c) XPS spectra of F in CNFs and F-CNFs. (d) XPS spectra of B in CNFs and F-CNFs mixed in with ABA. Binding energies and elemental atomic percentages for XPS spectra are summarized in Table B.3.

porous nanostructure provided by PVdF. Based upon SEM, TEM, and BET analysis, F-CNFs exhibit a porous morphology that provide a large specific surface area sensing material for ABA/F-CNF *ITCR*s.

Although PVdF serves as an excellent sacrificial polymer for highly porous nanofibers, a majority of the fluoride contained by the polymer, required for immobilizing ABA on the nanofiber sensing surface, is lost after carbonization. Elemental analysis was performed on CNFs and F-CNFs to probe the incorporation of fluoride in F-CNFs. EDX (Figure 4.4a,b) shows that despite a low fluoride content, a homogenous distribution of fluoride is observed along F-CNFs that is absent in pristine CNFs. Both F-CNFs and CNFs are mainly composed of carbon as expected. XPS analysis confirms that fluoride remains in F-CNFs indicated by a F 1s peak at 686.5 eV consistent with PVdF[19] that is absent in CNF XPS spectrum (Figure 4.4c). The ratio (in atomic percent) in F-CNFs for C:F is 84.6:3.7, as calculated from XPS analysis. Such fluoride coverage on F-CNFs

suggests that a similar amount of ABA can be immobilized on F-CNFs. Additional XPS analysis of F-CNFs mixed with ABA produces an atomic percentage ratio of C:F:B = 78.9 : 3.3 : 2.2. In addition, XPS spectra of B 1s (Figure 4.4d) for pristine CNFs mixed with ABA exhibit a peak at 191.13 eV which is attributed to unmodified ABA.[20,21] When ABA is mixed with F-CNFs, the B 1s peak shifts to 192.0 eV which has previously been reported when the boron center on 4-aminophenylboronic acid is bound to fluoride.[21] The positive shift in B 1s XPS spectra indicates the presence of ABA-flouride complex formed in ABA/F-CNFs that is absent in ABA/CNFs. Based on EDS and XPS, we can conclude that a majority of fluoride present in F-CNFs is complexed with ABA, successfully immobilizing ABA on the sensing surface of F-CNFs for efficient signal transduction during glucose sensing.

4.3.2 Impedance spectroscopy of PVdF-CNF ITCR glucose sensors

Impedance spectroscopy (IS) performed on ABA/CNF and ABA/F-CNF ITCRs was compared to assess sensor performance. The equivalent circuit for an *ITCR* (Figure 4.5a) consists of two resistors in parallel, solution resistance (R_{soln}) and channel resistance (R_{ITCR}), coupled together by the double layer capacitance of the carbon channel, $C_{ITCR.}$ Nyquist plots (Z_{im} *vs* Z_{re}) for ABA/CNFs (Figure 4.5b) and ABA/F-CNF (Figure 4.5c) *ITCR* sensors in PBS buffer are displayed with corresponding IS fits according to the equivalent circuit (Figure 4.5a). The *ITCR* equivalent circuit (Table B.2) produces semicircular Nyquist plot across a sufficiently large frequency range, and this semicircle is partially seen in Nyquist plots for ABA/CNFs. As the surface area and porosity of the nanofibers increase, the electrical conductivity of the carbon channel is reduced, causing R_{ITCR} to increase to the point where the semicircular Nyquist behavior is lost.[22] F-CNFs are significantly more resistant than CNFs and therefore Nyquist curves for

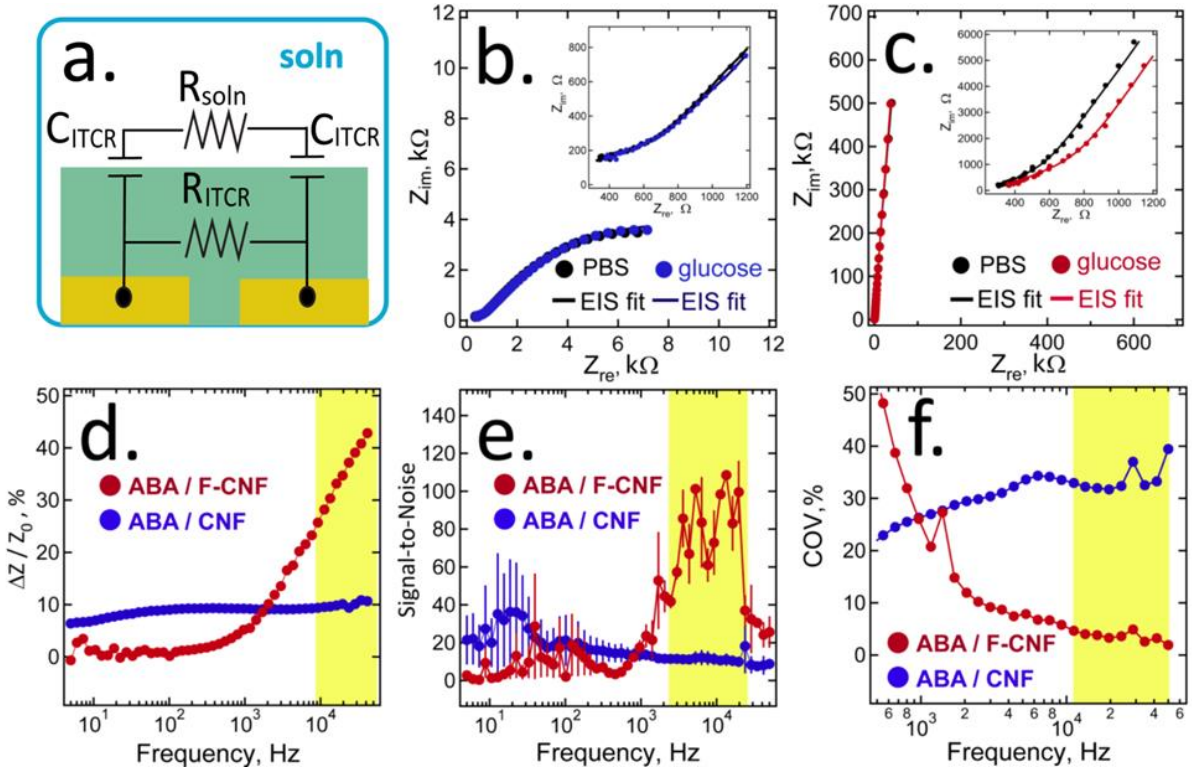

Figure 4.5**.** Impedance spectroscopy (IS) of CNF and F-CNFs *ITCR*s for glucose sensing. (a) Equivalent circuit describing *ITCR*s were R_{soln} represents solution resistance, R_{ITCR} is the resistance of the channel (i.e., CNFs or F-CNFs), and C is the double layer capacitance. This equivalent circuit is used for IS fitting. Nyquist plots for (b) ABA/CNF and (c) ABA-F-CNF *ITCR*s data (circles) with equivalent circuit fits (solid line). Error bars represent the standard deviation, ±1σ, of three consecutive IS measurements on a single *ITCR*. Nyquist curves for a single ABA/CNF ITCR in PBS buffer (black) and 5 mM glucose (blue). IS of ABA/F-CNFs show an increase in impedance from PBS buffer (black) to 5 mM glucose (red). IS analysis of ABA/CNFs (blue) and ABA/F-CNFs (red) where error bars represent the standard deviation, ±1σ, of three independent *ITCR*s. (d) Sensor signal described as the normalized change in impedance, $\Delta Z/Z_0$ (%), versus frequency for *ITCR*s exposed to 5 mM glucose. (e) Signal-to-noise ratios (S/N) by versus frequency for three independent *ITCR*s against 5 mM glucose. S is defined as the average sensor response for three independent *ITCRs* and the related standard deviation, ±1σ, represents, N, noise. (f) Coefficient of variation (COV) versus frequency. Highlighted regions represent frequency range for optimal sensor signal, S/N, and COV.

ABA/F-CNFs resemble an RC series circuit, where at low frequencies the impedance does not complete a semicircle.

Analytical equations for the real and imaginary components of the complex impedance, Z_{re} and Z_{im}, (Table B.2) are used to fit experimental impedance data to extract the values of the three circuit elements: R_{soln}, R_{ITCR}, and C_{ITCR}. A version of the equivalent circuit in which a constant phase element (CPE) is substituted for each capacitor is used for this purpose because better agreement between calculated and experiment impedance data are obtained, resulting in improved precision for the measurement of R_{VBR} (Table B.2). The impedance of a CPE, Z_{CPE}, and the capacitive impedance, Z_C, are defined by these equations:

$$Z_C = \frac{1}{i\,\omega\,C} \qquad Z_{CPE} = \frac{1}{i\,\omega\,Q^n}$$

where ω is the angular frequency (s^{-1}), $i = \sqrt{(-1)}$. Q^n is the CPE capacitance (F) where n has a value of 1.0 if the CPE is purely capacitive. n is used as a fitting parameter in this study and has a value of $1.0 < n < 1.2$. R_{ITCR} obtained from IS fitting confirms that channel resistance for CNFs (14533 Ω) is lower than F-CNFs (40859 Ω) which is attributed to the highly porous morphology of F-CNFs. Upon exposure to 5 mM glucose, the Nyquist curve for ABA/CNFs show relatively little change both at low and high frequencies (inset Figure 4.5b). When ABA/F-CNF sensors are exposed to 5 mM glucose there is a shift to higher impedances in the Nyquist plot that is most notably observed at high frequencies (inset Figure 4.5c). The shift in impedance will be subsequently referred to as the sensor response for *ITCR*s.

The *ITCR* response seen in Figures 4.5b,c was acquired by IS analysis in the frequency range from 5 Hz – 40 kHz, but the use of up to 30 discrete frequencies across this range extends

the measurement time to minutes. A faster analysis time is required for glucose sensors. For this reason, single frequency impedance analysis was attempted for the *ITCR*. To locate the optimum frequency, the *ITCR* signal-to-noise (S/N) (Figure 5e) and the coefficient of variation (CoV) (Figure 4.5f) for three successive measurements, were measured across this frequency range. The *ITCR* response, defined as the ratio of ($\Delta Z/\Delta Z_0$ (%)) for shifts in the total impedance, ΔZ, relative to buffer, is shown for ABA/CNF and ABA/F-CNF sensors for 5 mM glucose sensing (Figure 4.5d). Error bars on these plots represent the standard deviation ($\pm 1\sigma$) of the mean for three consecutive impedance measurements on single sensor for 3 independent glucose sensors. ABA/F-CNFs exhibited the highest glucose response > 25% at frequencies above 10 kHz compared to ABA/CNFs sensors which plateau at a 10% response over the entire frequency range. Based on signal amplitude alone, frequencies above 10 kHz are optimal for sensor response however one must equally assess the noise in a measurement to accurately determine sensor performance. A sensor characterized by high S/N ratios, $\Delta Z/\sigma$, is crucial for obtaining optimal sensitivity and sensor performance. ABA/CNF and ABA/F-CNF sensors show similar S/N ratios except in a frequency range of 2 – 12 kHz, where ABA/F-CNFs are far superior with 5x increase in S/N over ABA/CNFs (Figure 4.5e). Another critical parameter for ABA/F-CNF ITCRs is reproducibility among independent sensors to ensure every one behaves precisely; this is especially important in the realm of disposable or single-use sensors. The best sensor-to-sensor reproducibility, defined by the COV for 3 sensors, is achieved by ABA/F-CNF sensors (<10%) at frequencies above 5 kHz (Figure 4.5f). Highlighted regions in sensor response, S/N, and COV plots represent the optimal frequency range to obtain sensing data. Additionally, ABA/F-CNF ITCRs are more sensitive towards glucose than ABA/CNF ITCRs in the high frequency range. The highest S/N and lowest

COV point determine an optimal frequency of 13 kHz for real-time impedance sensing of ABA/F-CNF glucose sensors.

4.3.3 Real-time detection of glucose in buffer

The real-times sensing properties of ABA/F-CNF sensors were first investigated on a single sensor with successive exposures to 50 µM – 5 mM glucose (Figure 4.6a). Sensor response (ΔZ / ΔZ_0 (%)) versus time measurements were initiated upon rehydration of prepared ABA/F-CNF sensors with 5 µL of PBS buffer for a total of 6 minutes. During this time, ABA/F-CNF sensors equilibrated in 2 minutes and the impedance remained constant for an additional 4 minutes demonstrating a stable sensor with fast equilibration. Exposure to glucose resulted in a rapid increase in impedance that stabilized in 60 s and correlated with increasing concentrations of glucose. The response time is defined as the time required for the increase in impedance from Z_0 to reach 0.9 $\Delta Z_{max,}$ which for ABA/F-CNF sensors is < 8 s. This response time is limited by the time taken to replace solution on the F-CNF/ABA sensor depicted in Figure B.4f, suggesting that sub-5 second response times can be achieved by incorporating a microfluidic cell that allows for continuous solution flow. Nonetheless, a single measurement including exposure to PBS buffer followed by a single glucose concentration can be completed within 3-4 minutes.

To ensure sensor-to-sensor reproducibility, impedance response to single concentrations of glucose were measured on 24 independent sensors (Figure 4.6b). ABA/F-CNF sensors produced similar impedance responses for glucose regardless of the sequence of glucose concentrations and suggests that ABA/F-CNF sensors can precisely measure glucose concentration irrespective of previous exposures to glucose. Additionally, the response time remains at < 8 s despite changes in the magnitude of glucose concentration exposed to the sensor. A total of 24 sensors were tested to

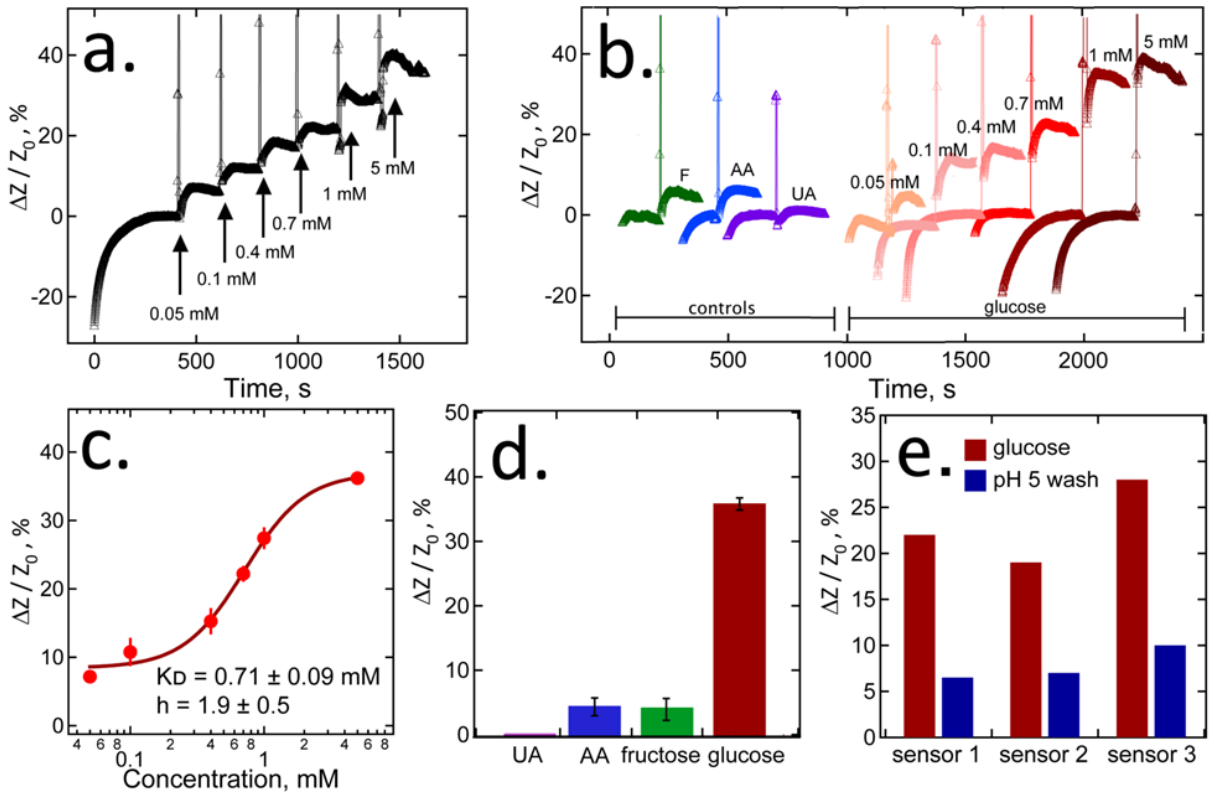

Figure 4.6. Real-time glucose sensing data for ABA/F-CNF *ITCRs*. (a) Sensor signal, $\Delta Z/Z_0$ (%), versus time for a single ABA/F-CNF *ITCR* exposed consecutively to 50 µM – 5 mM glucose. Arrows indicate the time point at which a new glucose solution was replaced on the *ITCR*. (b) Sensor signal versus time for 24 independent ABA/F-CNFs *ITCRs* for single glucose concentrations. Certain *ITCRs* were exposed to 5 mM fructose (F), ascorbic acid (AA), and uric acid (UA) for specificity controls. (c) Calibration plot for 24 ABA/F-CNF *ITCRs* based on real-time sensing data fit to the hill equation (solid line). Errors bars represent the standard deviation, ±1σ, for four *ITCR* sensors exposed to glucose. (d) Specificity assay for ABA-F-CNF *ITCRs* measured for 5 mM uric acid (UA), ascorbic acid (AA), fructose, and glucose. (e) Sensor signal for three ABA-CNF *ITCRs* exposed to 5 mM glucose in pH 7 PBS (red). All sensors were then incubated in pH 5 PBS for 15 min. Subsequently, all sensors were returned to pH 7 PBS and an impedance measurement was taken (blue).

generate a calibration curve (Figure 4.6c) where each data point represents the average response for 4 independent sensors with corresponding standard deviations for the error bars. Sensor response correlates to ligand-receptor behavior according to the Hill equation model:[23]

$$\Delta Z_{ITCR} = \Delta Z_{lim} + \frac{\Delta Z_0 - \Delta Z_{lim}}{1+\left(\frac{C_{glucose}}{K_D}\right)^h} \quad [1]$$

where $C_{glucose}$ is the glucose concentration, ΔZ_0 is the minimum sensor response seen at low $C_{glucose}$, ΔZ_{lim} is the limiting *ITCR* response seen at high $C_{glucose}$, K_D is the dissociation constant representing $C_{glucose}$ at which half of glucose binding sites are occupied. The Hill coefficient, *h*, describes cooperativity of binding where $h = 1$ signifies no cooperativity, $h > 1$ for positive cooperativity, and $h < 1$ occurs for negative cooperativity. The best fit of the Hill equation to the data produced $\Delta Z_0 = 8 \pm 1$ mM, $\Delta Z_{lim} = 37 \pm 2$ mM, $K_D = 0.71 \pm 0.09$ mM, and $h = 1.9 \pm 0.5$ with a $R^2 = 0.98$ square of the regression coefficient. The dissociation constant ($K_D = 0.71 \pm 0.09$ mM) falls within the physiological relevant concentration range of glucose in tear fluids. The measured value of *h*, the cooperativity parameter, indicates positive cooperative in the binding of glucose to ABA on F-CNFs where successive binding events increases the affinity of the sensor for glucose. Previous studies on boronic acid derivatives have also reported cooperative binding to glucose because of its ability for multivalent complexing.[24–26]

To demonstrate selective binding of glucose, ABA/F-CNF sensors were tested against typical interfering species ascorbic acid (AA), uric acid (UA), and fructose (Figure 4.6d). AA and UA are more significant interfering species in tear fluids as compared with fructose, nonetheless fructose presents a stringent control molecule for glucose sensing. The response of ABA/F-CNF sensors to 5 mM glucose is >7x higher compared to 5 mM fructose, AA, and UA. Selectivity

against AA and UA is expected, since UA contains no diols for boronic-acid binding and the negatively charged Nafion matrix can screen out AA. However, ABA has the ability to bind well with fructose and such highly specific binding to glucose provides hints towards the binding mechanism of ABA of F-CNFs. Here, we present a potential theory to explain the specific binding mechanism for glucose to ABA/F-CNFs. Previous boronic acid based sensors have taken advantage of multivalent saccharide binding for enhanced specificity in which glucose has multiple diols that can bind to boronic acids in a 2:1 ratio versus the 1:1 ratio for fructose.[27,28] At the right orientation, glucose can bind to two boronic acid moieties given that the boronic acids can adjust their conformation and are not overcrowded to promote steric hinderance.[29] Glucose sensors in which boronic acid is incorporated into a flexible polymer show impressive selectivity where the formation of 1:2 glucose-boronic acid can crosslink the polymer or create two negative charges. Since the porous F-CNFs provide a flexible scaffold for boronic acid and boronic acid is sparsely incorporated, a similar multivalent-binding process may occur in the system described here. Further experiments are needed to probe the binding mechanisms of ABA/F-CNFs to glucose.

Due to the reversibly of glucose binding by boronic acid derivatives, ABA/F-CNF sensors could be restored by exposure to pH 5 buffer (Figure4. 6e). In basic conditions, the diol-boronic acid complex is disrupted and the boronic acid returns to its original state before a binding event occurs. After 15 minutes of PBS (pH = 5) incubation, sensors were regenerated to 90-95% of their initial impedance.

4.4 Summary

We describe a new type of chemiresistor, the *impedance transduced chemiresistor, ITCR,* for the detection of glucose. The *ITCR* sensor design is defined by two significant innovations: First, its sensing element consists of a porous carbon film that is prepared via the electrospinning of two polymers – and poly(vinyl difluoride) - coupled with pyrolysis. Fluorine from the poly(vinyl difluoride) is incorporated into the resulting porous carbon channel, enhancing the affinity of the channel for a boronic acidic derivative which functions as the glucose receptor. In addition to enabling excellent glucose sensing performance, this channel design is simple, reproducible, inexpensive, and manufacturable. The *ITCR*s second innovation is the use of impedance spectroscopy to transduce glucose binding at this porous carbon channel resistor. IS enables the high precision, high signal-to-noise, measurement of impedance changes by locating and using the optimum frequency for this purpose. IS enhances read-out sensitivity and reproducibility while preserving the simplicity of the chemiresistor architecture.

In this report, we assess the sensing capabilities of an *ITCR* for glucose detection that exploits a chemiresistor channel comprised of ABA immobilized on F-CNFs. Through this analysis we reach two interesting conclusions: First, signal transduction of *ITCR*s is similar to a chemiresistor, where the electrical resistance of the channel material is perturbed by a binding event. Typically, non-faradaic impedance does not produce large signals compared to signal amplification by addition of a redox probe or enzyme. However, here we demonstrate that *ITCR*s can mimic signal enhancement through high-frequency impedance measurements that exploit the *ITCR* equivalent circuit. Second, porous CNFs contribute greatly to the specificity of ABA-based *ITCR*s towards glucose that is not typically observed in other boronic-acid based sensors. Boronic acids can complex with any diol such as fructose and ascorbic acid, but we demonstrate that

ABA/F-CNF *ITCR*s are highly specific to glucose. The *ITCR* is able to detect glucose across the concentration range from 50 µM to 5 mM, spanning the entire range seen for glucose in lacrimal fluid. Diminutive solution volumes of just 5 µL are required for an analysis that occurs in less than 8 s. Highly reproducible sensor-to-sensor performance, characterized by COVs of < 10% across the calibration range indicated above, is enabled by the simple *ITCR* architecture. By choosing a receptor and nanomaterial that are simple to fabricate and provide sensitivity and specificity without compromising the simplicity of the *ITCR* design, we present a proof-of-concept sensor that can transition easily to contact lens sensors for glucose detection.

4.5 Acknowledgements

The authors gratefully acknowledge the financial support of this work by the National Science Foundation, Chemistry Division through contract CHE-1306928. FE-SEM and TEM data were acquired using the instrumentation of the LEXI (lexi.eng.uci.edu/) and IMRI (ps.uci.edu/imri/) facilities at UCI. This work was supported by Wearable Platform Materials Technology Center (WMC) funded by National Research Foundation of Korea (NRF) Grant of the Korean Government (MSIP) (No. 2016R1A5A1009926) and the Ministry of Science, ICT & Future Planning as Biomedical Treatment Technology Development Project (2015M3A9D7067418).

4.6 References

(1) Yu, L.; Zhang, Y.; Hu, C.; Wu, H.; Yang, Y.; Huang, C.; Jia, N. *Food Chem.* **2015**, *176*, 22–26.

(2) Eissa, S.; Siaj, M.; Zourob, M. *Biosens. Bioelectron.* **2015**, *69*, 148–154.

(3) Lin, J.; He, C.; Zhao, Y.; Zhang, S. *Sensors Actuators, B Chem.* **2009**, *137* (2), 768–773.

(4) Rodbard, D. *Diabetes Technol. Ther.* **2016**, *18* (S2), S2-3-S2-13.

(5) Veiseh, O.; Tang, B. C.; Whitehead, K. A.; Anderson, D. G.; Langer, R. *Nature Reviews Drug Discovery*. 2014, pp 45–57.

(6) Wang, H.-C.; Lee, A.-R. *J. Food Drug Anal.* **2015**, *23* (2), 191–200.

(7) Yadav, J.; Rani, A.; Singh, V.; Murari, B. M. *Biomedical Signal Processing and Control*. 2015, pp 214–227.

(8) Zhang, J.; Hodge, W.; Hutnick, C.; Wang, X. *J. Diabetes Sci. Technol.* **2011**, *5* (1), 166–172.

(9) Baca, J. T.; Finegold, D. N.; Asher, S. A. *Ocular Surface*. 2007, pp 280–293.

(10) Yao, H.; Shum, A. J.; Cowan, M.; Lähdesmäki, I.; Parviz, B. A. *Biosens. Bioelectron.* **2011**, *26* (7), 3290–3296.

(11) Heller, A.; Feldman, B. *Chem. Rev* **2008**, *108*, 2482–2505.

(12) Witkowska Nery, E.; Kundys, M.; Jeleń, P. S.; Jönsson-Niedziółka, M. *Anal. Chem.* **2016**, *88* (23), 11271–11282.

(13) Toghill, K. E.; Compton, R. G. *Int. J. Electrochem. Sci.* **2010**, *5* (9), 1246–1301.

(14) Inagaki, M.; Yang, Y.; Kang, F. *Advanced Materials*. 2012, pp 2547–2566.

(15) Lu, J.; Drzal, L. T.; Worden, R. M.; Lee, I. *Chem. Mater.* **2007**, *19* (25), 6240–6246.

(16) Zhang, L.; Aboagye, A.; Kelkar, A.; Lai, C.; Fong, H. *Journal of Materials Science*. 2014, pp 463–480.

(17) Ryu, W.-H.; Jung, J.-W.; Park, K.; Kim, S.-J.; Kim, I.-D. *Nanoscale* **2014**, *6* (19), 10975–10981.

(18) Hong, S.-M.; Kim, S. H.; Jeong, B. G.; Jo, S. M.; Lee, K. B. *RSC Adv.* **2014**, *4* (103),

58956–58963.

(19) Militello, M. C.; Gaarenstroom, S. W. *Surf. Sci. Spectra* **1999**, *6* (2), 141–145.

(20) Wang, J. Y.; Chou, T. C.; Chen, L. C.; Ho, K. C. *Biosens. Bioelectron.* **2015**, *63*, 317–324.

(21) Liu, Q.; Xiao, K.; Wen, L.; Dong, Y.; Xie, G.; Zhang, Z.; Bo, Z.; Jiang, L. *ACS Nano* **2014**, *8* (12), 12292–12299.

(22) Yang, D. S.; Chaudhari, S.; Rajesh, K. P.; Yu, J. S. *ChemCatChem* **2014**, *6* (5), 1236–1244.

(23) Kurganov, B. I.; Lobanov, A. V.; Borisov, I. A.; Reshetilov, A. N. *Anal. Chim. Acta* **2001**, *427* (1), 11–19.

(24) Heinrichs, G.; Schellenträger, M.; Kubik, S. *European J. Org. Chem.* **2006**, No. 18, 4177–4186.

(25) KUMAI, M.; KOZUKA, S.; SAMIZO, M.; HASHIMOTO, T.; SUZUKI, I.; HAYASHITA, T. *Anal. Sci.* **2012**, *28* (2), 121–121.

(26) D'Silva, C.; Green, D. *J. Chem. Soc. Chem. Commun.* **1991**, No. 4, 227–229.

(27) Kong, K. V.; Ho, C. J. H.; Gong, T.; Lau, W. K. O.; Olivo, M. *Biosens. Bioelectron.* **2014**, *56*, 186–191.

(28) Bull, S. D.; Davidson, M. G.; Van Den Elsen, J. M. H.; Fossey, J. S.; Jenkins, A. T. A.; Jiang, Y. B.; Kubo, Y.; Marken, F.; Sakurai, K.; Zhao, J.; James, T. D. *Acc. Chem. Res.* **2013**, *46* (2), 312–326.

(29) Wu, X.; Li, Z.; Chen, X.-X.; Fossey, J. S.; James, T. D.; Jiang, Y.-B. *Chem. Soc. Rev.* **2013**, *42* (20), 8032.

(30) Cho, S. J.; Noh, H.-B.; Won, M.-S.; Cho, C.-H.; Kim, K. B.; Shim, Y.-B. *Biosens. Bioelectron.* **2018**, *99* (May 2017), 471–478.

(31) Gu, S.; Ma, K.; Kong, J.; Al-Ghanim, K. A.; Mahboob, S.; Liu, Y.; Zhang, X. *Int. J. Electrochem. Sci.* **2017**, *12* (6), 5092–5103.

(32) Thiruppathi, M.; Thiyagarajan, N.; Gopinathan, M.; Chang, J. L.; Zen, J. M. *Microchim. Acta* **2017**, *184* (10), 4073–4080.

(33) Kim, D.-M.; Moon, J.-M.; Lee, W.-C.; Yoon, J.-H.; Choi, C. S.; Shim, Y.-B. *Biosens. Bioelectron.* **2016**, *91* (June 2016), 276–283.

(34) Çiftçi, H.; Alver, E.; Çelik, F.; Metin, A.; Tamer, U. *Microchim. Acta* **2016**, *183* (4), 1479–1486.

(35) Shishkanova, T. V.; Fitl, P.; Král, V.; Barek, J. *J. Electroanal. Chem.* **2016**, *761*, 106–111.

(36) Badhulika, S.; Tlili, C.; Mulchandani, A. *Analyst* **2014**, *139* (12), 3077–3082.

(37) Lerner, M. B.; Kybert, N.; Mendoza, R.; Villechenon, R.; Bonilla Lopez, M. A.; Charlie Johnson, A. T. *Appl. Phys. Lett.* **2013**, *102* (18).

(38) Das, D.; Kim, D. M.; Park, D. S.; Shim, Y. B. *Electroanalysis* **2011**, *23* (9), 2036–2041.

(39) Tlili, C.; Badhulika, S.; Tran, T. T.; Lee, I.; Mulchandani, A. *Talanta* **2014**, *128*, 473–479.

Appendix B

Supplementary Information for Chapter 4

B.1 Glucose Sensing Literature

Table B.1: Summary of related glucose sensing literature involving boronic-acid derivatives

Bioaffinity element	Detection method	linear range	limit of detection	response time	Specific against fructose?	sample volume	Intra-assay COV	ref
hierarchical CuCo bimetal coated with glucose-imprinted polymer composed of nafion, polurethane and aminophenyl boronic acid	Chrono amperometry	1.0 - 25 mM	0.65 ± 0.1 µM	5 s	No	4.5 mL	N = 5 ± 5%	[30]
polyethyleneimine gold nanoparticles porphyrin nanocomposites functionalized with mercaptophenyl boronic acid	DPV	10 - 350 µM	2.16 µM	30 s	No	N/A	N = 5 for 3.1% (0.05 mM glucose)	[31]
screen printed carbon electrode with an azo-functionalized dimer of 4-amino phenyl boronic acid	DPV ($Fe(CN)_6$)	1 - 500 µM	0.36 µM	N/A	No	N/A	N = 5 1.92%	[32]
A molecularly imprinted polymer containing acrylamide, and aminophenyl boronic acid	potentiometry	32 µM - 1 mM	19 µM	2 min	No	N/A	N = 5 3.25% (0.1 mM glucose)	[33]
3-aminophenyl boronic acid immobilized on polyethyleneimine coated gold nanoparticles	potentiometry	0.5 - 50 mM	0.025 mM	N/A	No	N/A	N/A	[34]
mercaptopphenylboronic acid modified gold nanoparticles	potentiometry	0.31 – 33 mM	.2 mM	N/A	No	N/A	N = 3 5.8 - 6.9 %	[35]
poly(aniline boronic acid) functionalized single walled carbon nanotubes	Chemiresistor I-V response	~ 4 – 10 mM	3.46 mM	4 min	No	20 µL	N/A	[36]
carbon nanotube transistor functionalized with pyrene-1-bornic acid	source-drain current	1 µM - 100 mM	300 nM	1.3 s	No	1.5 µL	N/A	[37]
3-aminophenyl boronic acid bonded on terthiophene-3-carboxylic acid	DPV	0.9 - 9.1 µM	0.49 µM	N/A	No	N/A	3.8% (1.0 µM glucose)	[38]
3-aminophenyl boronic acid immobilized on single walled carbon nanotubes	Chemiresistor I-V response	1 – 25 mM	1.2 mM	10 min	No	N/A	Inter-assay N = 7 3.5%	[39]
3-aminophenylboronic acid functionalized on porous carbon nanofibers	***ITCR***	**0.1 mM – 1 mM**	**0.1 mM**	**< 8 s**	**Yes**	**< 5 µL**	**N = 4 2.6 – 10 %**	**This work**

B.2 Equivalent Circuits

Table B.2. Equivalent circuits and equations representing the electrical response of a *ITCR* glucose sensor.

Eq. Circuit[a]	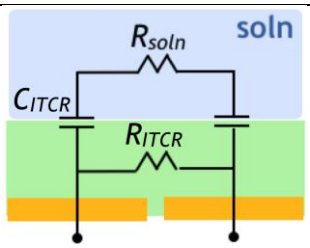
Z_{re} =	$\dfrac{R_{ITCR}R_{soln}\,(R_{ITCR}+R_{soln}\,)+\dfrac{R_{ITCR}}{\omega^2 {C_{ITCR}}^2}}{(R_{ITCR}+R_{soln}\,)^2+\dfrac{1}{\omega C_{ITCR}}^2}$
Z_{im}=	$\dfrac{\dfrac{{R_{ITCR}}^2}{\omega C_{ITCR}}}{(R_{ITCR}+R_{soln}\,)^2+\dfrac{1}{\omega C_{ITCR}}^2}$
Eq. Circuit[b]	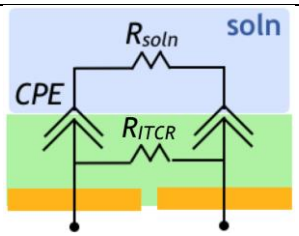
Z_{re}=	$\dfrac{R_{ITCR}[\,1+Q_{ITCR}\omega^n(2R_{ITCR}+R_{soln})\cos\frac{\pi n}{2}+\,R_{soln}{Q_{ITCR}}^2\omega^{2n}(R_{soln}+R_{ITCR})]}{Q_{ITCR}\omega^n(R_{soln}+R_{ITCR})\left[(R_{soln}+R_{ITCR})Q_{ITCR}\omega^n+2\cos\frac{\pi n}{2}\right]+1}$
Z_{im}=	$\dfrac{-\,R_{ITCR}^2\,\omega^n\,Q_{ITCR}\,\sin\frac{\pi n}{2}}{Q_{VBR}\omega^n(R_{soln}+R_{ITCR})\left[(R_{soln}+R_{ITCR})Q_{ITCR}\omega^n+2\cos\frac{\pi n}{2}\right]+1}$

[a]Capacitive equivalent circuit, [b]Equivalent circuit with constant phase elements (CPEs).

B.3 Optimization of Calcination Temperature

Table B.3. Optimization of PVDF-PAN calcination temperature.

Nanofiber	**Calcination Temperature (˚C)**	**XPS F atomic %**	**BET Surface Area (m^2/g)**
PAN only	600	0	4.51
PVdF/PAN	400	34	N/A
PVdF/PAN	500	26	176
PVdF/PAN	600	3.7	515
PVdF/PAN	1000	0	600

Discussion of Table B.3. PVdF/PAN nanofibers were calcinated at temperatures 400, 500, 600, 1000 ˚C. Corresponding XPS analysis shows that fluoride composition decreases as calcination temperature increases where at 1000 ˚C all fluoride is completely decomposed. Corresponding BET analysis shows a significant increase in surface area as calcination temperature increases. Nanofibers composed of PAN only show no fluoride content and very small surface area. An optimal calcination temperature of 600 ˚C was selected to have maximum surface area while retaining fluoride in the nanofibers.

B.4 Real Time Glucose Sensing

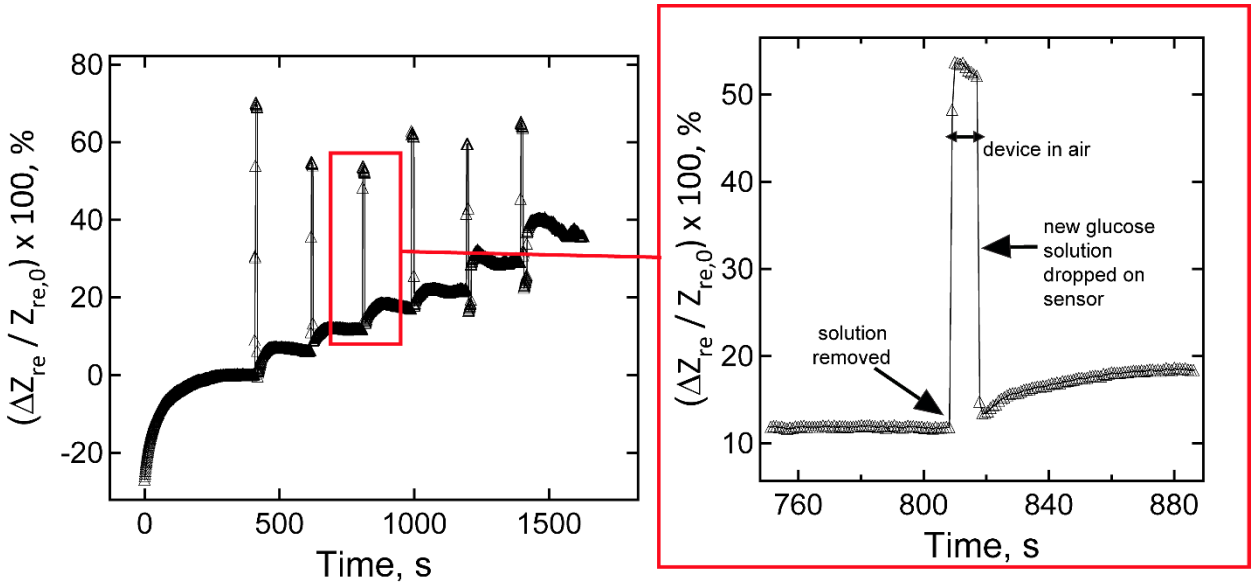

Figure B.4. Real-time glucose sensing data for ABA/F-CNF ITCRs. Sensor signal, $\Delta Z/Z_0$ (%), versus time for a single ABA/F-CNF *ITCR* exposed consecutively to 50 µM – 5 mM glucose. Arrows indicate the time point at which a new glucose solution was replaced on the *ITCR*. The red box magnifies a time period where a new glucose concentration is exposed to the sensor. First, the previous buffer solution is removed and the sensor is in air for a short time until a new buffer solution is dropped on the sensor. The response time is defined as the time from when the previous solution is removed to when the new solution is applied to the sensor and sensor signal reaches 0.9 $\Delta Z_{max.}$